

**Fabrication of Polysulfone-based (ZnO-
GO-NiO) Mixed Matrix Membrane for the
Adsorptive Removal of Lead (Pb⁺²) and
Cadmium (Cd⁺²) Heavy Metal Ions from
wastewater**



By
Arslan Maqbool

School of Chemical & Materials Engineering
National University of Sciences and Technology
2023

Fabrication of Polysulfone-based (ZnO-GO-NiO) Mixed Matrix Membrane for the Adsorptive Removal of Lead (Pb⁺²) and Cadmium (Cd⁺²) Heavy Metal Ions from wastewater



Arslan Maqbool

Registration No: 00000329400

**This thesis is submitted as a partial fulfilment of the requirements for the degree of
MS Chemical Engineering**

Supervisor: Dr. Ameen Shahid

**School of Chemical & Materials Engineering (SCME)
National University of Sciences and Technology (NUST)
H-12, Islamabad, Pakistan
August, 2023**

THESIS ACCEPTANCE CERTIFICATE



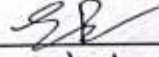
THESIS ACCEPTANCE CERTIFICATE

Certified that final copy of MS thesis written by **Mr Arslan Maqbool** (Registration No 00000329400), of School of Chemical & Materials Engineering (SCME) has been vetted by undersigned, found complete in all respects as per NUST Statues/Regulations, is free of plagiarism, errors, and mistakes and is accepted as partial fulfillment for award of MS degree. It is further certified that necessary amendments as pointed out by GEC members of the scholar have also been incorporated in the said thesis.

Signature: 

Name of Supervisor: Dr Ameen Shahid

Date: 15-08-2023

Signature (HOD): 

Date: 15/8/23

Signature (Dean/Principal): 

Date: 15.8.2023

TH-1

MS CHE-08-2020

Form TH-1

(Must be type written)



**National University of Sciences & Technology
(NUST)**

MASTER'S THESIS WORK

Formulation of Guidance and Examination Committee (GEC)

Name: Arslan Maqbool

NUST Regn No: 00000329400

Department: SCME

Specialization: _____

Credit Hour Completed: (18) 24

CGPA: (3.33) 3.38

Course Work Completed

S/No	Code	Title	Core/Elective	CH	Grade
1	CHE-843	Separation Process in Chemical Engineering	Core	03	B
2	EME-921	MHMT in Chemical Engineering	Core	03	B+
3	ENE-809	Waste Water Treatment & Design	Elective	03	B+
4	RM-898	Research Methodology	Elective	00	Q
5	CHE-847	Chemical Kinetics & Reactor Design	Core	03	B
6	CHE-816	Molecular Nanotechnology	Elective	03	B+
7	EME-981	Advanced Fuel Technology	Elective	03	B+
8	CHE-098	Gasification Processes	Elective	03	B+
9	EE-911	Carbon capture & Utilization	Elective	03	B+

Date: 15 September, 2021

Student's Signature: _____

Thesis Committee

- Name: Dr. Ameen Shahid (supervisor)
Department: SCME
- Name: Dr. Zaib Jahan (Co-supervisor)
Department: SCME
- Name: Dr. Zakir Hussain
Department: SCME
- Name: Dr. Bilal Kahan Niazi
Department: SCME
- Name: Dr. Muhammad Ali Inam (External)
Department: IESE

Signature: _____

Signature: _____

Signature: _____

Signature: _____

Signature: _____

Date: 28/9/21

Signature of Head of Department: _____

APPROVAL

Date: 28.9.2021

Dean/Principal

TH-4



National University of Sciences & Technology (NUST)

FORM TH-4

MASTER'S THESIS WORK

We hereby recommend that the dissertation prepared under our supervision by

Regn No & Name: 00000329400 Arslan Magbool

Title: Fabrication of Polysulfone-based (ZnO-GO-NiO) Mixed Matrix Membrane for the Adsorptive Removal of Lead (Pb⁺²) and Cadmium (Cd⁺²) Heavy Metal Ions from Wastewater.

Presented on: 18 May 2023 at: 1400 hrs in SCME Seminar Hall

Be accepted in partial fulfillment of the requirements for the award of Master of Science degree in Chemical Engineering.

Guidance & Examination Committee Members

Name: Dr Zakir Hussain

Signature: [Signature]

Name: Dr Muhammad Bilal Khan Niazi

Signature: [Signature]

Name: Dr Muhammad Ali Inam (IESE)

Signature: [Signature]

Name: Dr Zaib Jahan (Co-Supervisor)

Signature: [Signature]

Supervisor's Name: Dr Ameen Shahid

Signature: [Signature]

Dated: 22-05-2023

Head of Department

Date 9/8/23

Dean/Principal

Date 10.8.2023

School of Chemical & Materials Engineering (SCME)

بِسْمِ اللَّهِ الرَّحْمَنِ الرَّحِيمِ

۱۴۳۸

Dedicated To

**MY TEACHERS, PARENTS, SIBLINGS AND FRIENDS
WHO ENABLED ME TO COMPLETE MY MASTER'S
DEGREE**

Acknowledgement

“He is Allah; there is no deity except Him. To Him is praise in the first [life] and the Hereafter. And His is the [final] decision, and to Him you will be returned” (Al Qasas: 70).

I’m grateful to **Almighty Allah** for giving me all the grace to pursue this study. Undoubtedly these are His unlimited blessings that made me complete this work. And peace and blessings be upon **Prophet Muhammad (PBUH)** who enlightened our minds to acknowledge our creator.

I show gratitude to my dear parents, for their encouragement in all respects of my study. I would also like to include a extraordinary note of thanks to my siblings who incited and stood by me.

My honest thanks and gratitude to my supervisor, **Dr. Ameen Shahid** and co-supervisor, **Dr. Zaib Jahan**, and all the GEC member, for their critical comments on early drafts, kind behaviour, constructive suggestions and all the way helpful supervision. Without their tireless guidance and patience, this research would not have been completed.

Lastly, I feel pleasure and deep sense of indebtedness to all friends for being always prompt and supportive.

Abstract

The presence of heavy metal ions, such as chromium, lead and cadmium, in industrial wastewater discharge streams are major contaminants that poses a risk to human health. These HMs should be separated from the wastewater to ensure the reuse of the discharged water again in the process and also to mitigate their environmental impacts. The distinctive mechanical properties of 2D graphene oxide (GO), antifouling characteristics of zinc oxide (ZnO), and metal oxide (NiO) nanoparticles can be combined to produce composites supporting special features for various applications in wastewater treatment. In this study, solution casting and phase inversion methods were employed to synthesize polysulfone-based GO, ZnO-GO and ZnO-GO-NiO mixed matrix membranes with different compositions and the effects of variation in composition on the removal of lead (Pb²⁺) and cadmium (Cd²⁺) ions were examined. Several characterization techniques including X-ray diffraction analysis (XRD), Fourier transform infrared spectroscopy (FTIR), scanning electron microscopy (SEM), and energy dispersive X-ray (EDX) were applied to investigate the crystallinity, functional groups, morphology, and elemental analysis of the synthesized nanoparticles and composite membranes, respectively. The composite membranes were also analyzed in terms of their porosity, pore size, permeability, contact angle, surface zeta potential, surface roughness, thermal stability, mechanical strength, and flux regeneration at the different transmembrane pressure of 2-3 kgcm⁻². The effect of variation in feed concentrations on the total adsorption capacity was investigated by varying the feed concentrations from 50 to 200 mg L⁻¹ and fixed pH value of 5.5. Highest adsorption capacity was measured to be 308.16 mg g⁻¹ and 354.80 mg g⁻¹ for Pb (II) and Cd (II) respectively, for membrane (M4_A) having 0.3 wt.% of ZnO-GO-NiO nanocomposite, at 200 mg L⁻¹ of feed concentration and 1.60 mL min⁻¹ of permeate flux. Yet, the lower feed concentration and flow rate allowed the membrane to operate for a longer period of time while maintaining a better efficiency without regeneration. The Pb (II) and Cd (II) adsorption breakthrough curves were created, and the experimental data was compared with the Thomas model that shows $\pm 4.7\%$ error and 0.99 correlation coefficient (R^2).

Table of Contents

DECLARATION.....	
APPROVAL FOR SUBMISSION.....	
DEDICATION.....	i
ACKNOWLEDGEMENTS.....	ii
ABSTRACT.....	iii
TABLE OF CONTENTS	iv
LIST OF TABLES.....	viii
LIST OF FIGURES	ix
LIST OF APPENDICES	xi

CHAPTER 1- Introduction

1.1 Background.....	2
1.2 Membrane separation.....	5
1.3 Problem Statement.....	6
1.4 Aims and Objectives.....	7
1.5 Scope.....	8
1.6 Characterization techniques.....	8

CHAPTER 2- Literature review

2.1 Heavy Metals.....	9
2.2 Adsorption Mechanism.....	10
2.2.1 Ion Exchange.....	12
2.2.2 Electrostatic Attractions.....	12
2.2.3 Surface Complexation.....	13
2.3 PSF-based Membrane.....	14
2.4 Adsorbents for Heavy Metal Removal.....	15
2.4.1 Metal & Metal Oxides.....	15
2.4.1.1 Zirconium.....	15
2.4.1.2 Zinc oxide.....	16
2.4.1.3 Iron and Iron oxide.....	16
2.4.2 Carbon Source.....	18
2.4.2.1 Graphene oxide.....	19

2.4.2.2 Carbon nanotube.....	20
2.4.2.3 Activated carbon.....	21
2.4.3 Natural Source.....	21
2.4.3.1 Chicken eggshells.....	21

CHAPTER 3- Materials & Methods

3.1 General Preview.....	22
3.2 Materials.....	22
3.3 Dead end filtration unit.....	23
3.4 Synthesis of nano particles.....	24
3.4.1 Synthesis of graphene oxide by modified hummers' method.....	24
3.4.2 Synthesis of nano zinc oxide.....	25
3.5 Synthesis of ZnO-decorated GO nanocomposite.....	25
3.6 Synthesis of ZnO-GO-NiO nanocomposite.....	26
3.7 Casting Solution Preparation.....	27
3.7.1 Membrane Casting method.....	27
3.7.2 Phase inversion method.....	28
3.8 Nanoparticles and Membrane Characterization.....	29
3.8.1 Scanning electron microscopy (SEM).....	30
3.8.2 Energy dispersive X-ray spectroscopy (EDX).....	30
3.8.3 X-ray diffraction (XRD).....	30
3.8.4 Fourier transform infrared spectroscopy (FTIR).....	31
3.8.5 Atomic force microscopy (AFM).....	31
3.8.6 Atomic absorption spectroscopy (AAS).....	31
3.8.7 Universal testing machine (UTM).....	32
3.8.8 Contact angle measurement.....	32
3.9 Permeability test of membranes.....	32
3.10 Pure water flux of membranes and hydraulic permeability.....	34
3.11 Equilibrium water content, porosity, compaction factor, mean pore diameter, and hydrophilicity.....	34
3.12 Membrane compaction factor.....	35
3.13 Mechanical characteristics of membranes.....	36
3.14 Antifouling properties and permeate flux recovery.....	36

3.15 Measurement of surface zeta potential.....	36
3.16 Lead and cadmium ions removal experiment.....	37
3.17 Adsorption kinetics for cadmium and lead ions removal.....	38
3.18 Stock Solution Preparation.....	38
3.18.1 Preparation of Cd ²⁺ Solution.....	39
3.18.2 Different concentration Cd ²⁺ Solutions preparation.....	39
3.18.3 Preparation of pb ²⁺ Solution.....	39
3.18.4 Different concentration pb ²⁺ Solutions preparation.....	39
3.19 Heavy Metals Adsorption Performance Test.....	40
3.20 Evaluation of the conditions of adsorption.....	40
3.20.1 Effect of pH on the Adsorption efficiency.....	40
3.20.2 Effect of Contact Time.....	40
3.21 Desorption and Regeneration.....	41
3.22 Bulk Analysis.....	41

CHAPTER 4- Results and Discussion

4 Results and discussions.....	43
4.1 Membrane Characterization and NPs.....	43
4.1.1 Microscopic analysis (NPs and Composite morphology).....	44
4.1.1.1 Membranes morphology.....	45
4.1.2 Contact Angle.....	45
4.1.3 Surface zeta potential.....	50
4.1.4 Atomic force microscopy (AFM).....	51
4.1.5 X-ray diffraction (XRD).....	52
4.1.6 Spectroscopic analysis (FTIR).....	55
4.1.7 Macroscopic analysis.....	57
4.1.8 Mechanical characteristics.....	58
4.2 Pure water fluxes (PWF) of membranes.....	59
4.3 Total fouling and the flux recovery ratio of membranes.....	61
4.4 Heavy metal ions removal.....	62
5. CONCLUSION.....	68

REFERENCES.....70
APPENDICES.....76

List of Tables

Table 1.1: Merits and demerits of heavy metal removal methods from aqueous phase.....	3
Table 1.2 Characterization techniques and their purpose.....	8
Table 2.1: Sources & Effects of Heavy Metal ions.....	9
Table 2.2: PSF-based nanocomposite MMMs (PSF/PEG-4000 blended membranes) used for the cadmium (Cd^{2+}) and lead ions (Pb^{2+}) removal.....	18
Table 3.1 Quantity and physical form of the chemicals used in experimentation.....	22
Table 3.2 Amount of chemicals used in synthesis of graphene oxide.....	25
Table 3.3 Composition of membrane casting solutions.....	29
Table 4.1 Mechanical characteristics of synthesized composite membranes.....	59
Table 4.2: Pure water flux at transmembrane pressure, contact angle, equilibrium water content, porosity, permeability, compaction factor at transmembrane pressure and mean pore diameter of synthesized membranes (Zhang, Xiao and Hu, 2013a).....	61
Table 4.3 Pb(II) and Cd(II) adsorption at various feed concentrations: Approximated values from Thomas model.....	64

List of Figures

Figure 1.1: EURO statistic explained about the share of industrial categories in the total water use in industry (%) in different countries.....	1
Figure 2.1 Molecular structure of GO.....	11
Figure 2.2: Electrostatic Attraction & Ion Exchange between GO and heavy metal ions	12
Figure 2.3: Adsorption of Heavy Metals on GO via Surface Complexation.....	13
Figure 2.4: Chemical Structure of polysulfone (PSF).....	14
Figure 2.5: Porosity & Contact Angle Comparison of (PVDF) and (PVDF/ZnO) Hybrid MMMs.....	15
Figure 2.6: Reusability of Nano fibrous Membranes in Adsorption.....	16
Figure 2.7: The Rejection Rate of Heavy Metals (Cu^{2+} , Pb^{2+} , Cr^{3+} and Cd^{2+}) and Dyes for Pure GO Membrane and GO-IPDI Membrane. (Khandegar, Kaur and Chanana, 2021).....	18
Figure 3.1 Dead end filtration unit.....	24
Figure 3.2 Illustration of the nanoparticles/composites synthesis and functionalization procedures...	27
Figure 3.3 Membrane composition and preparation method (a) solution casting (b) phase inversion...	28
Figure 3.4 (a) Schematic representation of the bench scale filtration system used in the study (Dead End Filtration Unit) and (b) a comparison mechanism of dead end and cross-flow filtration.....	34
Figure 4.1: SEM Images of nanoparticles.....	44
Figure 4.2: SEM Images of synthesized membranes surface and cross-section as mentioned on each membrane.....	46
Figure 4.3 Contact angle of synthesized composite membranes from (M1) to (M4_A).....	49
Figure 4.4 Surface charges of the membranes, (b) Atomic force microscopy (AFM) images of membranes.....	51
Figure 4.5. XRD spectra (a) of nanoparticles GO, ZnO, and nanocomposites ZnO-GO, and ZnO-GO-NiO and (b) composite membranes.....	54
Figure 4.6: FTIR spectra of nanoparticles and nanocomposites.....	56
Figure 4.7 TGA curves of neat PSF, GO, ZnO-GO, and ZnO-GO-NiO PSF-based mixed matrix membranes (b) Stress w.r.t the strain variations for mixed matrix membranes.....	58

Figure 4.8) Pure water flux (PWF) of different composition membranes at three different pressures (2, 2.5, and 3 kg cm ⁻²) (b) Graphical representation of R _t , R _r , R _{ir} and FRR values (%) of synthesized membranes.....	60
Figure 4.9 Percentage removal with different concentrations of Pb ²⁺ and Cd ²⁺ ions.....	64
Figure 4.10 Change in adsorption capacity values (mg g ⁻¹) of membrane (M4_A) for Pb (II) and Cd (II) ions.....	65
Figure 4.11 Breakthrough curves at various feed concentrations.....	66
Figure 4.12 EDX analysis of membranes (a) before adsorption (b) after adsorption, and (c) compositional analysis of membrane (M4_A).....	67

List of Appendices

APPENDIX A: Cd ²⁺ Stock Solution Preparation Calculation.....	76
APPENDIX B: 40 ppm of Cd ²⁺ Solution preparation calculation.....	76
APPENDIX C: Pb ²⁺ Stock Solution Preparation Calculation.....	76
APPENDIX D: 0.2 M of HCl solution preparation Calculation.....	77
APPENDIX E: 0.2 M NaOH Solution Preparation Calculation	77

Chapter 1

Introduction

1.1 Background

The question for freshwater supplies is increasing day by day in the whole world due to the increasing world population and rise of water needs (Boretti and Rosa, 2019). The water of the earth contains 97% of salt which cannot be used directly without treatment while just 3% is fresh water (Bureau of reclamation California, 2020). On the other hand, two third of this is ice-covered in glaciers and polar ice caps (Kalogirou, 2005). The residual freshwater is groundwater, with a small portion above the ground or in the air (USGS, 2019). With this small proportion of the water available for use, the reuse of the wastewater becomes necessary to fulfil the requirements of the society (Grupo Banco Mundial, 2020). According to the Eurostat statistics explained the main water consuming industries are manufacturer of food products, textiles, paper and pulp, refined petroleum products, basic metals, automotive, construction, electricity, and mining sector. **Figure 1.1** represents Eurostat statistics explained about the contribute of industrialised categories in the total water use in industry (%) in different countries.

	Manufacture of food products	Manufacture of textiles	Manufacture of paper and paper products	Manufacture of refined petroleum products, chemicals and chemical products	Manufacture of basic metals	Manufacture of motor vehicles, trailers, semi-trailers and of other transport equipment	Other manufacturing	Construction	Production and distribution of electricity (incl. cooling purposes)	Mining and quarrying
Belgium (2009)	2.2	0.1	0.9	16.6	2.2	0.0	0.7	0.0	76.5	0.8
Bulgaria (2011)	0.7	0.1	0.6	1.9	0.5	0.1	0.8	0.1	94.6	0.6
Czech Republic	1.5	0.5	4.5	10.5	3.0	0.1	1.3	0.0	75.4	3.3
Germany (2010)	1.6	0.1	1.9	10.7	2.6	0.2	1.2	0.0	78.3	3.4
Spain (2010)	3.2	0.4	2.0	5.9	2.5	0.2	0.9	0.4	84.4	0.1
Cyprus (2010)	0.2	0.0	0.0	0.0	0.0	0.0	0.2	0.0	99.4	0.1
Latvia (2007) (1)	10.4	9.4	0.2	4.1	16.8	0.5	4.4	1.3	52.2	0.7
Lithuania (2011)	2.9	0.5	0.6	7.7	0.0	0.0	0.9	0.0	87.3	0.2
Malta (2009) (1)	58.3	8.3	0.0	8.3	0.0	8.3	16.7	0.0	0.0	0.0
Netherlands (2010)	2.0	0.0	0.7	21.5	2.0	0.0	0.5	0.0	73.3	0.0
Poland (2011)	1.0	0.1	1.2	5.1	0.5	0.0	0.8	0.1	90.6	0.7
Slovenia (2011)	10.4	1.5	31.4	24.5	15.5	1.6	12.8	0.0	0.4	2.0
Sweden (2010)	0.5	0.0	7.0	4.3	2.8	0.1	0.5	0.0	84.6	0.1
Norway (2009)	3.2	0.1	16.8	46.0	14.3	0.2	11.9	3.4	0.0	4.0
FYR of Macedonia (2009) (1)	90.4	0.3	3.4	4.5	0.9	0.3	0.2	0.0	0.0	0.0
Serbia (2011)	0.6	0.0	0.1	0.4	1.1	0.1	0.3	0.0	97.1	0.3
Turkey (2010)	3.8	2.4	0.5	2.3	15.6	0.1	1.5	0.6	72.3	0.9

Figure 1.1: Eurostat statistics explained about the share of industrial categories in the total water use in industry (%) in different countries.

According to these statistics, the treatment and reuse of water effluent from the industries is essential in order to maintain the daily production processes of the industries (Richards, Baker and Iwuoha, 2012). A high number of water streams now contain heavy metals such as lakes and rivers because of the industrialization. Hazardous contaminants including dye and heavy metals are frequently found in effluent from the paper and textile sectors. To colour the products, thousands of various commercial dyes are utilised in the textile, culinary, paper, leather, and other industries. Every year, about 700,000 tonnes of effluent trash are produced. It is accepted that these colouring substances are greatly influencing water quality. The first chemical discovered in wastewater is the colour. Even at levels below 1 ppm, the presence of certain colours in water is highly visible and harmful. Arsenic (specific gravity 5.7), chromium (specific gravity 7.19), iron (specific gravity 7.9), cadmium (specific gravity 8.65), lead (specific gravity 11.34), and mercury (specific gravity 13.54) are a few well-known, significant poisonous metallic metals. Garments sections have received criticism for being among the worst polluters of toxic waste in the textile sector (Sruthi and Shabari, 2018). The WHO permissible limit for these heavy metals in drinking water is 0.01mg/L, 2mg/L, 0.003mg/L, 0.3mg/L respectively (Arshad Ali, 2018).

To assess the concentration of heavy metals in discharge samples collected from textile mills, numerous investigations were conducted. We can infer that wastewater from the textile industry contains some amount of heavy metals. Those notorious heavy metals are, Zinc (Zn), Nickel (Ni), Chromium (Cr), Copper (Cu), Cadmium (Cd), and Lead (Pb). Effluents from textiles comprehend a significant amount of these metals. When this effluent is discharged onto the ground, it becomes a component of the surface water that eventually leaches into the groundwater and causes contamination owing to the build up of toxic metallic elements. Thus, industrial wastes produce a wide-ranging ecological challenges and dangerous health dangers.

Heavy metals are lethal and non-decomposable. These heavy metals accumulate in people's bodies and the food chain, which leads to serious health and environmental problems (Al-Malack and Basaleh, 2016). Heavy metals are dangerous to the health as they cause emphysema, hypertension, renal impairment, and skeletal abnormality in foetuses (Pourbeyram, 2016). Cadmium ions, Cd^{2+} are extremely poisonous and they are the sixth most lethal element that disturb human healthiness. Cd^{2+} adds up into water bodies from several different ways as a result of industrial activities for example, smelting, metal plating, contamination by phosphate fertilizers, mining, and seepage from hazardous waste spots. The

excess of Cd²⁺ ions cause numerous acute and chronic syndromes, for example, nausea, diarrhoea, abdominal distress, and improper functioning of testicles etc. (Khan *et al.*, 2013).

Lead ions also exist in effluent water from textile industry. When these ions are released into environment, they have chances to get mixed to food chain through water, soil and air pollution (Sruthi and Shabari, 2018). Lead ions present adverse effects on human health. Chronic exposure to lead disturbs the nervous system, mainly during its development. It creates neurocognitive, psychiatric, and behavioural problems. It also weakens renal and reproductive functions. It is the cause of anemia, vitamin D levels deficiency and increased risk of hypertension.

Various approaches have been used for the deletion of heavy metals from water such as ion exchange, oxidation, irradiation, electro-chemical processing, membrane filtration, photo-chemical, adsorption etc. shown in Table 1.1 (Fu and Wang, 2011). From these, adsorption is distinguished due to economical, effective, and easily operatable way for the heavy metal removal applications. Adsorption is the process of molecules, ions, or atoms from a gas or liquid adhering to a surface. The adsorbent's surface is covered with a layer of the adsorbate material as a result of this process and the substances get bound to the solid surface by chemical and physical interactions (Turki, 2022). Adsorption is widely used because it is simple to use, versatile in design and method, unaffected by harmful compounds, reversible, and the adsorbents can be recovered using the right desorption procedure (Pourbeyram, 2016).

Table 1.1 represents merits and demerits of heavy metals removal methods from aqueous phase (Ariffin *et al.*, 2017)

Table 1.1: Merits and demerits of heavy metal removal methods from aqueous phase.

Removal Methods	Merits	Demerits
Oxidation	Fast	By-products formation High energy cost
Adsorption	Design flexibility Insensitive to toxic pollutants Easy operation	Requires regeneration of adsorbents
Ion exchange	Can remove large range of heavy metals	Demands regeneration of adsorbents
Membrane filtration	Can remove wide range of heavy metals	Expensive

		Formation of by-product as concentrated sludge
Ozonation	Applicable in gaseous state	Short half life
Flocculation	Cost effective	High sludge formation Large size particles form
Electrochemical treatment	Fast Successful for the removal of metal ions	Expensive Large size particles form
Biological treatment	Productive for the elimination of some heavy metals	Not yet commercialized
Fenton's reagent	Hydrogen peroxide activation does not need energy input Can treat different wastes	Produces waste/sludge
Electrokinetic coagulation	Cost effective	Large sludge production
Irradiation	Effective at laboratory level	Requires excess of dissolved oxygen
Photo-chemical treatment	No sludge formation	Formation of by-products

1.2 Membrane separation

The membrane filtration has been widely used in waste water treatment. PSF-based membrane is the most commonly used membranes among others for the ultra-filtration of wastewater due to its resistance to high temperatures, mechanical strength, and exceptional film-forming nature (Richards, Baker and Iwuoha, 2012). The drawback of this membrane is the membrane fouling caused by hydrophobicity. The membrane contamination is the accumulation of organic impurities in water onto the surface of membrane. These contaminants have aquaphobic nature. Much research is being performed to investigate and ameliorate the hydrophilicity of the polysulfone membranes. In order to reduce membrane fouling by increasing the hydrophilic character of the polymer matrix, metal oxide nanoparticles have recently been combined with it (Phelane, 2013).

Due to its enormous surface area, high aspect ratio, porosity, adjustable surface functional groups, and strong interfacial activity, nano-adsorbents have become a hot topic in study. A useful inorganic functional material called zinc oxide nanoparticle (ZnO) exhibits H₂, CO, and CO₂ adsorption efficiency. Zinc oxide nanoparticle is also very cost efficient as compared to other nano adsorbents as Al₂O₃ and TiO₂ (Zhang *et al.*, 2014). Due to its high chemical stability, low cost, abundance, and non-toxicity it is considered as one of the most promising adsorbents in wastewater treatment technologies (Naseem and Durrani, 2021).

Nickle oxide is a functional material which has gather attention of researchers due to its electrical, optical, structural, and catalytic properties (Dehmani and Abouarnadasse, 2020). Moreover, graphene oxide (GO) has also wide applications in several fields, such as medicine, environmental remediation applications and electrode modification because of its unique properties and structure (Khandegar, Kaur and Chanana, 2021). Graphene oxide is an oxidised form of graphene containing a variety of oxygenated functionalities, such as carboxylic acid and carbonyl groups at the sidewalls and hydroxyl and epoxy groups at the base. Heavy metal ions get attach effectively on the GO surface by lone pair sharing of electrons on the oxygen. Due to this reason, it becomes an efficient adsorbent to make the water free from heavy metal ions (Mukherjee, Bhunia and De, 2016).

In this research, the influence of (GO), (ZnO-GO) and (ZnO-GO-NiO) composites conjugated with the PSF membranes for the formation of (zinc/graphene/nickel) oxides MMMs is evaluated. The synthesized membranes were examined for cadmium and lead ions adsorption from textile wastewater. Mixed matrix membrane is a composite membrane in which some inorganic substances are dispersed in the polymeric matrix. With higher surface charge and adsorption capacity, the inclusion of inorganic materials has several benefits that boost the denunciation of heavy metal ions while maintaining a high permeate flux (Mukherjee, Bhunia and De, 2016). As a result of the high negative charge on the graphene oxide sheets, which is prone to strong repulsive activities, the impregnation of GO on ZnO-NiO was intended to demonstrate a good distribution of nano-adsorbents and prevent the buildup of ZnO-NiO (Peng *et al.*, 2017).

1.3 Problem statement

According to (Kolbasov *et al.*, 2017), huge population in the world exceeding the number of four billion will not have adequate amount of pure water to live till 2025. The major reason of water scarcity is the constant increase of water pollution by the addition of heavy metals in

lakes and rivers due to industrialization such as mining, metallurgical, electroplating, alloys and steel production, electronics, etc. (Kolbasov *et al.*, 2017). The non-degradability of the heavy metals makes them to last in the environment for many years. Hence, remediation measures must be needed to resolve this issue. In the past, different wastewater treatment techniques were developed and employed which included biological and chemical treatment, for example, adsorption, ion exchange, ozonation, electro dialysis etc. (Kolbasov *et al.*, 2017). Recently, the adsorption process by making a composite of nano-adsorbents has grabbed attention because of its cost effectiveness and efficiency for the heavy metal separation from water. On the other hand, nano-adsorbents cause agglomeration in aqueous solutions during the adsorption process although they are cheap and it's difficult to regenerate these nano-adsorbents from the water. Hence, it has been suggested that the fusion of both processes i.e., problematic regeneration can be resolved using the membrane separation technique and adsorption. Furthermore, the agglomeration of adsorbents can also be avoided with this combined process (Kolbasov *et al.*, 2017). This study focuses on the adsorption of cadmium (Cd^{2+}) and lead (Pb^{2+}) ions, by using ZnO-GO and ZnO-GO-NiO PSF MMMs under varying conditions from textile wastewater. The primary reason for integrating ZnO/NiO to GO was to target proper diffusion of ZnO/NiO in the polymer mixed matrix.

1.4 Aims and objectives

The aim of the study is to create PSF-based MMMs (ZnO-GO) and (ZnO-GO-NiO) and investigate its adsorption potential for Cd^{2+} and Pb^{2+} from textile wastewater. The main objectives are as follows:

- i. Synthesis and characterizations of nanoparticles, graphene oxide (GO), nano zinc oxide (ZnO), (ZnO-GO) and (ZnO-GO-NiO) composite used as nano-adsorbents
- ii. Fabrication of Mixed Matrix Membranes:
 - Preparation of Polysulfone pristine membrane using casting solution method
 - Synthesis of PSF/PEG-4000 based membrane by using different compositions (ZnO-GO) and (ZnO-GO-NiO) by solution casting and phase inversion method
- iii. Characterization of PSF/PEG-based membranes and ZnO-GO-NiO PSF MMMs.
- iv. Examination of adsorption capacity of MMMs for better performance and efficient removal of heavy metal ion (Cd^{2+} , Pb^{2+})
- v. Examination of the percentage removal of cadmium (Cd^{2+}) and lead (Pb^{2+}) ions, by MMMs under various concentrations of heavy metal ions (50-200) mg L^{-1} .

- vi. Evaluation of adsorption kinetics, adsorption isotherms, antifouling characteristics, and regeneration characteristics.

1.5 Scope

The Purpose of this study is to synthesize (ZnO-GO) and (ZnO-GO-NiO) PSF MMMs and to analyse its adsorption capability under various contact times and pH for the removal of cadmium (Cd^{2+}) and lead (Pb^{2+}) ions from textile wastewater. The preparation of graphene oxide was done by hummers method while nano zinc oxide and nickel oxide were prepared from zinc acetate dehydrates and nickel acetate respectively. Polysulfone (PSF), N-methyl-2-pyrrolidone (NMP) and ZnO/GO/NiO composite was casted on flat glass plate using casting blade. Fabrication of the polysulfone membrane was accomplished by phase inversion method. The synthesized films were then vacuum dried at room temperature for 24 hours to remove traces of solvent.

The ZnO/GO/NiO PSF MMMs were placed in Cd^{2+} and Pb^{2+} ions solutions for a specific time interval. The initial and final concentration of Cd^{2+} and Pb^{2+} ions in the solution were then determined using dead end filtration cell. Different initial concentrations of Cd^{2+} and Pb^{2+} were used to examine the adsorption potential by the ZnO/GO and ZnO/GO/NiO PSF MMMs. Additionally, the pH values of Cd^{2+} and Pb^{2+} solutions were changed, and ZnO/GO and ZnO/GO/NiO PSF MMM adsorption capacities were determined. At various contact times, the adsorption capacity of ZnO/GO and ZnO/GO/NiO PSF MMMs was also discovered. The experiment's findings were examined to determine whether the ZnO-GO and ZnO-GO-NiO PSF MMMs were an appropriate adsorption model for the adsorption of Cd^{2+} and Pb^{2+} . It was also possible to access the membrane's performance for desorption and regeneration under ideal circumstances. Additionally, the adsorption potential of ZnO/GO and ZnO/GO/NiO in bulk as well as MMMs was examined. The specifics about the results of experimentation are reported in chapter 4 (Results and Discussion).

1.6 Characterization techniques

The characterization of materials is the process by which the morphological and functional characteristics of specific substances are examined. The objective is to know valuable information about the composites, such as their degree of resistance and reliability for particular applications. **Table 1.2** represents the characterization techniques that were employed to analyse various properties of the polysulfone based ZnO-GO and ZnO-GO-NiO mixed matrix membranes.

Table 1.2: Characterization techniques and their purpose.

Technique	Purpose
XRD	Used for compound identification and provide information about unit cell dimensions and crystallinity.
SEM/EDX	Observes surface texture, morphology, and the elemental analysis of samples.
FTIR	Identifies the atomic structure and functional groups identification.
AFM	Measures the surface roughness of the composites.
TGA	Analyse the thermal stability of the mixed matrix membranes.
AAS	Evaluates the concentrations of metallic elements in different materials
Zeta Potential	To measure the surface charge of prepared membranes.
UTM	Check the mechanical properties such as tension, compression.
Contact Angle	Evaluate hydrophilic or hydrophobic nature of the composites.

Chapter 2

Literature Review

2.1 Heavy Metals

Heavy metals are metals with extremely high densities, atomic weights, or atomic numbers. A heavy metal can be characterised based on density in metallurgy, whereas atomic number is the primary differentiating factor in physics. On the other hand, chemists are more concerned with chemical behaviour.

The density of heavy metals is greater than 5g per cubic centimetre. Heavy metals badly effect the health of human beings. Their intake led to harmful health consequences such as reduction in growth, tumour, nervous system destruction and in extreme cases death (Barakat, 2011). Sensitivity to some HMs might result in autoimmunity, in which the immune system of the body itself attacks on the body's own cells. Most common heavy metals which cause this disease are mercury and lead. Furthermore, these can also cause rheumatoid arthritis, kidney failure, nervous damage, and harm to brain cells. HMs attack on the brain and can cause irreversible damage if exposed to higher doses. Because of the consumption of more food by the children than the adults, there are higher chances of the children to get effected (Barakat, 2011). Some HMs found in environment, their origins, and their worst effects on people are described in **Table 2.1**.

Table 2.1: Sources & the effects of different heavy metals.

Heavy metals	Sources	Effects
Copper	Water radiators, antifungal agents, hormone drugs, pesticides, water pipes, drinks from copper brewery tackle, and direct gas water boilers.	Sickness, autism, stammering, high blood pressure, mental syndrome, arthritis, anaemia, hyperactivity, liver swelling and inflammation, cystic fibrosis, and heart attack.
Nickel	Zinc base casting runoff, silver refineries, storage batteries & electroplating industries	Bone cancer, lungs cancer, nose cancer, headache, dermatitis,

		myocarditis, breathing issues, vertigo, vomiting
Chromium	Fabric industry and steel manufacturing	Breathing troubles, skin irritations, liver destruction, haemolysis, lung diseases
Lead	Steel industry, mining, automobile, batteries, and colors productions	Brain Pain, vomiting, hyperactivity, mental obstruction, thyroid problem, lethargy, and anorexia.
Mercury	Refineries, sap, crop enrichers, paints, batteries, fabric softeners, pharmaceuticals, and cosmetic industries	Birth defects, tumour, gingivitis, seizures, chromosome destruction, mental obstruction, vomiting, hearing loss, eye, and teeth problems.
Cadmium	Cd-Ni batteries, metallic coating, mining, stabilisers, phosphate fertilizing compounds, pigments, and alloys	High blood pressure, testicular atrophy, renal injury, emphysema, and bone diseases

2.2 Mechanism of Adsorption

The ion exchange, surface complexation and the electrostatic attraction are the three most typical adsorption processes for the adsorption of HMs on the surface of graphene oxide (Peng *et al.*, 2017). Figure 2.1 shows the molecular structure of GO (Chung *et al.*, 2013). GO is consisting of functional groups i.e. -COOH, OH, C=O, and -O-, which provides active sites (Mensah *et al.*, 2019a). HM ions adsorption onto nano-ZnO involves both ion exchange and electrostatic attraction (Ray and Shipley, 2015).



Figure 2.1: Molecular formation of graphene oxide (Chung et al., 2013)

2.2.1 Mechanism of Ion Exchange

The activation between HM ions and proton on GO and ZnO's oxygeneous groups, i.e. -OH, or -COOH, is known as ion exchange. Its adsorption methods are extremely quick and reversible. According to (Peng *et al.*, 2017) the adsorption mechanism is based on the interchange of H⁺ and heavy metal cations on the oxygeneous groups. Following are the results of the reaction between Pb²⁺ and proton on oxygeneous functional groups in graphene oxide:



2.2.2 Electrostatic Attraction

The mainspring for the electrostatic attraction between the positively charged heavy metal ions and negatively charged ZnO/GO/NiO sheets is adsorption. This electrostatic force plays important part as a driving force in adsorption (Peng *et al.*, 2017). Figure 2.2. illustrates the electrostatic attraction and the mechanism of ion exchange between graphene oxide and heavy metal ions. It shows a web like structure.

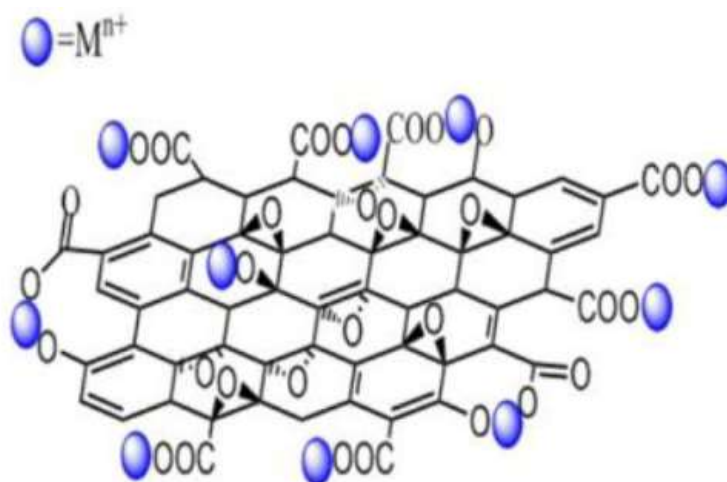


Figure 2.2: Ion Exchange & Electrostatic Attraction between GO and heavy metal ions (Peng *et al.*, 2017).

2.2.3 Surface Complexation:

Research proves HM ions adsorption on surface of GO also involves surface mechanism (complexation) (Liu *et al.*, 2019). Figure 2.3 shows how the surface complexation is implicated in the adsorption of heavy metal ions on GO. For instance, the Pb (II) and the Pb^{2+} linked GO are complexed by the oxygenous functional groups positioned at the margins of Graphene oxide sheets by immediate linkage of the -COOH or -OH at active sites (Peng *et al.*, 2017).

Models of surface complexation are basically chemical models that use an equilibrium method to provide a molecular description of the adsorption mechanism. Because they take into account the charges on both the adsorbent and adsorbing species, these surface complexation models have advanced and gained significance (Goldberg, 2013). Based on surface equilibrium, surface complexation models provide an explanation for sorption. Constant capacitance model (CCM), diffuse layer model (DLM), and triple layer model (TLM) are the three most popular surface complexation models (Goldberg, 2013)

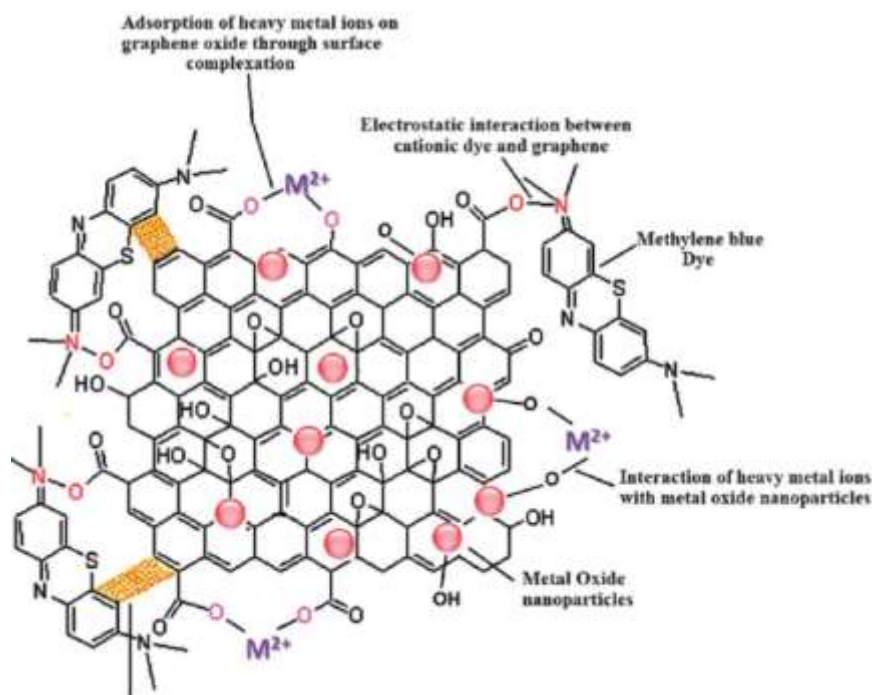


Figure 2.3: Heavy Metal Ions adsorption on graphene oxide via surface complexation. (Upadhyay et al., 2014)

2.3 Polysulfone Membranes

The organic polymer (Polysulfone) is commonly employed due to its various characteristics such as chemical, thermal, and mechanical strength, and resistance to oxidation (Tiron *et al.*, 2017). Figure 2.4 displays the chemical structure of PSF. Polysulfone membrane is stiff, strong, clear, and high-strength thermo-plastic resin which shows resistance to temperatures even above 160°C (Huang and Yang, 2006). It is now replacing extensively used cellulose acetate membrane due to its chlorine oxidation repulsion property (Majewska-Nowak, 1989).

PSF is an ion exchange membrane used in electro dialysis and MMMs electrolysis (Huang and Yang, 2006). Along this, PSF is also utilized as a thermos-plastic substance in ultrafiltration procedures for the fabrication of the membranes (Huang and Yang, 2006).

Various studies are conducted to improve the affinity of polysulfone-based membranes for water. The procedure of fusing PSF and NPs has grabbed the attention in the few years due to their easy processing and moderate operating conditions. The combination of nanoparticles creates artificial membranes that shows better separation efficiency as well as chemical and heat resistance. Moreover, it also shows improved adaptableness in harsh wastewater conditions (Richards, Baker and Iwuoha, 2012).

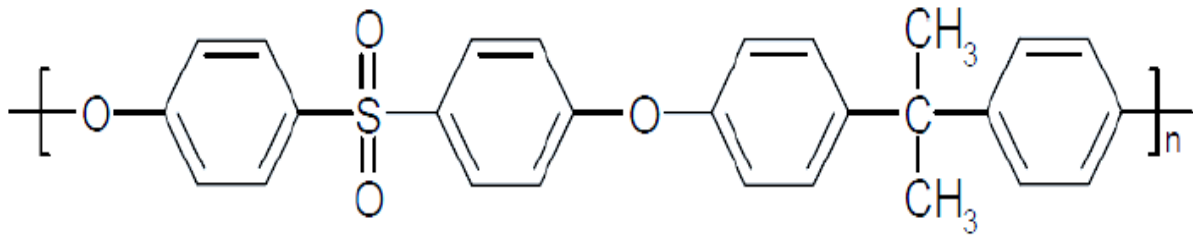


Figure 2.4: Chemical structure of Polysulfone (PSF)

2.4 Adsorbents used for removal of heavy metal ions

2.4.1 Metal and Metal Oxides

Currently, various metals with their oxides i.e. (Zr), ZnO, (Fe₂O₃), and (Al₂O₃) employed as adsorbents for HM ions removal from wastewater. These metals displayed better adsorption efficiency for heavy metal ions removal due to their hydrophilicity, high flux recovery ratio, and high surface area-to-volume ratio. ((Mukherjee, Bhunia and De, 2016); (Khandegar, Kaur and Chanana, 2021); (Zhang *et al.*, 2014); (Mensah *et al.*, 2019a). The modification of different adsorbents and their adsorption performance for heavy metal ions on specific operating condition are showed in Table 2.2.

2.4.1.1 Zirconium (Zr)

Zirconium (Zr) is a cationic (metal) having more current stability and less poisonousness. In the recent years it has been recognized for the removal application of HM ions because of its strong ionic or coordinative affinity for oxygen containing groups (Pourbeyram, 2016). According to the results of (Nermen N. Maximous, 2010), (ZrO₂/PES) and (Al₂O₃/PES) membrane represented more removal for Pb²⁺, Cr³⁺ and Cd²⁺ at 7 pH and low transmembrane pressure of 0.7 bar. 5 wt. % metal oxides dosage represented removal capacity of (Al₂O₃) for Pb²⁺ very close to ZrO₂. ZrO₂ showed 5.2 % better removal efficiency of Cr³⁺ than Al₂O₃. While Al₂O₃ showed better performance i.e., 2.2% added than ZrO₂ for the removal of Cd²⁺. Although both ZrO₂ and Al₂O₃ have analogous removal efficiencies and both are suitable to utilize for the removal of Pb²⁺, Cr³⁺ and Cd²⁺ ions from wastewater. It was also found that a lesser gap condition is achieved by these membrane as compared to other adsorbents such as activated carbon, maize leaves, and rice husk). Their less maintenance cost and membrane fouling control is also very advantageous (Nermen N. Maximous, 2010).

Along with the heavy metal adsorption, Zr has also fluoride removal capability. As the fluoride is an important element for all living organisms. World Health Organization (WHO) has included it in the list of the contaminants in groundwater. The highest tolerable amount of fluoride in water is almost 1.5 mgL^{-1} (He *et al.*, 2016). The excessive amount consumption of fluoride via liquids and food can become the cause of various syndromes which include fluorosis of bones, and fatal retroflex role (He *et al.*, 2016).

2.4.1.2 Zinc Oxide

Nano ZnO is a white-colored inorganic substance. Nano-ZnO is less expensive than other nano-adsorbents as Al_2O_3 and TiO_2 (Zhang *et al.*, 2014). The research of (Zhang *et al.*, 2014) revealed that when compared to pure PVDF films (9.83 ug/cm^2), PVDF/ZnO hybrid membranes with 3 wt% ZnO demonstrated the highest capacity for Cu^{2+} adsorption (87.4 ug/cm^2). It was nearly nine times less when the pH was 6, the equilibration duration was 120 minutes, and the initial concentration of Cu^{2+} was 20 mg/L. Additionally, as shown in Figure 2.5, the contact angle decreased as ZnO nanoparticles were added, improving the hydrophilicity of the membrane surface (Zhang *et al.*, 2014).

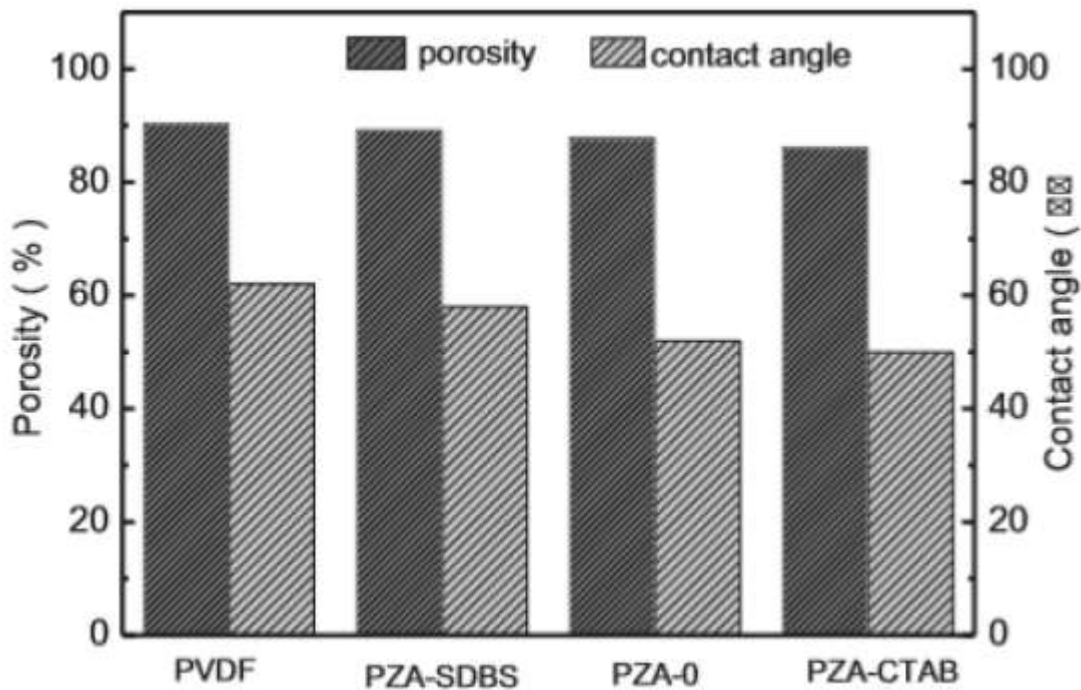


Figure 2.5: Water Contact Angle and Porosity comparison of PVDF/ZnO Hybrid Membranes. (Zhang *et al.*, 2014)

2.4.1.3 Iron and Iron Oxide

(Kolbasov *et al.*, 2017) synthesized a nanofibrous membrane which contained nanoparticles of Fe_3O_4 (0-4 wt.%) filled with the double layers of chitosan/PVA/PES. The outcomes revealed that the maximum adsorption capabilities in a binary system at the pH of 3 were analogous for Cr^{4+} and Pb^{2+} ions (509.7 mg/g for Cr^{4+} ions and 525.8 mg/g for Pb^{2+} ions). The ability to reuse the Nanofibrous membrane in adsorption and ultrafiltration procedures for three cycles demonstrated the manufactured nanofibrous membranes' great capability. This proved that this nanofibrous membrane is good for industrial use as confirmed in **Figure 2.6** (Kolbasov *et al.*, 2017).

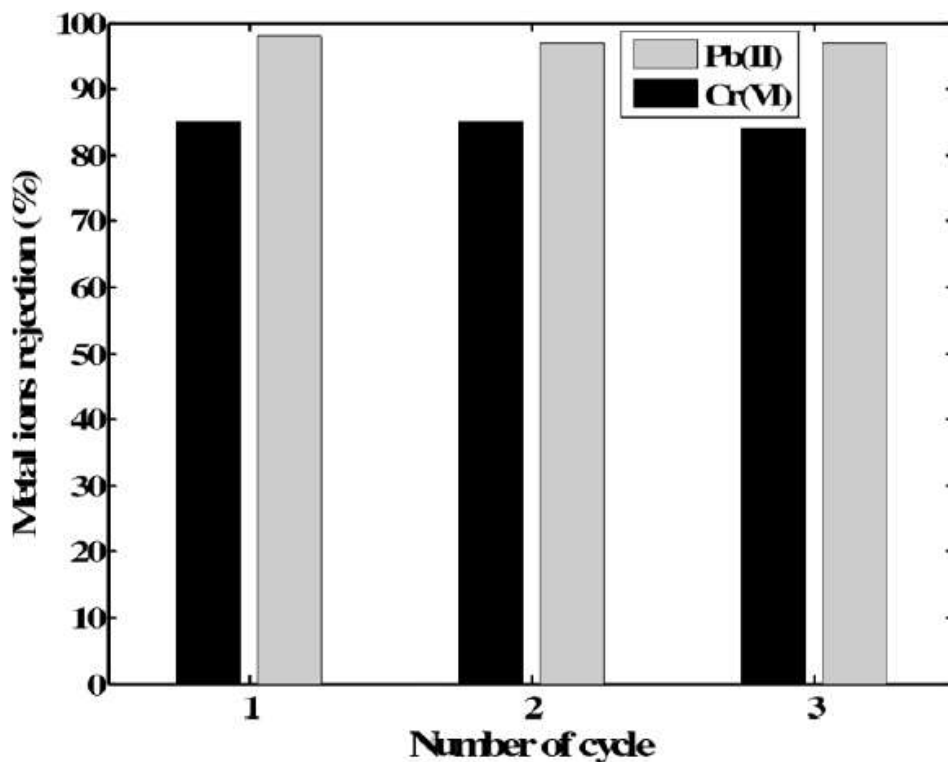


Figure 2.6: For three cycles, the reusability of a nanofibrous barrier in adsorption and membrane-based procedures was investigated (Kolbasov *et al.*, 2017).

Moreover, iron metal can be applied for the removal of phosphorus to prevent extreme amount of phosphorus in industrial discharged water bodies which results in the eutrophication and algal bloom symptoms. By lowering phosphorus conc. in the discharged water from 0.1 mg P/L, eutrophication can be prevented (Johir *et al.*, 2016). According to research findings from (Chae *et al.*, 2021), Fe-Ti bimetal oxides treated with sulfonated polymer beads demonstrated significant phosphate ion removal effectiveness (selectivity factor >25) in comparison to other ions like Cl^- , NO_3^- , and SO_4^{2-} . Additionally, it achieved a metal adsorption efficiency of 7.14 mg P/g to 59 mg P/g with a molar percentage of Ti to the total molar concentration of the

bimetallic system. (i.e., Fe and Ti) 48-hour reaction time, 30 mL synthetic feed water, and a 25°C temperature difference ranged from 0% to 6%. This outcome confirmed that the Ca ion can aid in phosphate association during surface coordination. This will result in more phosphorus binding than phosphate can receive through direct coordination. With the use of beads, approximately 97% of the phosphorus was recovered during the recovery procedure, which required 1.2 eq NaOH per L bed. Another positive sign was the high rate of recovery (Park et al., 2017).

2.4.2 Carbon Sources

2.4.2.1 Graphene Oxide (GO)

Graphene oxide nanoparticles have grabbed the interest of scientists in research areas of nanocomposites and substantial disciplines fields because of its outstanding electrical, physical, and mechanical features. High surface area and functional groups (OH, -COOH, -O- and C=O) of GO are the reason behind its homogeneous dispersion in water and organic solvents (Mensah *et al.*, 2019b). In the recent research, graphene is now emerged as highly selective permeable membrane having sub-nanometre pores which also possess resistance to chemicals, heat, and mechanical endurance (Khandegar, Kaur and Chanana, 2021).

(Mukherjee, Bhunia and De, 2016) made the graphene oxide (GO) infused MMM with the 0.1, 0.2, 0.35 and 0.5 wt.% dosage of graphene oxide. In the conclusion of the research, it was learnt that high adsorption capacity for various metal ions was as follows: Pb²⁺ (79 mg/g), Cu²⁺ (75 mg/g), Cd²⁺ (68 mg/g) and Cr⁶⁺ (154 mg/g) at pH= 6.7, 6.5, 6.4 and 3.5 and so forth. The operational parameters throughout the experiment were set at a 50 mg/L feed concentration, a 414 kPa TMP, and a 40 L/h crossflow rate. The decrease in contact angle, from 83° to 70°, indicated that the membrane was becoming more hydrophilic. The restoration of the MMM was done by washing with a 5.5 pH acidic solution for 60 minutes. And recovery of MMMs over 0.9 indicated that membrane shows high recovery in both adsorption and desorption processes (Mukherjee, Bhunia and De, 2016).

(Khandegar, Kaur and Chanana, 2021) Rejection rate of graphene oxide/iso-phorone diisocyanate (GO-IPDI) membranes for rhodamine-B (RB), methylene orange (MO), and Congo red (CR) was reported to be 97.6%, 96.2%, 96.9%, and 98.24%, respectively, when the dosage of graphene oxide was fixed at 10 mg. When the operation parameters were set to 1 bar pressure, pH=7, and 10 mL of 10 mg/L concentrated dyes feed solution, the rejection rate of GO-IPDI membranes for Cu²⁺, Pb²⁺, Cr³⁺, and Cd²⁺ ions were 46.2%, 66.4%, 71.1%, and 52.8%, respectively. The GO had a contact angle of 26°, but GO-IPDI membranes had a contact

angle of 53°. This demonstrated that the decline in the hydrophilic functional decreases the rejection rate of GO-IPDI membrane as compared to GO membrane as shown in Figure 2.7 (Khandegar, Kaur and Chanana, 2021). According to (Khandegar, Kaur and Chanana, 2021), the activity deficiency might be the result of decrease in the size of HM ions in comparison to the interlayer of the GO-IPDI. Therefore, it restricted the physical sieving for the rejection of metal ion. Moreover, the addition of IPDI might resulted in the consumption of surface oxygen functional groups of graphene oxide. Notable gaps can be noticed due to feeble interaction of the GO when that membrane no fabricated with IPDI. The surface of membrane was completely unaffected after the introduction of IPDI to GO layers for the formation of GO-IPDI membrane.

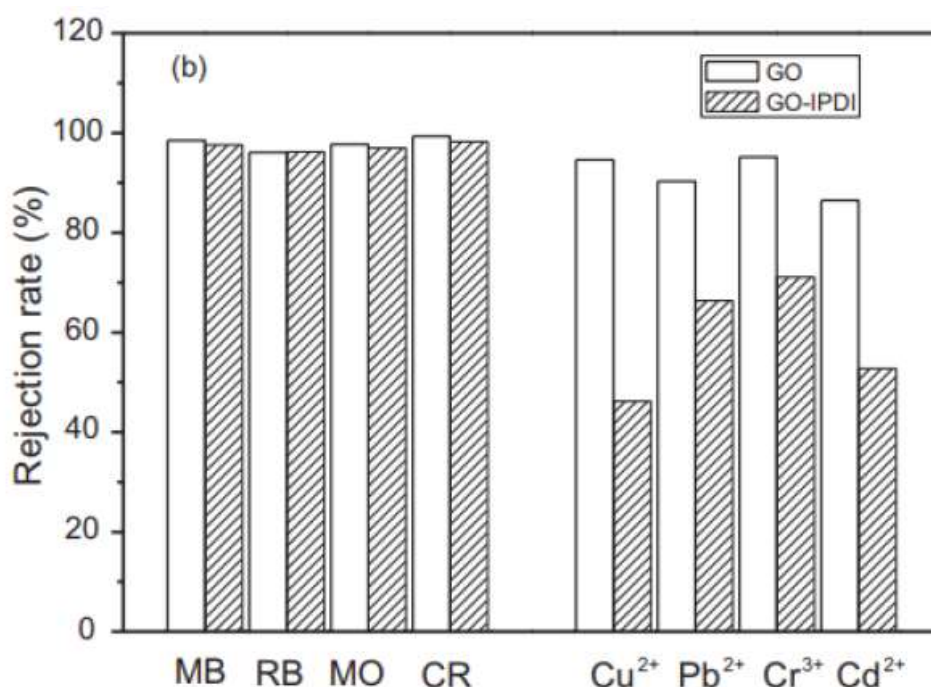


Figure 2.7: Rejection Rate of the Heavy Metal Ions (Cu²⁺, Pb²⁺, Cr³⁺ and Cd²⁺) and Dyes for Pure GO Membrane and GO-IPDI Membrane (Khandegar, Kaur and Chanana, 2021).

This proved GO-IPDI a good membrane for removal of HMs due to its outstanding constancy. The strength of the chemical bonds between GO nanosheets which was further reinforced by IPDI linkers were the main reason behind the stability of the membrane, which was beneficial to avoid the peeling off of the membranes from PVDF surface (Khandegar, Kaur and Chanana, 2021).

Table 2.2 The PSF-based nanocomposite membranes (PSF/PEG/GO blended membranes) used for the cadmium (Cd²⁺) and lead ions (Pb²⁺) removal.

Membrane	Initial conc. (mg/L)	Flux (Lm²/h)	Feed soln. pH	Removal Efficiency (mg/g)	Reference
PSF + 0.2 wt% GO	50	38.5	6.7	79.00	(Mukherjee, Bhunia and De, 2016b)
PSF + Zeolite nanoparticle	100–500	60.0	6.0	682.00	(Yurekli, 2016)
PSF + NiFe ² O ³	50	0.55	7.0	52.11	(Mrinmoy Mondal, 2017)
PES + Humid MnO	1000	573	7.0	204.10	(Jamshidi Gohari, 2013)
PSF + 0.5 wt% GO	50	163.71	5.5	98.24	(Ravishankar, Christy and Jegatheesan, 2018a)
PSF + Hydrous FO	10–50	942	7.0	13.20	(Abdullah <i>et al.</i> , 2016)
PSF + Biochar	0.21	132	5.0	89.96	(Jinsong He, 2017)
PVA + PVDF + Zr phosphate	1–100	87.9	5.5	121.20	(Dandan Zhao, 2016)
PSF + Amide functionalized MWCNT	1	12,600	2.6	90.00	(Mondal and Kumar Majumder, 2020b)
PSF + Poly 6-methyl 2-vinyl pyridinium sulfate	1000	216.36	6.0	87.81	(Kalaiselvi <i>et al.</i> , 2013)
PSF + PAA	4.9	36.0	6.0	99.00	(M'Bareck <i>et al.</i> , 2006)
PSF + Sulfanilic acid-poly(vinylchloride)	10	0.1	7.0	91.00	(Nayak <i>et al.</i> , 2016a)
PSF + PVC modified by 4-amino benzoic acid	10	2.56	7.0	82.00	(Vignesh Nayak, 2017a)
PSF + PEG + ZnO-GO-NiO (M4_A)	50-200	55.20	5.5	Cd = 354.8 Pb = 308.16	Present study

2.4.2.2 Carbon Nanotube

A hybrid ceramic membrane with hydrophilic nature was synthesized by (Ainscough *et al.*, 2017) which was integrated with carbon nanotube (CNT). Adsorption performance of the membrane was found excellent. It showed adsorption efficiency of 99.39% for Cd, 99.61% for Hg, 99.70% for Ni, 99.72% for Co, and 99.97% for pb. Washing with 2 wt.% sodium hydroxides at 50°C and a time period of 1hr and then with 1% citric acid was done in post experiment treatment. The sodium hydroxide was used to take off organic contaminants while citric acid was implied to eliminate inorganic components. During this experiment, only 12% of the original pre-experimental membrane flux was recovered (Ainscough *et al.*, 2017). The study of (Ainscough *et al.*, 2017) determined that the reason behind the permanent contamination of the membrane was motor oil because it blocked the inner pore and surface which was clearly visible on both inner and outer surfaces of the membrane in the form of stains.

2.4.2.3 Activated Carbon

(Nermen N. Maximous, 2010) researched on the activated carbon at the pH of 5 and found that it can attain 98% removal efficiency of lead ions, 95% removal efficiency of Chromium ions and 83% cadmium ions removal efficacy. (Al-Malack and Basaleh, 2016) examined the exclusion of Cd²⁺ and Pb²⁺ ions by activated carbon which was generated from municipal waste. In the study, the best possible adsorption conditions for Cd²⁺ and Pb²⁺ ions removal were found which came out as pH of 5, metal conc. of 100 mg/L, time of contact 180 min and an adsorbent dose of 200 mg in 50 mL of metal solution. Furthermore, the maximum adsorption capacity for Cd²⁺ and Pb²⁺ ions represented by adsorption isotherms were 61 and 90 mg/g, respectively, at the above mentioned operating conditions (Al-Malack and Basaleh, 2016).

2.4.3 Natural Source

2.4.3.1 Chicken Eggshells

Chicken eggshells were employed as an adsorbent material to take off heavy metal ions such as lead, copper, Ni, and zn ions (binti Rohaizar and Sien, 2013); (Mashangwa, Tekere and Sibanda, 2017). Chicken eggshells can adsorb heavy metals present in wastewater because of their high ratio of calcium carbonate. The carbonate groups assist in adsorption on the chicken eggshells because they replace cations with the heavy metal ions (binti Rohaizar and Sien, 2013). Moreover, the porosity of eggshells makes it an attractive material to be used as an adsorbent. The eggshell typically consists of ceramic material, arranged in a three-layered structure. Firstly, the cuticle on the outer surface then a spongy layer and finally an inner lamellar (or mammillary) layer. Almost 90% of the eggshell is composed of the mammillary

and spongy layers which make a calcite (calcium carbonate) bounded matrix composed of protein fibres. The eggshell is an efficient adsorbent because of its two layers that are fashioned in such a way that it contains many circular pores (binti Rohaizar and Sien, 2013).

(binti Rohaizar and Sien, 2013) made chicken eggshells comprised of the 0.5g of chicken eggshell to remove 50mg/L conc. of Cu (II) ions. The studies of the Aimi et al. (2013) showed that the selective adsorption of copper and attraction of adsorbent was 13.8995L/g and this uptake arisen quickly in initial 15 minutes while complete adsorption of Cu²⁺ was achieved after 60 min time period when the pH was 4-8, contact time was 180 min, TMP 30°C, and initial Cu (II) ions concentrations was 50-350 mg/L. the results concluded that 7 pH was the pH while the optimal agitation rate was examined at 350 rpm.

Soon after, (Mashangwa, Tekere and Sibanda, 2017) illustrated that eggshells are cheap and effective adsorbent material for the removal of Pb²⁺, Ni²⁺, Cu²⁺, and Zn²⁺. The maximum adsorptions were 97% for lead, 94% for nickel, 95% for copper, and 80% for zinc from the water with a 7g adsorbent at the pH of 7, optimal contact time 6 hrs, 24°C room temperature and 100 ppm of initial metal conc. (Pb, Ni, Cu, and Zn). The researchers also described that during the initial 120 min the equilibrium points for adsorption was achieved for Pb²⁺ (98.33%) and 270 min for Zn²⁺ (81.24%). Copper and nickel, alternatively, revealed a maximum adsorption ratio of 14.46% and 3.47% at 5 and 6 hrs, respectively.

Chapter 3

Materials & Methods

3.1 General Preview

This chapter explains the synthesis of PSF-based (GO), (ZnO-GO), (ZnO-GO-NiO) mixed matrix membranes for the removal of heavy metal ions from wastewater. The materials and methods for the fabrication of membrane, characterization techniques, adsorption environments, adsorption models, desorption/restoration of MMMs is also described.

3.2 Materials

The polymer materials, Polysulfone (PSF) and Polyethylene Glycol-4000 were ordered from Sigma-Aldrich, having (M.W.) of 35000 and 3500-4500 Da, respectively. N-methyl-2-pyrrolidone (NMP) was employed as a solvent for the dissolution of the polymers and it was delivered by Scientific Hub. Graphene oxide (GO) were synthesised by modified/improved Hummers method, Nano zinc oxide/graphene oxide (ZnO/GO) and Zinc oxide/graphene oxide/Nickel oxide (ZnO/GO/NiO) nano powders were used as nano-adsorbent and the synthesis methods and functionalization procedures are explained in **Fig. 1**. The chemicals required for the synthesis of these nanoparticles and composites were include Graphite powder, potassium permanganate (KMnO_4), hydrochloric acid (H_2SO_4), phosphoric acid (H_3PO_4), hydrochloric acid (HCL) zinc acetate ($\text{Zn}(\text{CH}_3\text{COO})_2 \cdot 2\text{H}_2\text{O}$), Oxalic acid dihydrate ($\text{C}_2\text{H}_2\text{O}_4 \cdot 2\text{H}_2\text{O}$), nickel(II) acetate ($\text{Ni}(\text{CH}_3\text{CO}_2)_2 \cdot 4\text{H}_2\text{O}$), Triton X-100, sodium hydroxide (NaOH), absolute ethanol and deionized water, were supplied by Sigma-Aldrich. The lead and cadmium ions solutions with various concentrations (50 mgL^{-1} , 100 mgL^{-1} , and 200 mgL^{-1}) were made by dissolution of lead nitrate ($\text{Pb}(\text{NO}_3)_2$, M.W. = 331.2 gmol^{-1}) and cadmium nitrate tetrahydrate ($\text{Cd}(\text{NO}_3)_2 \cdot 4\text{H}_2\text{O}$, M.W = 308.49 gmol^{-1}) in deionized water which were utilized in the ultrafiltration membrane experiments.

Table 3.1: Quantity and physical form of the chemicals used in experimentation.

Sr. No	Name of Chemicals	Quantity	Physical Form
1	Zinc Acetate dehydrates [$\text{Zn}(\text{CH}_3\text{COO})_2 \cdot 2\text{H}_2\text{O}$]	0.01g-0.20g (1-5) wt.%	Crystalline
2	Oxalic Acid ($\text{C}_2\text{H}_2\text{O}_4 \cdot 2\text{H}_2\text{O}$)	1 g	Crystalline
3	Ethanol ($\text{C}_2\text{H}_5\text{OH}$)	200ml	Liquid

4	Nickel (II) Acetate [Ni (CH ₃ CO ₂) ₂ ·4H ₂ O]	0.35 g	Crystalline
5	Sodium Hydroxide (NaOH)	0.16 g	Crystalline
6	Triton X-100	0.04 ml	Liquid
7	Polysulfone (PSF)	15 wt. %	Granules
8	PEG-400	5 wt. %	Liquid
9	N-methyl-2-pyrrolidone (NMP)	80 wt. %	Liquid
10	ZnO/GO/NiO nanocomposite	(0.1-0.5) wt. %	NPs
11	Cadmium Nitrate [(Cd (NO) ₃ ·4H ₂ O)]	25 ml	Liquid
12	Graphene oxide	0.3 g	Powder (NPs)

The lead and cadmium contaminated solutions of various concentrations (50 mgL⁻¹, 100 mgL⁻¹, and 200 mgL⁻¹) used in the current ultrafiltration experiments (pore diameters of the membranes reside in the ranges of 10nm to 100nm) were created synthetically by dissolving lead nitrate and cadmium nitrate tetrahydrate in deionized water. 37wt.% HCl (EMSURE® by Merck) and NaOH pellets (R&M Chemicals) were used to maintain the pH of the Cd²⁺ and Pb²⁺ solutions. **Table 3.1** represents the quantity and physical form of the chemicals used in the experimentation:

3.3 Dead End Filtration Unit

Dead End Filtration Unit was used as a filtration assembly that works on the application of the pressure which provides a push to the feed through the membrane filter (Berk, 2009). A particle-free clear filtrate produces as a result of the process that is called permeate. However, the separated particles/contaminants from the feed make a filter cake. In a typical assembly, particle-containing fluid (liquid, gas) is pumped in opposition to the filter medium (PorexFiltration, 2019). Pressure is kept as low as possible to lessen the compaction of the retained substances (Singh, 2015). The constant outflow of the filtrate causes the accumulation of filter cake from the solid particles to be separated on the filter medium (Singh, 2005). Which can also have a positive impact on the filtrate quality because the formation of the filter cake can result in an additional depth filter effect, subject to the pore structure of the filter cake and its permeability (Nagy, 2019).

Figure 3.1 represents schematic depiction for the dead-end filtration unit.

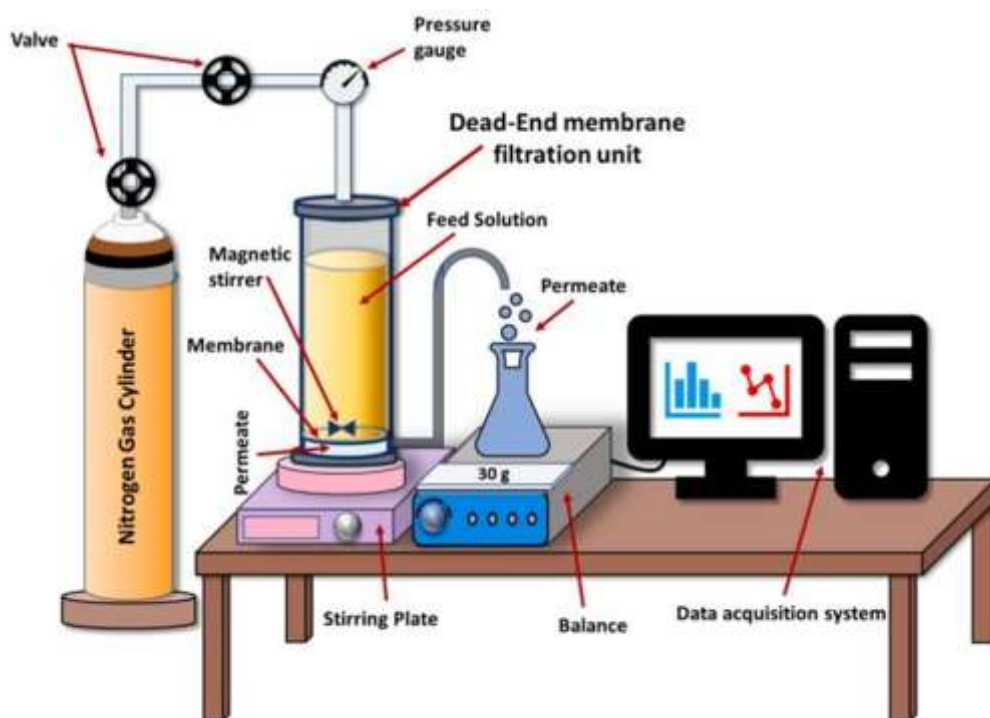


Figure 3.1: Dead-end filtration unit

3.4 Synthesis of nano particles

3.4.1 Synthesis of graphene oxide (GO) by modified hummers' method

Modified, improved Hummers' method was used to produce graphene oxide (GO) from graphite powder. 9:1 ratio mixture of conc. H_2SO_4 and H_3PO_4 was prepared by adding 360ml of sulphuric acid and 40ml of phosphoric acid (Pang *et al.*, 2018). Another mixture of graphite flakes and potassium permanganate was made by the addition of 3g of graphite flakes and 18g of KMnO_4 (potassium permanganate). Both mixtures i.e., the mixture of $\text{H}_2\text{SO}_4/\text{H}_3\text{PO}_4$ and graphite flakes/ KMnO_4 were mixed. For this purpose, both mixtures were slowly poured into one another under constant stirring because this addition results in exothermic reaction (Marcano *et al.*, 2010). The process was followed by heating of the mixture for 12-18 hrs under continuous stirring while temperature was kept in between 45-50°C (Santamaría-Juárez *et al.*, 2019). After completion of the reaction a dark brown, high viscous gel like product was obtained and the resulted mixture was then cooled to ambient temperature by adding 400ml deionized water ice into beaker and stirrer until the ice melted and became liquid (Benzait, Chen and Trabzon, 2021). 5-10ml of 30% H_2O_2 was added dropwise into above prepared mixture till the colour changed to yellow (Yu *et al.*, 2016). The process further moved to filtration and centrifugation to obtain solid material, washing of the product was done by adding 200ml of

30% HCl and 200ml of C₂H₆O by vacuum filtration and centrifugation (Alam, Sharma and Kumar, 2017). This resulted in the formation of solid product. Which was washed with continuous supply of deionized H₂O to achieve the pH of >5 and the attainment of the pH was indicated by the change in colour which turned to be dark brown (Santamaría-Juárez *et al.*, 2019). Filtration/centrifugation was performed to obtain brownish material followed by vacuum drying at 60°C for 24 hrs (Guerrero-Contreras and Caballero-Briones, 2015). **Table 3.2** represents the amount of the chemicals/materials used in the synthesis process of graphene oxide (GO).

Table 3.2: Amount of chemicals used in synthesis of graphene oxide

Chemicals	Quantity
H ₂ SO ₄	360ml
H ₃ PO ₄	40ml
Graphite flakes	3g
KMnO ₄	18g
Deionized water ice	400ml
30% H ₂ O ₂	10ml
30% HCL	200ml
Ethanol	200ml
Deionized water	>5 litres
pH paper	>20

3.4.2 Synthesis of nano zinc oxide (ZnO)

Flower shaped Zn-NPs were prepared by dissolving 4mM zinc acetate dihydrate and 20mM of sodium hydroxide in deionized H₂O (Gusatti *et al.*, 2011a). Firstly, both aqueous solutions were cooled in ice bath and then sodium hydroxide solution was added slowly with the help of peristaltic pump in to zinc acetate dihydrate solution at 550rpm stirring using a propeller (Hong *et al.*, 2006). The resulting turbid solution was heated at 75°C for half an hour using a temperature-controlled water bath and this settled down the white powder at the base (Mahamuni *et al.*, 2019). Which was separated by washing the solution thrice with deionized water. Finally, the prepared mixture was dried overnight in a clean environment at room temperature (Mahamuni *et al.*, 2019).

3.5 Synthesis of ZnO-decorated GO nanocomposite material

Graphene oxide (GO) suspension was synthesized by immersing 0.3g GO in 10mL of absolute C₂H₅OH under sonication using an ultra sonicator at 40KHz frequency (Chauhan *et al.*, 2019). 0.01-0.20g of Zn (CH₃COO)₂·2H₂O was included into 90mL of absolute C₂H₅OH at 65°C for 30min and continuous stirring (Lin *et al.*, 2020). The suspension of graphene oxide was mixed into Zn(CH₃COO)₂·2H₂O and absolute C₂H₅OH mixture and the solution was kept stirring for 20 min at 45°C (P. Kumar *et al.*, 2018). In the end, 1g of C₂H₂O₄·2H₂O dissolved in 50mL absolute alcohol was combined with the above mixture and stirred for 90min (Chauhan *et al.*, 2019). The precipitate was collected by centrifugation and dried overnight in an oven at 65°C. The synthesized product was calcined at 400°C for 3hr to obtain ZnO/GO nanocomposite (Nisar *et al.*, 2022). The nanocomposite weight percentages of ZnO (1, 5, 10 and 20 wt.%) were further made by controlling the quantity of Zn (CH₃COO)₂·2H₂O (Boukhoubza *et al.*, 2020).

3.6 Synthesis of nanocomposite (ZnO-GO-NiO)

ZnO-GO-NiO nanocomposite was prepared in two steps. Firstly, 20mL of 0.16g sodium hydroxide solution was dropped into 20mL of 0.35g nickel acetate solution comprising of 0.04ml of Triton X-100 under continuous stirring (Obodo *et al.*, 2020). 65 mL of deionized (DI) H₂O was then mixed into the above prepared solution at continuous stirring to produce Ni(OH)₂ (Buledi *et al.*, 2023). Secondly, a specific quantity of ZnO-decorated GO was dissolved in 20mL of deionized water through ultra-sonication (Lin *et al.*, 2020). 12 mL of Ni(OH)₂ was mixed into this solution and it was kept stirring for 1hr, then shifted into a Teflon-lined stainless-steel autoclave for hydrothermal processing at 150°C for 6hr (Obodo *et al.*, 2020). After cooling the product to room temperature, the final black solution was washed with DI water and ethanol thrice and sent to oven for drying at 60°C for 8hr (Paul *et al.*, 2021a).

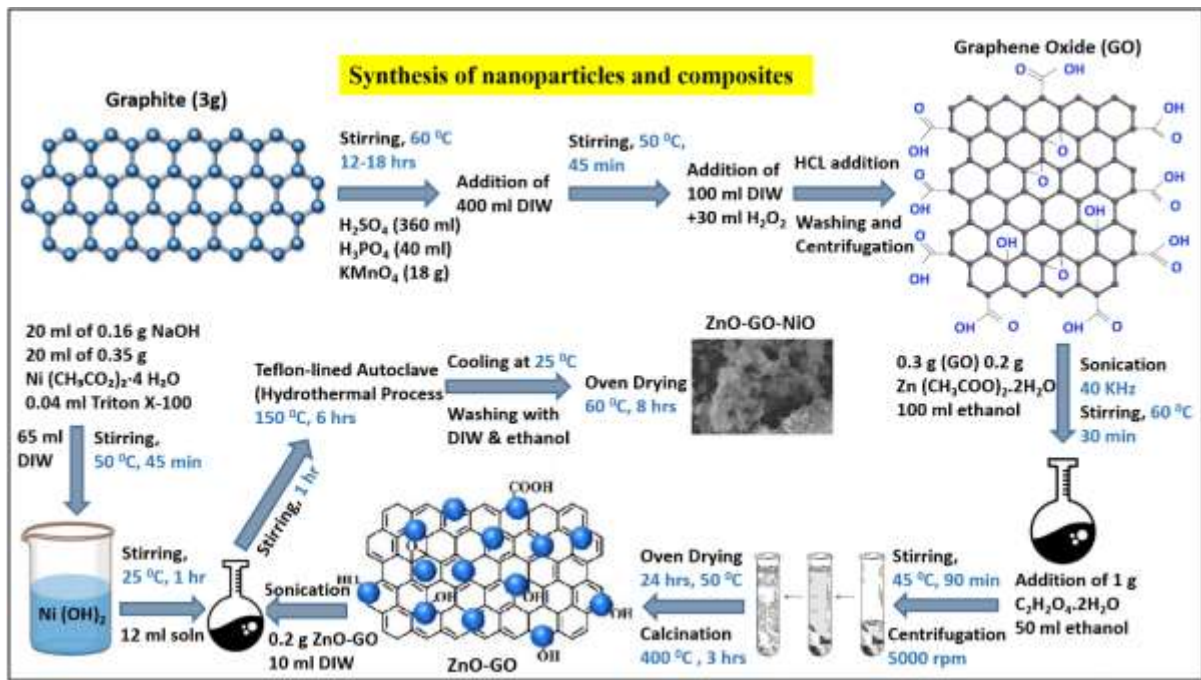


Fig. 3.2. Illustration of the nanoparticles/composites synthesis and functionalization procedures.

3.7 Casting solution preparation

Prior to casting solution preparation, PSF membrane was taken into a 250mL beaker and oven dried at 60°C overnight to eliminate any moisture content (Alasfar *et al.*, 2022a). Firstly, 15 wt.% of N-methyl-2-pyrrolidone was added into a 100mL of beaker and was heated up to 60°C at the heating plate under constant stirring using a magnetic stirrer at a rate of 400-450 rpm (Yeo, Lee and Han, 2000). For pristine membrane, 80 wt.% polysulfone beads and 5 wt.% PEG-4000 mixed with the pre-heated N-methyl-2-pyrrolidone solution using a spatula. A paraffin film was used to seal the beaker and left undisturbed for 5-6hr while stirring until polysulfone (PSF) and PEG-4000 polymers are completely diluted (Paul *et al.*, 2021b). For fabrication of composite membranes, (0.1-0.5) wt.% of GO, ZnO-GO and ZnO-GO-NiO composites were dispersed separately in 10 ml NMP by using sonicator (50 KHz) with the wt.% of PSF and PEG-4000 mentioned in **Table 3.3** into the casting solution and again the mixture was sonicated for half an hour by using probe sonicator for the proper distribution of the ZnO/GO/NiO (Harris and Walczyk, 2006). The synthesized casting solution was of black color due to the existence of black colored graphene oxide nanoparticles and nano zinc oxide (Zhang *et al.*, 2010).

3.7.1 Solution casting method

The first method used for membrane casting is solution casting method showed in **Fig. 3.3 (a)**. Right after probe sonication, the casting solution was poured into a glass petri dish by using solution casting method in order to avoid the hardening of the solution and then left

uninterrupted for 15-20 minutes to remove the entrapped air bubbles (Tiron *et al.*, 2017). This casted solution was then dried in oven with evaporation temperature of 70 °C for 6 hours to completely eliminate the solvent. Porous dried films were obtained having thickness ranges from 50-100µm for different composite membranes (Alasfar *et al.*, 2022b).

3.7.2 Phase inversion method

The second method is phase inversion method represented in **Fig. 3.3 (b)**. After the preparation of casting solution, membranes were casted on a glass plate (flat) with the help of casting blade which was maintained at 200µm thickness (Urducea *et al.*, 2020). In this method, the film and glass plate were submerged in 5L distilled water. After half an hour processing, the membranes were transferred in distilled water bath (Urducea *et al.*, 2020). These membranes were left for 24hr without any disturbance for the completion of the phase inversion procedure (Lee *et al.*, 2003). The subsequent films were vacuum dried for 24hr at room temperature to eliminate the solvent. Finally, 15-25nm pore sized dried films were obtained having thickness range 60-90µm (Wojciechowski *et al.*, 2004).

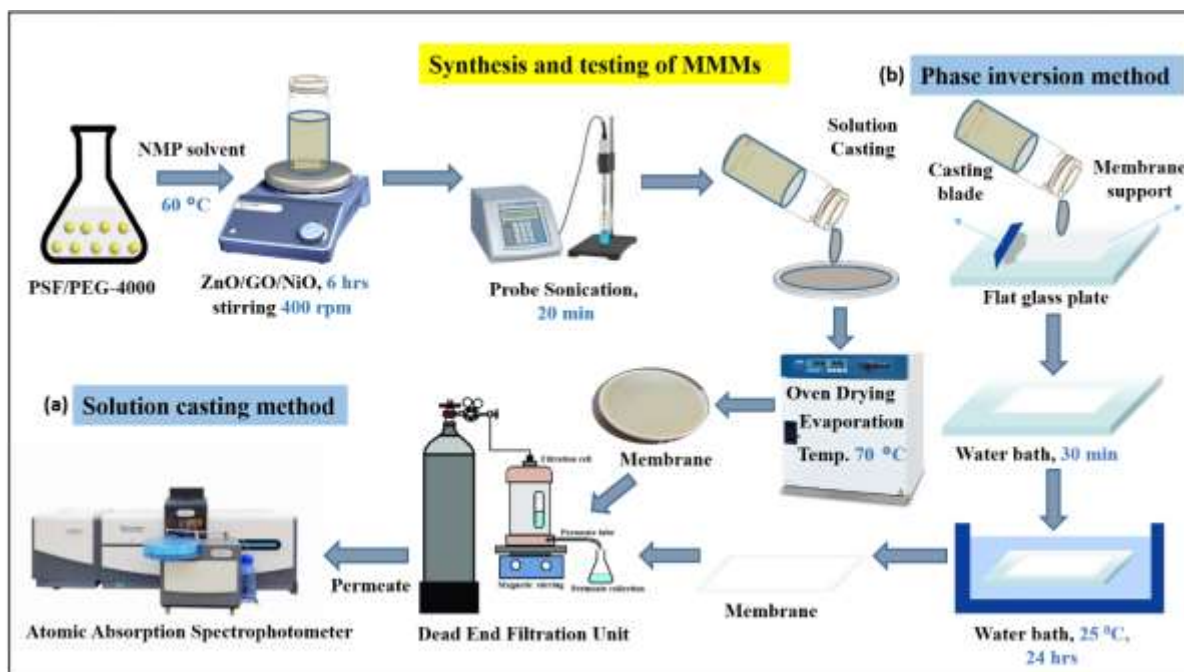


Fig. 3.3: Membrane composition and preparation method (a) solution casting (b) phase inversion.

Table 3.3: Compositions of membrane casting solutions.

Sr. No.	Polysulfone (PSF) (wt. %)	NMP (wt. %)	PEG-400 (wt. %)	Composite (wt. %)	PSF+PEG:NMP:NPs
M1	15	80	5	0	1:4:0
M2	15	78	5	GO 0.2 %	1:4:0.002
M3	15	79.9	5	ZnO-GO 0.1 %	1:4:0.001
M4	15	79.7	5	ZnO-GO 0.3 %	1:4:0.003
M5	15	79.5	5	ZnO-GO 0.5 %	1:4:0.005
M3_A	15	79.9	5	ZnO-GO-NiO 0.1 %	1:4:0.001
M4_A	15	79.7	5	ZnO-GO-NiO 0.3 %	1:4:0.003
M5_A	15	79.5	5	ZnO-GO-NiO 0.5 %	1:4:0.005

3.8 Nanoparticles and membrane characterization

The size, crystal structure, elemental analysis, and a number of other physical features of nanoparticles have all been described using a variety of techniques (Mourdikoudis, Pallares and Thanh, 2018). Physical characteristics can frequently be assessed using a variety of methods and the choice of the best appropriate method is made more difficult by the various advantages and disadvantages of each methodology; frequently, a combinatorial characterisation approach is required (Ibrahim Khan, Khalid Saeed and Idrees Khan, 2019). The efficiency of membranes used in filtration processes depends on factors such as their morphology, porosity, surface features, and physical and chemical properties (Cevallos-Mendoza *et al.*, 2022). The attributes of membranes differ according to their synthesis methods and their final composition which can be improved to achieve the particular features according to their performance such as flux and rejection efficacy (Ray *et al.*, 2020). Even though, other characteristics like fouling, cleaning, and modelling are also crucial to address (Saleh and Gupta, 2016). Hence, the characterization techniques are very important in membrane exploration and improvement process (Bernstein, Kaufman and Freger, 2013b). Chemical composition and physical properties of prepared

membranes, such as their shape, mechanical strength, charge, etc., are determined using several characterization techniques (Gupta, Gandhi and Sapra, 2023). The combination of different characterization techniques also aids with the identification of structure of the membrane and its transportation properties (Cuperus and Smolders, 1991). The two subcategories of characterization approaches are static and dynamic. The static methods provide information on the morphology and structure of the membranes, as well as their chemical and physical characteristics. While studying membrane performance, dynamic approaches are crucial (Tylkowski and Tsibranska, 2015). The current context comprises both traditional and cutting-edge approaches to ascertain the membranes' chemical and physical properties, shape, and porosity, as well as their transport properties, surface characteristics, and antifouling qualities (El Batouti, Alharby and Elewa, 2022).

3.8.1 Scanning electron microscopy (SEM)

The high-resolution imaging of nanoparticles (NPs) with diameters much below (10 nm) is studied by scanning electron microscopy SEM (S4700 Hitachi, Japan). This characterization technique was used to study the morphology, distribution of NPs in cells and other matrices/supports, precision in NPs' lateral dimensions, and fast analysis of their elemental compositions (Mourdikoudis, Pallares and Thanh, 2018). Surface morphology and texture of neat PSF, GO, ZnO-GO and ZnO-GO-NiO PSF-based MMMs prior to the adsorption process and also later than adsorption process was studied by scanning electron microscope (SEM). The samples of the membrane were broken ahead of the SEM analysis by using the liquid nitrogen cracking method (Li *et al.*, 2022). Sample thickness was also determined in the course of the analysis. During the imaging process, 1000x-2500x magnification and 20Kv voltage was used.

3.8.2 Energy dispersive X-ray spectroscopy (EDX)

Energy dispersive X-ray (EDX) analysis was also performed to get the elemental assessment of nanoparticles and membranes of GO/ZnO/NiO, and later the presence of Pb^{2+} and Cd^{2+} in the membranes (Al-Mur, 2023). It is typically used in conjunction to the scanning electron microscopy (SEM). This technique employs an electron beam which is bombarded on the sample to determine the elemental composition of the sample. EDX method identifies the X-rays emitted the analysed volume of the sample (Samal *et al.*, 2022). In this study, synthesised nanoparticles, neat PSF membrane, (0.2) wt.% GO, (0.1-0.5) wt.% ZnO-GO and ZnO-GO-NiO PSF-based MMMs before and after the adsorption were taken as samples.

3.8.3 X-ray diffraction (XRD)

The X-ray diffraction (XRD) analysis was used to examine the composite materials' structural characteristics (Heryanto *et al.*, 2018). A diffractometer (from STOE, Germany) with Cu-K α -1 radiation in the range of 2θ from 20° - 90° was employed for the structural analysis. Samples were pressed into the sample holder, clamped at an angle of 45° and targeted by an incident X-ray beam of 0.154060 nm wavelength. The XRD patterns were formed due to the diffraction of incident X-ray beam into specific directions which demonstrated the nature of synthesized nanoparticles, neat PSF membrane, GO, ZnO-GO PSF MMMs and ZnO-GO-NiO PSF MMMs. During the analysis, 5 steps with the 0.05° step size was used (Ionita, A. Pandele, *et al.*, 2015). The change in the number of steps and step sizes from 1-5 and 0.02° - 0.05° respectively does not brought about any change in the appearance of the peaks. Bragg equation was used to calculate d-spacing between different planes (M Khayet and García-Payo, 2009).

$$d = \frac{\lambda}{2\sin\theta} \quad (1)$$

where θ is called as diffraction angle, and the Scherrer equation was used to calculate crystalline size (D). (M Khayet and García-Payo, 2009).

$$D = \frac{K\lambda}{\beta\cos\theta} \quad (2)$$

The considered value of the Scherrer constant (K) is 0.9 in the present study that depends on the crystal morphology and lattice direction. β is the line broadening value at half of the maximum intensity (FWHM), which is expressed as $\Delta 2\theta$ in radians (Monshi, Foroughi and Monshi, 2012).

3.8.4 Fourier transform infrared spectroscopy (FTIR)

Fourier-transform Infrared spectroscopy (FTIR) was applied to investigate the functional groups in the synthesized nanoparticles and PSF-based mixed matrix membranes in the range of 500 cm^{-1} to 4000 cm^{-1} using a spectrophotometer (Model: PerkinElmer Spectrum 100). The nanoparticles (GO, ZnO, ZnO-GO, ZnO-GO-NiO) were prepared by making pellets with potassium bromide (KBr), were exposed to IR-radiations while all the synthesized membranes were subjected to drying for 24 hours at 50°C prior to analysis and then directly exposed to IR-radiations, and both samples were studied for different functional groups.

3.8.5 Atomic force microscopy (AFM)

AFM was performed via a silicon tip that has a radius of 10 nm and a resonance frequency of 70 kHz, as well as a spring with a constant of 2 Nm^{-1} that was worked for the contact less tapping mode in air (Moraille *et al.*, 2022). The AFM instrument was typically used to measure how rough materials or surfaces were (Last *et al.*, 2010).

3.8.6 Atomic absorption spectroscopy (AAS)

AAS identified the metallic concentration in synthesized membranes. Atomic absorption spectroscopy is a procedure which measures the concentrations of metallic elements in various compounds. It uses electromagnetic radiations of different wavelengths, coming from a light source. Different elements will absorb these wavelengths contrarily which helps to differentiate those elements in various materials.

3.8.7 Universal testing machine (UTM)

Mechanical properties of the prepared membranes were examined using universal testing machine. A Universal testing machine (UTM) is used to check the mechanical properties such as tension, compression etc. of a given sample specimen by exerting stress in tensile, compressive, or transverse directions. The machine has been given the name “universal” because it can perform wide range of tests over different kind of materials.

3.8.8 Contact angle measurement:

The hydrophilic properties were analysed by the estimated values of the static contact angle and the membrane surfaces at ambient temperature. While the contact angle was the concluded by placing 2 cm × 1.5 cm sized piece of membrane in goniometer and dropping (2.5- 5 µL) of DI water on the membrane (Toosi, Emami and Hajian, 2018).

Thermo-gravimetric analysis (TGA) was applied to analyse the thermal stability of the mixed matrix membranes by using a thermos-gravimetric analyser (used in COMSATS university Islamabad). 10 mg of the prepared samples was heated from 40°C to 1000 °C at a heating rate of 10 °C/min in N₂ atmosphere (Suhaimi *et al.*, 2019).

3.9 Permeability test of membranes

The permeability of the synthesized membranes was assessed by performing number of batch experiments in a permeation cell consisted of 400 mL stainless still. The membranes were cut into circular pattern and put on the basement support. The effective areas and effective diameters of the PSF/PEG-4000 membranes were $1.4 \times 10^{-3} \text{ m}^2$ and $2.1 \times 10^{-2} \text{ m}$ respectively. Compressed N₂ gas was used to create pressure inside the cell while the permeate was obtained from the base as expressed in **Fig. 3.4 (a)**. The membranes were compressed with deionised water at 2 kg cm⁻² transmembrane pressure for 60 min and pure water fluxes were determined after each 5 minutes until the flows across the membranes got stable. To determine the compaction factors (CF), the ratio between (PWF_{initial}) and (PWF_{steady state}) was determined. Dead End Filtration Unit was used as a filtration assembly that works on the application of the

pressure which provides a push to the feed through the membrane filter (Berk, 2009). A particle-free clear filtrate produces as a result of the process that is called permeate. However, the separated particles/contaminants from the feed make a filter cake. In a typical assembly, particle-containing fluid (liquid, gas) is pumped in opposition to the filter medium (PorexFiltration, 2019). Pressure is kept as low as possible to lessen the compaction of the retained substances (Singh, 2015). The constant outflow of the filtrate causes the accumulation of filter cake from the solid particles to be separated on the filter medium (Singh, 2005). Which can also have a convinced influence on the filtrate condition because the formation of the filter cake can result in an additional depth filter effect, subject to the pore structure of the filter cake and its permeability (Nagy, 2019).

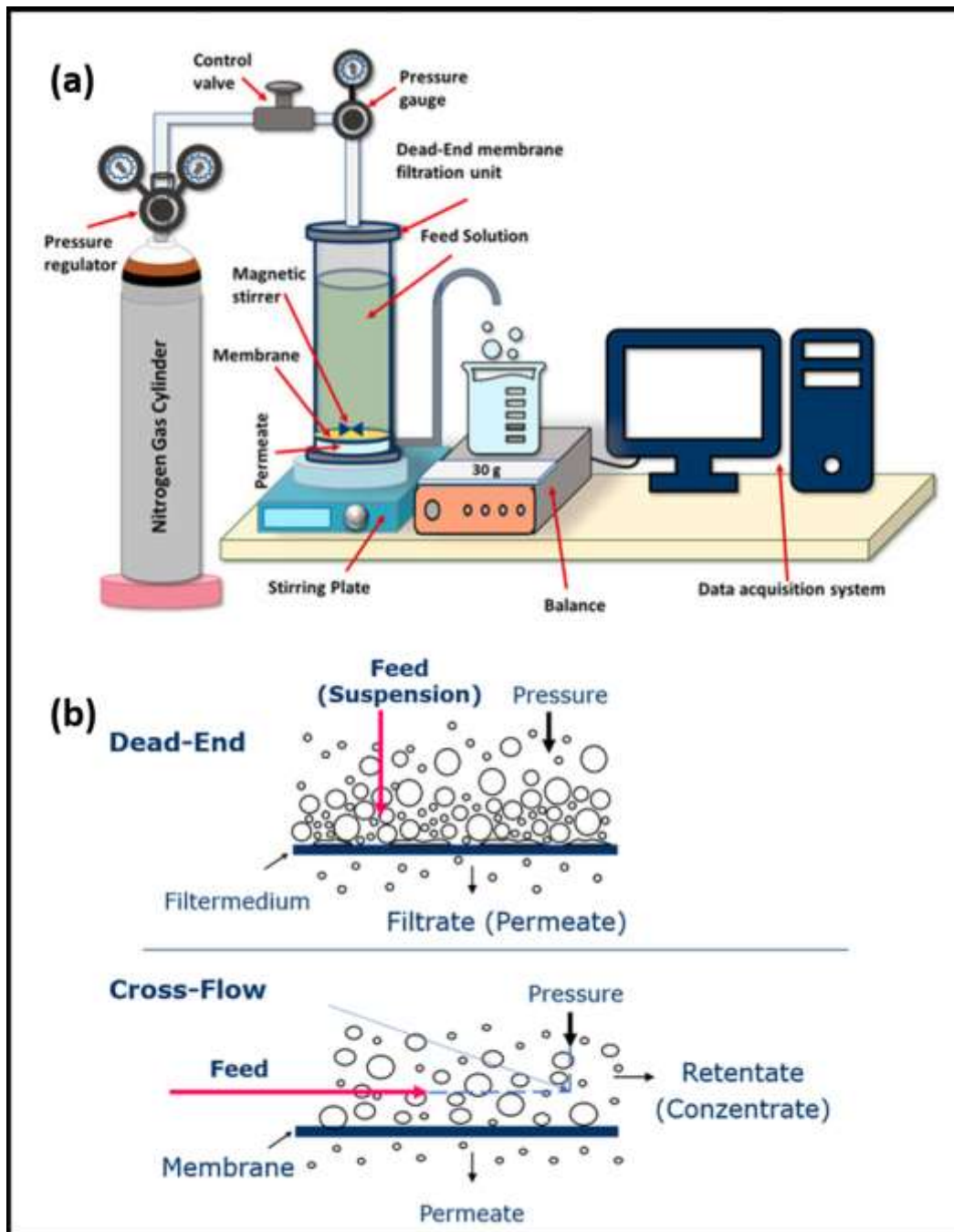


Fig. 3.4 (a) Schematic representation of the bench scale filtration system used in the study (Dead End Filtration Unit) and (b) a comparison mechanism of dead end and cross-flow filtration.

3.10 Pure water flux (PWF) of membranes and Hydraulic permeability (P_m)

Hydraulic permeability (P_m) is important to estimate for the membranes working on pressure difference principle (Khirevich, Yutkin and Patzek, 2022). For this purpose, the pure water permeate flux tests were performed on the compacted membranes at the differential pressures of (2 kg cm⁻², 2.5 kg cm⁻², and 3 kg cm⁻²) till the attainment of an equilibration point. Eq. (3) was used to calculate pure water fluxes (Jacob *et al.*, 2014).

$$J_w = \frac{q}{A\Delta t} \quad (3)$$

where A is the membrane's effective area (m²), Q is the volume of permeate (L), and Δt is the time interval (h). Hydraulic permeability (P_m) was determined by the slope of J_w vs. P graph by the following Eq (4).

$$P_m = \frac{J_w}{\Delta P} \quad (4)$$

3.11 Equilibrium water content (EWC), porosity, compaction factor, mean pore diameter, and hydrophilicity

The equilibrium water content (EWC) specifies the porosity and hydrophilicity of the membranes. Eq. (5) was used to estimate equilibrium water content at room temperature (Liu *et al.*, 2019).

$$EWC(\%) = \frac{W_w - W_d}{W_w} \times 100 \quad (5)$$

Following Eq. (6) was used to find the porosity of the membranes (Chakrabarty, Ghoshal and Purkait, 2008a)

$$\text{Porosity}(\varepsilon) = \frac{\frac{W_w - W_d}{\rho_w}}{\frac{W_w - W_d}{\rho_w} + \frac{W_d}{\rho_w}} \quad (6)$$

Where W_w and W_d are the membranes weights in wet and dry states, respectively. (ρ_w) is water density, and (V) is the membranes volume. The weight of the wet membranes was measured by using digital weight balance. The surface water was dried using an air heater and the wet membranes were vacuum dried at 40 °C for 1 hr and weighed again. SEM images captured at various locations were used to estimate volume and thickness of the synthesized membranes. The mean pore diameters were determined at 2 kg cm⁻² pressure difference through the values of pure water flux. This experimental method was based on Hagen-Poiseuille's equation (Zhang, Nguyen and Ping, 2009a; Zhang, Xiao and Hu, 2013a).

$$\text{Mean pore radius } (r') = \sqrt{\frac{8\mu_w h' J_w}{\varepsilon \Delta P}} \quad (7)$$

Where μ_w is water viscosity, h' is membrane thickness, and ΔP is differential pressure. Guerout-Elford-Ferry equation was also used in calculation of mean pore radius by some other researchers (Ghaemi, Zereshki and Heidari, 2017a).

$$\text{Mean pore radius } (r') = \sqrt{\frac{(2.9 - 1.75\varepsilon)8\mu_w h' J_w}{\varepsilon \Delta P}} \quad (8)$$

Where h', J_w, ε, η, and ΔP stand for membrane thickness (m), pure water flux (m³/s), porosity Eq. (6), viscosity of pure water (0.00089 Pa.s), and transmembrane pressure (TMP, Pa).

3.12 Membrane compaction factor

Membrane compaction phenomenon tests the mechanical strength of the polymeric membrane by applying pressure. The flux having a linear relation with pressure suggest that no membrane compaction arose. The resulted deformation of the membrane compaction is often permanent. The following equation is used ascertain the membrane compaction factor (CF) at a given working pressure (Sinha and Purkait, 2014).

$$CF = \frac{J_{in}}{J_{st}} \quad (9)$$

where J_{in} and J_{st} are the flux of the deionized water at the start of the filtration and after 90 min of the filtration process ($L.m^{-2}.h^{-1}$).

The volume of water which passes through the specific area of the membrane per unit time per transmembrane pressure is known as Permeance, expressed by Eq. (10) and Eq. (11) in term of water flux. (Kamal, Ahzi and Kochkodan, 2020).

$$PM = \frac{Q}{A\Delta t\Delta p} \quad (10)$$

or

$$PM = \frac{J_w}{\Delta p} \quad (11)$$

While the permeability is defined as the volume of water which passes through the depth of membrane per unit time per transmembrane pressure (Li *et al.*, 2020).

$$P = \frac{QI}{A\Delta t\Delta p} \quad (12)$$

or

$$P = PM.I \quad (13)$$

or

$$P = \frac{J_w.I}{\Delta p} \quad (14)$$

where Q is water volume, A is membrane effective surface area, Δp is transmembrane pressure, Δt is sampling time, and I is membrane thickness.

3.13 Mechanical characteristics of membranes

Mechanical properties of prepared membranes were examined using universal testing machine UTM (SHIMADZU AGS-X) by applying stress in tensile direction with the maximum capacity of 50kN and standard used to calculate the mechanical strength of membranes is ASTM D882-02 with 10mm/min elongation rate (Liu *et al.*, 2020).

3.14 Antifouling properties and permeate flux recovery

Due to the fouling issue, the membranes' flow was reduced (Alsawaftah *et al.*, 2021). To estimate the antifouling characteristics of the membranes, the flux was measured with the pure DI water and 50 mgL⁻¹ of Pb²⁺ and Cd²⁺ solutions. After filtration, the membranes were cleaned and rinsed with 0.1 M hydrochloric acid (HCl), and 0.1 M of sodium hydroxide (NaOH) for 90 min and the flux of pure DI water was measured again (Jiang *et al.*, 2014; Sisay *et al.*, 2022). Eqs. (15-18) were used to calculate total flux losses because of total fouling factor (R_t), and flux recovery ratios (FRR) (Jaleh *et al.*, 2020):

$$R_t(\%) = \left(\frac{1-J_{w1}}{J_w} \right) \times 100 \quad (15)$$

$$R_r(\%) = \left(\frac{J_w - J_{w2}}{J_w} \right) \times 100 \quad (16)$$

$$R_{ir}(\%) = R_t - R_r \quad (17)$$

$$FRR = \left(\frac{J_{w2}}{J_w} \right) \times 100 \quad (18)$$

where J_{w1} is the membranes' pure water flux following ultrafiltration (50 mgL⁻¹ Cd²⁺ and Pb²⁺ solutions, and 2 kg cm⁻² transmembrane pressure), J_{w2} is the ultrafiltration-cleansed membrane's pure water flux. (50 mg/L Cd²⁺ and Pb²⁺ solutions) at that same pressure. R_r and R_{ir} are reversible and irreversible fouling ratios, respectively.

3.15 Measurement of surface zeta potential

Surface zeta potentials or surface charge of synthesized MMMs were evaluated by placing small pieces into pure DI water and sonicating for 1.5 hours using surface zeta potential Cell (Beckman Coulter) (Kosmulski, 2021).

3.16 Lead and Cadmium ions removal experiment

100 ppm of the Cd²⁺ and Pb²⁺ solutions were prepared by dissolving 50 mg of Cd(NO₃)₂·4H₂O and 50 mg of Pb(NO₃)₂ in 1lit deionized H₂O in a volumetric flask or beaker. Then, 100 mg and 200 mg of lead and cadmium salts stock solutions were prepared to test the membranes to measure HM ions removal efficiency. Different concentrations of the Cd²⁺ and Pb²⁺ solutions were attained by offsetting the stock solutions. The pH values of Cd²⁺ and Pb²⁺ solution was changed by titrating 0.1M of HCl and 0.1M of NaOH solutions into the Cd²⁺ and Pb²⁺ solutions. Initially, constant permeability was achieved by passing the pure water for 1 hour from the synthesized membranes at 2 kg/cm² pressure. Then 300 mL of the different concentrations

Cd^{2+} and Pb^{2+} solutions were passed through each membrane for the same time interval and pressure and same procedure was repeated for 100 mg/L and 200 mg/L metal ion solutions for each membranes. After 10 min the obtained permeates were examined by dead end filtration unit. Eq. (19) was used to calculate the removal percentage of the Cd^{2+} and Pb^{2+} ions (Mohammad and Atassi, 2021).

$$R (\%) = \left(1 - \frac{C_p}{C_f}\right) \times 100 \quad (20)$$

Where, C_p is heavy metal concentrations in permeate and C_f is heavy metal concentrations in feed. The breakthrough curve was used to estimate the total elimination rate for a given concentration.

$$R_o (\%) = \frac{q_t}{m_t} \times 100 \quad (21)$$

where m_t is the total amount of contaminant, and q_t is the total quantity of ions adsorbed (mg). The Eqs. (22), and (23), respectively, serve as representations for the q_t and m_t .

$$q_t = \frac{Q}{1000} \int_{t=0}^{t=t_t} C_{ad} dt = \frac{Q}{1000} \sum_{t=0}^{t=t_t} (C_f - C_p) dt \quad (22)$$

$$m_t = \frac{C_f Q t_t}{1000} \quad (23)$$

Where, C_{ad} is adsorbed quantity at time t (mg dm^{-3}), t_t (min) is total flow time at exhaustion point. (%E) shows percentage error between the experimental (q_{exp}) and calculated (q_{cal}) values, expressed by Eq. (24).

$$\% E = \frac{q_{exp} - q_{cal}}{q_{exp}} \times 100 \quad (24)$$

Where, q_{exp} is experimental adsorption capacities and q_{cal} is calculated adsorption capacities calculated from experimental and model equations, respectively.

3.17 Adsorption kinetics for cadmium and lead ions removal

The mechanism of ultrafiltration for the removal of Cd^{2+} and Pb^{2+} ions was investigated by kinetic study. In this study, membrane working was managed as a fixed bed where the membranes at the base functioned as fixed bed (porous) and 400 mL column provided the direction to the heavy metal ions solution. As the pressurized air at the top of the column derived the water through the bed. As a result, the second-order kinetics and the linearized Thomas model, which is based on the Langmuir model, were appropriate for the experimental results. It is widely used to investigate the kinetics of adsorption in both packed bed and

membrane separation processes (K. Khulbe and Matsuura, 2018). For this purpose, the following equation was used (Fang *et al.*, 2017).

$$\ln\left(\frac{C_f}{C_p} - 1\right) = \frac{K_T q_0 M'}{Q} - \frac{K_T C_f}{Q} V_t \quad (25)$$

In Eq. (25), M' is the adsorbent's total mass (g), V_t is the volume of fluid passed at time t , q_0 is the adsorbent's total adsorption capacity (mg g^{-1}), and K_T is the Thomas rate constant ($\text{Lmin}^{-1} \text{mg}^{-1}$)

3.18 Stock Solution Preparation

3.18.1 Preparation of Cd^{2+} solution

100 ppm of the Cd^{2+} solution was made by dissolving 274.43mg of $\text{Cd}(\text{NO}_3)_2 \cdot 4\text{H}_2\text{O}$ in 1lit deionized water in a flask. The mass of $\text{Cd}(\text{NO}_3)_2 \cdot 4\text{H}_2\text{O}$ required was calculated with **Equation**

3.1.

$$\text{mass of } \text{Cd}(\text{NO}_3)_2 \cdot 4\text{H}_2\text{O} = V \times \text{MW of } \text{Cd}(\text{NO}_3)_2 \cdot 4\text{H}_2\text{O} \times \text{ppm of } \text{Cd}^{2+} / \text{MW of } \text{Cd}^{2+} \times \text{stoichiometry} \quad (3.1)$$

where,

V = volume of stock solution, Liter

MW of $\text{Cd}(\text{NO}_3)_2 \cdot 4\text{H}_2\text{O}$ = molar mass of $\text{Cd}(\text{NO}_3)_2 \cdot 4\text{H}_2\text{O}$, (g/mol)

MW of Cd^{2+} = molecular mass of Cd^{2+} , (g/mol)

stoichiometry = stoichiometry in $\text{Cd}(\text{NO}_3)_2 \cdot 4\text{H}_2\text{O}$

3.18.2 Different Concentration Cd^{2+} Solutions preparation:

Different concentration of Cd^{2+} (5ppm, 10ppm, 15ppm, 20ppm and 25ppm) solutions were made by dilution of the 100ppm Cd^{2+} stock solution by dilution factor equation presented in Equation 3.2.

$$C_1 V_1 = C_2 V_2 \quad (3.2)$$

As,

C_1 = conc. of Cd^{2+} stock solution, ppm

C_2 = Required conc. of Cd^{2+} stock solution, ppm

V_1 = vol of Cd^{2+} stock solution required for dilution, mL

V_2 = Required vol of Cd^{2+} stock solution, mL

A Cd^{2+} calibration curve was made at different concentrations of Cd^{2+} (0ppm, 5ppm, 10ppm, 15ppm, 20ppm and 25ppm) solutions, analysed by dead end filtration unit.

3.18.3 Preparation of Pb^{2+} solution:

100ppm of the Pb^{2+} solution was prepared by dissolving 160mg of $Pb(NO_3)_2$ in 1lit deionized H_2O in a volumetric flask. The desired $Pb(NO_3)_2$ mass was evaluated by **Equation 3.3**.

$$mass\ of\ Pb(NO_3)_2 = V \times MW\ of\ Pb(NO_3)_2 \times ppm\ of\ Pb^{2+} / MW\ of\ Pb^{2+} \times stoichiometry \quad (3.3)$$

As,

V = vol of the stock solution, L

MW of $Pb(NO_3)_2$ = molecular mass of $Pb(NO_3)_2$, (g/mol)

MW of Pb^{2+} = molecular mass of Pb^{2+} , (g/mol)

stoichiometry = stoichiometry in $Pb(NO_3)_2$

3.18.4 Different Concentration Pb^{2+} Solutions preparation:

Pb^{2+} solution of the following concentrations 5ppm, 10ppm, 15ppm, 20ppm and 25ppm were prepared by dilution of the 100ppm Pb^{2+} stock solution the following equation:

$$C_1V_1=C_2V_2 \quad (3.4)$$

where,

C_1 = concentration of Pb^{2+} stock solution, ppm

C_2 = Required concentration of Pb^{2+} solution, ppm

V_1 = volume of Pb^{2+} stock solution, mL

V_2 = Required volume of Pb^{2+} stock solution, mL

A Pb^{2+} calibration curve was made by different concentrations of Pb^{2+} (0ppm, 5ppm, 10ppm, 15ppm, 20ppm and 25ppm) solutions, analysed by dead end filtration unit.

3.19 Heavy Metal Adsorption Performance Test

7cm² (1cm x 7cm) of each membrane was put into 10mL of Cd^{2+} and Pb^{2+} solutions under different conditions to find the static uptake capacity of Cd^{2+} and Pb^{2+} on ZnO/GO PSF MMMs and ZnO/GO/NiO PSF MMMs. The initial and final concentration of Cd^{2+} and Pb^{2+} were measured by using the dead-end filtration unit.

$$qe = (C_0 - C_e) Vm \quad (3.5)$$

where,

qe = adsorption capacity, mg/cm²

C_0 = initial conc. of metal ions in solution, mg/L

C_e = equilibrium conc. of metal ions in solution, mg/L

V = vol of the solution, Liter

m = area of membrane, cm²

3.20 Evaluation of Conditions of Adsorption

3.20.1 Effect of pH on Adsorption efficiency

The pH values of Cd^{2+} and Pb^{2+} solution was changed by titrating 0.1M of HCl and 0.1M of NaOH solutions into the Cd^{2+} and Pb^{2+} solutions. Test calculations for the preparation of 0.1M HCl and 0.1M NaOH solutions are shown in Appendix D and E. The HCl solution was used to increase the acidic nature of the solution hence decreased the pH values of the Cd^{2+} and Pb^{2+} solutions whereas the NaOH solution increased the basic nature by raising the pH values of Cd^{2+} and Pb^{2+} solutions. 10 mL of each of the solutions with different pH values were then added to a 15 mL centrifuge tube. The pH values of the Cd^{2+} and Pb^{2+} solutions were then changed to 2.3, 3.5, 5.5, 8.3, 10, and 11. Each tube contained five membrane segments with a 1 cm × 7 cm cross section area. The tubes were leaved for 3hr without any disturbance. After 3hr membranes were removed and the solutions were filtered using filter papers before performing dead-end filtration test as the precipitate of Cd^{2+} and Pb^{2+} can cause damages to the instrument.

3.20.2 Effect of Contact Time on Adsorption efficiency

The effect of contact time on the efficiency of the adsorption was analysed by putting four pieces of the membranes of 1cm x 7cm cross section into the 15mL centrifuge tubes having 10mL of 25ppm Cd^{2+} and Pb^{2+} solutions. The membranes were drawn out after 1, 2, 3 and 4 hrs, respectively from the tubes and the tubes were examined using dead-end filtration unit.

3.21 Desorption and Regeneration

A perfect adsorbent should exhibit a good adsorption ability as well as an excellent desorption performance because in this way it will be able to sustain the adsorption efficiency for a long time at reduced operational cost. Thus, desorption and regeneration are very important for any adsorption process by MMMs (Peng *et al.*, 2017). (Mukherjee, Bhunia and De, 2016) stated that graphene oxide membrane with adsorbed HM particles can be restored by using acidic solution. First, the membranes employed in the adsorption of Cd^{2+} and Pb^{2+} in 10 mL Cd^{2+} and Pb^{2+} solutions with 25ppm were cleaned completely for 15 minutes with distilled water. Then, the membranes were placed into HCl (0.1 M) solution that was stirred for 45 minutes with a magnetic stirrer at 500rpm. After that the membranes were removed from the acidic solution and washed with distilled water until a neutral pH obtained. Membranes were then place back into 10 mL Cd^{2+} and Pb^{2+} solutions with 25ppm for the application of adsorption of Cd^{2+} and

Pb²⁺ again. The maximum adsorption capacities were then again identified. To assess the desorption capabilities of the membranes, the identical procedure was carried out three times. For the purpose of measuring the concentration of Cd²⁺ ions in the HCl solution, 10mL of the old HCl (0.1 M) was put into the centrifuge tubes that were then transported to a dead-end filtering unit.

3.22 Bulk Analysis

Adsorption performance of the ZnO/GO and ZnO/GO/NiO in MMMs and bulk was analysed through bulk analysis. 0.13g of ZnO/GO and ZnO/GO/NiO were put directly into a 50mL of Cd²⁺ and Pb²⁺ solutions with the concentration of 100ppm separately. After six hours, the solutions were filtered to ensure that the equilibrium adsorption capacity could be reached. Ten milliliters of the filtered solution were then put into a 15-milliliter centrifuge tube and transferred to the dead-end filtering unit for the determination of the Cd²⁺ ions concentration in the HCl solution.

Chapter 4

Results & Discussion

4. Results and discussions

4.1. Characterization of membranes and NPs

4.1.1. Microscopic analysis (NPs and composite morphology)

SEM is a characterisation tool to analyse the topography, morphology, composition and crystallographic information of materials (Liu *et al.*, 2014). SEM Images of nanoparticles GO, ZnO, and composites ZnO-GO, and ZnO-GO-NiO are presented in **Fig. 4.1** As could be seen from **Fig. 4.1 (a)** GO nanosheet was appeared as a thin and flexible film with obvious wrinkles (Fouda, Duraia and El-Tantawy, 2016). Scrolling and crumpling morphology might be viewed as intrinsic feature of Graphene oxide (GO) (Fouda, Duraia and El-Tantawy, 2016). A large graphene oxide sheet (4-5 layers) with dimension of nanometres (approximately 10-15 nm) has been found to be situated on the top of the grid, with 97.05 % purity.

The white dots in the SEM image were added by the ZnO NP decorating of the GO nanosheet in **Fig. 4.1 (c)**. The investigation of particle size and surface morphology of (GO-ZnO) composite shows that the particles of nano ZnO have been dispersed on GO sheets (He *et al.*, 2018). It is observed that some ZnO particles have been agglomerated. The particles diameter of nano ZnO is less than 25 nm and three particles diameter is determined as 15.7, 18.98 and 20.32 nm, it was further confirmed by EDX analysis. (Hosseini and Babaei, 2017a). While the microscopic spots scattered around the graphene oxide flake are attributable to the zinc oxide (ZnO) nanoparticles, the wrinkles and folded portions are attributed to graphene oxide (GO) (Hosseini and Babaei, 2017b). Hence, the nanosheet of GO and nanoparticles of ZnO in the composite are approved by both micrographs (Hosseini and Babaei, 2017b).

As can be seen, **Fig. 4.1 (d)** shows fairly agglomerated, spherical NiO nanoparticles along with ZnO-GO nanocomposite. The SEM image exhibited that nano-NiO with the presence of (ZnO-GO) was a typical nano-sheet morphology with the thickness of about (10–12) nm (R. Kumar *et al.*, 2018). The disordered nanoparticle structure of NiO persisted even as the calcination temperature was raised to 300 °C, as seen in Fig. 4. (d) that some nanoparticles began to agglomerate. The lattice spacing was 0.31 and 0.34 nm indicating that the sample converted to NiO under the calcination at 300 °C (Chen *et al.*, 2022). When the calcination temperature was

further increased to 400 °C, NiO gathered and partially converted into nanoparticles, while at 500 °C calcination temperature, NiO was basically NiO nanoparticles. The samples NiO along with ZnO-GO nanocomposite, at 400 °C and 500 °C calcination temperature, comprised of nanoparticles and nanosheets had a higher propensity to aggregate before turning into NPs entirely. These findings demonstrate that the nanosheet morphology of NiO nanosheets tended to be maintained during calcination in a carbon and zinc environment (Chen *et al.*, 2022).

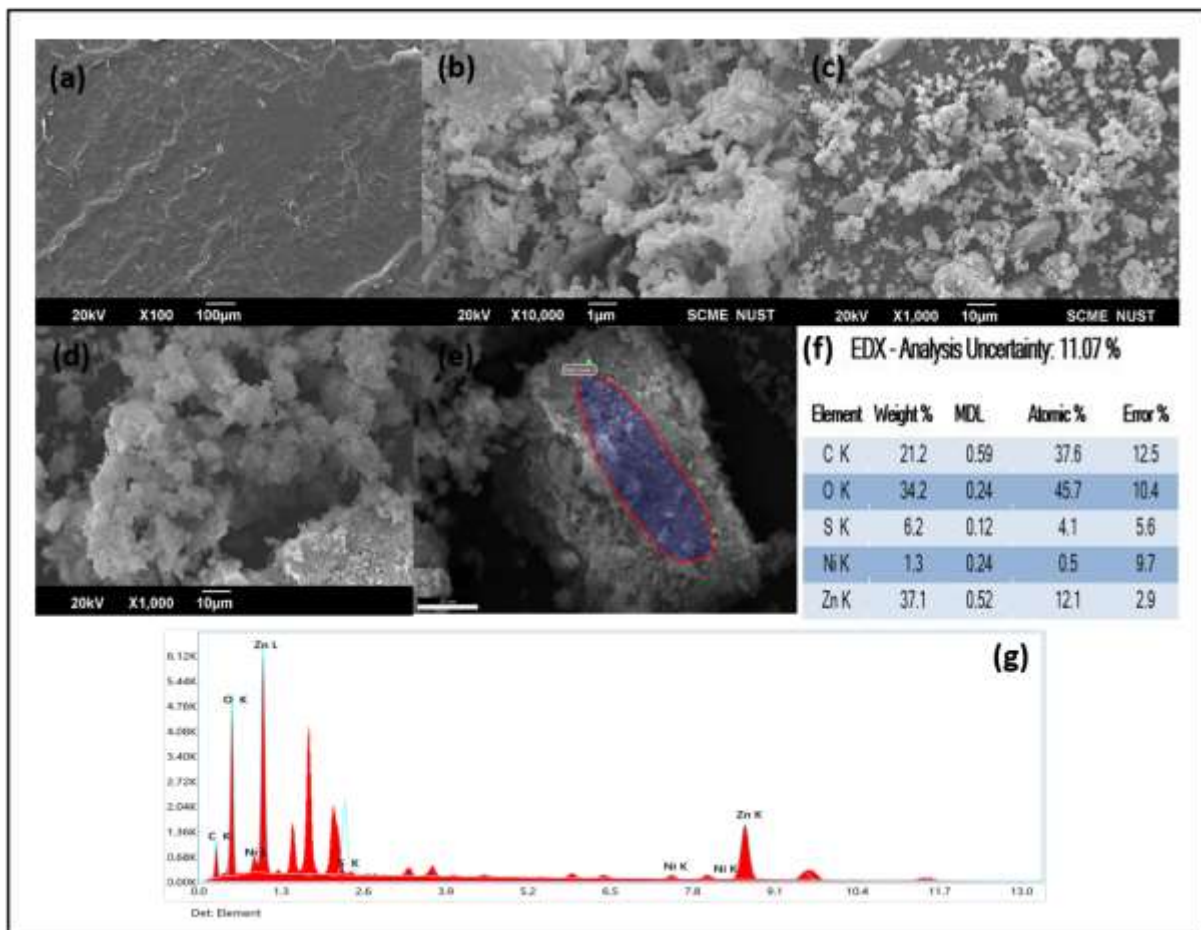


Fig. 4.1 SEM Images of nanoparticles (a) GO, (b) ZnO, and composites (c) ZnO-GO, and (d) ZnO-GO-NiO, while (e, f, g) shows EDX elemental microanalysis of final nanocomposites ZnO-GO-NiO.

Fig. 4.1 (e, f, g) represents the EDX elemental microanalysis of final composite (ZnO-GO-NiO). The elemental analysis is provided by EDX using a semi-quantitative process, and it is discovered along with the peak area and spectra for each component of the sample (Scimeca *et al.*, 2018). The spectra of the naturally synthesised GO-decorated ZnO-NPs and its incorporation with NiO demonstrated the presence of the required phase of C, O, Zn, and Ni proving great purity of nanocomposite (ZnO-GO-NiO) NPs. In our data, the measured stoichiometric mass percentages of Zn, O, C and Ni were 37.1 wt.%, 34.2 wt.%, 21.2 wt.%, and 1.3 wt.% respectively.

4.1.1.1. Membranes morphology

The morphology (quantitative) of composite membranes of different wt. % of polymers and nanoparticles were examined by scanning electron microscope (SEM) having high-resolution, as can be seen in **Fig. 4.2** It shows the surface and cross-sectional SEM micrographs of neat PSF membrane (**M1**), and 0.2 wt. % GO PSF MMM (**M2**). While Fig. 4.2 (e) (f) and (g) (h) show the surface and cross-sectional SEM illustrations of (0.1) (0.3) wt. % ZnO-GO PSF MMMs (**M3**) (**M4**) respectively. Fig. 4.2 (i) (j) and (k) (l) show the surface and cross-sectional SEM illustrations of (0.1) (0.3) wt. % ZnO-GO-NiO PSF MMMs, (**M3_A**) (**M4_A**), respectively.

As could be seen from Fig., GO nanoparticles emerged as a thin film in M2. It shows a layered structure with a fairly smooth surface (Pourbeyram, 2016). (M3) and (M4) represents agglomerated particles of ZnO of membranes surface which were probably made by the escape of volatile matters or gases during the calcination process (Bekele *et al.*, 2021). The impregnation of zinc oxide nanoparticles on to GO nanosheet put white spots in SEM image of respective membranes surface and it was further confirmed by EDX analysis. ZnO nanoparticles display quasi-spherical agglomerated particles onto GO on membranes surface (M3) (M4) (Alamdari *et al.*, 2019). Comparatively clustered spherical NiO nanoparticles can be noted in membranes (M3_A) and (M4_A). ZnO/NiO agglomerates of heterostructure shape are homogeneously dispersed on the surface of graphene oxide (Mardiroosi, Mahjoub and Fakhri, 2017).

The cross-sectional view revealed an asymmetric structure of the membranes that was evenly dispersed. These membranes were seen to be composed of a very thin dense upper layer with nearly concealed pores with the supportive permeable layer covering the cross-section area of the membranes. The membranes contained cellular and needle-like porous structure which was quite unique from the typical structure of the PSF membranes. It was observed that the phase separation methods were adopted during the time of casting brought a change in non-Newtonian solutions viscosity which resulted in the appearance of similar pores in all membranes having different compositions. A similar porous structure was seen by (Lee *et al.*, 2013), as (M1) membrane containing 15 wt.% PSF and 5 wt.% PEG-4000. The polysulfone/polyethylene glycol membrane (M1) was found similar to a hydrolysed membrane prepared by (Zhang *et al.*, 2014) which contained PSF:PEG:PAN:DMAc = 16:8:4:72 (DMAc is N, N-dimethylacetamide) ratio. Another similar membrane was observed by (Simin Nasseri, 2017) comprising of GO in this case of (M2). The large and the small pores were formed by phase separations (liquid-liquid) and (solid-liquid) (Roh *et al.*, 2012).

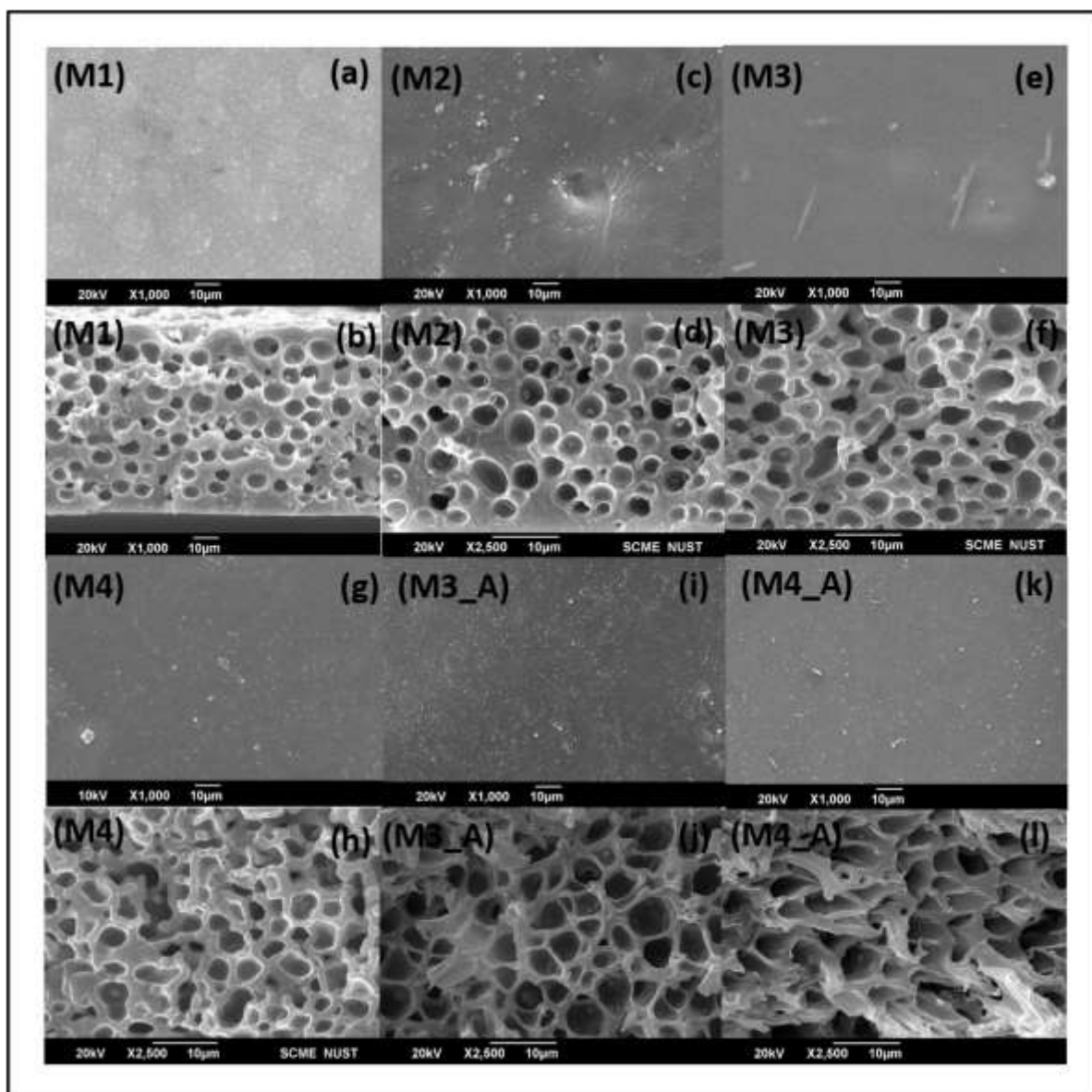


Fig 4.2 SEM Images of synthesized membranes surface and cross-section as mentioned on each membrane

On the other hand, a thicker, porous layer and dense skin layer was observed for the neat PSF membrane. The delay in the de-mixing rate on between the solvent and solute was the probable reason for this appearance (Barth *et al.*, 2000). This delay caused a decrease in the rate of phase inversion procedure in comparison to the process of fabrication of membranes (Chung *et al.*, 2017). The hydrophilicity of ZnO impregnated GO nanocomposite membranes (M3) and (M4) induces propensity in the membranes to draw more water during the phase inversion. As a result, the de-mixing rate increases which creates a porous structure (Rabiee *et al.*, 2015). These membranes reveal the distribution of the Zn on the synthesized membranes that was not observed on the surface of neat PSF membrane (M1) or on surface of membrane (M2)

containing 0.2 wt.% GO. The zinc element displayed a homogeneous dispersion on PSF/ZnO-GO MMMs while the agglomeration might be happened for ZnO nanoparticles (Rosn, Teow and Mohammad, 2018). While the more porous structure of (ZnO-GO-NiO) composite membranes depicts a slow exchange rate between solvent and solute during phase inversion (Chong *et al.*, 2017). Due to this phenomenon, final nanocomposite membranes (M3_A) and (M4_A) shows a considerable difference between the neat PSF and GO membrane (M1) and (M2) respectively, and (0.1) (0.3) wt. % ZnO-GO membranes (M3) and (M4). The larger pore size for (ZnO-GO-NiO) PSF MMM as compared to other membranes is also due to attraction of the non-solvent by the oxygen functional groups of the (ZnO-GO-NiO) towards the polymer solution. As a result, non-solvent inflow and outflow of the solvent was increased. The acceleration of the phase inversion process was caused due to little contact of the metal ions and functional groups of the surface as a result of pore size increase. (Chong *et al.*, 2017).

The large and the small pores were formed by liquid-liquid and liquid-solid phase separation respectively (Roh *et al.*, 2012). After PEG-4000 is discharged from the polysulfone matrix during the liquid-liquid phase separation, tiny holes start to form. The synthesized membranes are less porous and have small pore size at upper and lower surface. That is why these cooled more rapidly instead of inner sections (Chong *et al.*, 2017). The two most essential components which can influence the functionality of the membranes are porosity and hydrophilicity (Zhang *et al.*, 2013); (Mir *et al.*, 2016). The porosity of composite membranes was calculated by using Eq. (6) (Chakrabarty, Ghoshal and Purkait, 2008b). The casting solutions viscosity and cooling rates also effects on the membranes thickness (M1 = 91 μm , M2 = 98 μm , M3 = 108 μm , M4 = 119 μm , M3_A = 125 μm , and M4_A = 154 μm , having average of 116 μm), which can be seen in the SEM micrographs. The Eq. (7) (Zhang, Nguyen and Ping, 2009b), and Eq. (8) (Ghaemi, Zereshki and Heidari, 2017b) were used to calculate membranes mean pore radius.

4.1.2. Contact Angle

Contact angles diagrams are presented in **Fig. 4.3** The incorporation of additive (PEG-4000) in mixed matrix membranes improves the hydrophilic character, PWF, and pore creation. which increases by the rise in either molecular mass or amount of (PEG-4000) (Ma *et al.*, 2011). In this research, a specific volume of 5 wt.% (PEG-4000) was put in to examine the cavities in each membrane. The hydrophilic nature and the permeability of the water can also be improved by the combination of PEG-4000 and ZnO-NiO mixed matrix membranes. (Zhang, Xiao and Hu, 2013b). Pap (Angesti and Munasir, 2021) classifies the nature of membrane surfaces as

hydrophilic and hydrophobic on the basis of contact angle ranges. Which describes the surface as hydrophilic (partial wetting) when the contact angle range is $0^\circ < \theta < 90^\circ$ while the surface as hydrophobic (non-wetting) when the contact angle range is $90^\circ < \theta < 180^\circ$ (Angesti and Munasir, 2021). At low contact angle the membrane surface is hydrophilic which increases the flux and the ion removal ability of the membrane (Kulkarni, Mukherjee and Gill, 1996). The addition of polyethylene glycol (PEG-4000) causes this increase in hydrophilic nature of the membrane (Sinha and Purkait, 2013).

Graphene oxide (GO) nanoparticles consist of carbon atoms create a small tendency of hydrophobic properties when combined with PSF polymer (Rhazouani *et al.*, 2021). Thus, the effect of synthesized GO nanoparticles towards this property in both types of membrane (PSF and GO + PSF and composite membranes ZnO-GO/ZnO-GO-NiO) was measured using contact angle measurement (Adilah Rosnan, Haan and Mohammad, 2018). **Fig. 4.3** show the contact angle of neat PSF and PSF/GO membranes (M1) and (M2) respectively, gives the highest of water contact angle values of 99.7° and 94.8° . But due to the presence of 5 wt.% PEG-4000 polymer in all the membranes compositions, the hydrophobicity is not as high as it could be in simple PSF/GO based membranes.

When ZnO nanoparticles incorporated to the PSF membranes, it reduces the contact angle that is why the hydrophilicity, permeate flux, and metal ions elimination capacity of the membranes improves (Ayyaru, Dinh and Ahn, 2020) (Fu, Hua and Zhang, 2017). Whereas, exceeding the specific limit of their concentration results in development of poly-acrylonitrile chains on membrane's surface which raises the contact angle and therefore hydrophobicity (Zhu *et al.*, 2007) ; (Mehmet Emin Pasaoglu; Serkan Guclu; Ismail Koyuncu, 2016). The contact angle of ZnO nanoparticle membranes is increase a little due to its incorporation with GO nanoparticles as contact angles of (M3) and (M4) membranes are 90.6° and 92.1° , respectively.

The water contact angle experiment was performed to study the hydrophilicity and wettability of mixed or composite PSF membranes with the addition of various nickel oxide (NiO) concentrations in addition to (ZnO) and (GO) and investigated its hydrophilic effects as well (Bagheripour *et al.*, 2016). The results showed that growing the nanoparticle contents in the casting solution from 0 to 0.1 wt.% caused the water contact angle to fall in the range of 70 to 55° and then further increase from 55 to 60° by adding 0.3 wt.% nanoparticles loading. Consequently, it can be said that increasing the amount of nickel oxide nanoparticles in the casting solution—between 0 and 0.1 weight percent—improved membrane hydrophilicity.

(Bagheripour *et al.*, 2016). This might be affected by an increase in pore volume and size as well as the hydrophilic property of nickel oxide nanoparticles (Jabbar *et al.*, 2020). During the phase inversion process, nickel oxide nanoparticles, like other metal nanoparticles, have a tendency to migrate to the membrane surface. (Chen *et al.*, 2019). When NPs migrate to the membrane's top at a high nanoparticle loading ratio (0.3 wt.%), this causes greater alterations to the membrane's surface pores (pore blockage), which lowers the amount of water that can bind to the membrane's surface. (Jabbar *et al.*, 2020). This may be the main reason for a small increment of contact angle from M3_A to M4_A that is 78.4 °C to 80.7 °C where 0.3 wt.% of ZnO-GO-NiO nanocomposite and 5 wt.% PEG-4000 was used. So, it's proved that M4_A membrane is more hydrophilic as compared to neat PSF and other composite membranes. This result revealed that PSF/GO based membrane is less hydrophilic as compared to membranes containing ZnO or NiO nanoparticles (Pramila and Gopalakrishnan, 2018a). The mechanism shows that due to the usage of the composite membranes, metal ions take the position of the hydrophilic functional groups which increases the contact angle and finally the membrane develops hydrophobic character (Agrawal *et al.*, 2017).

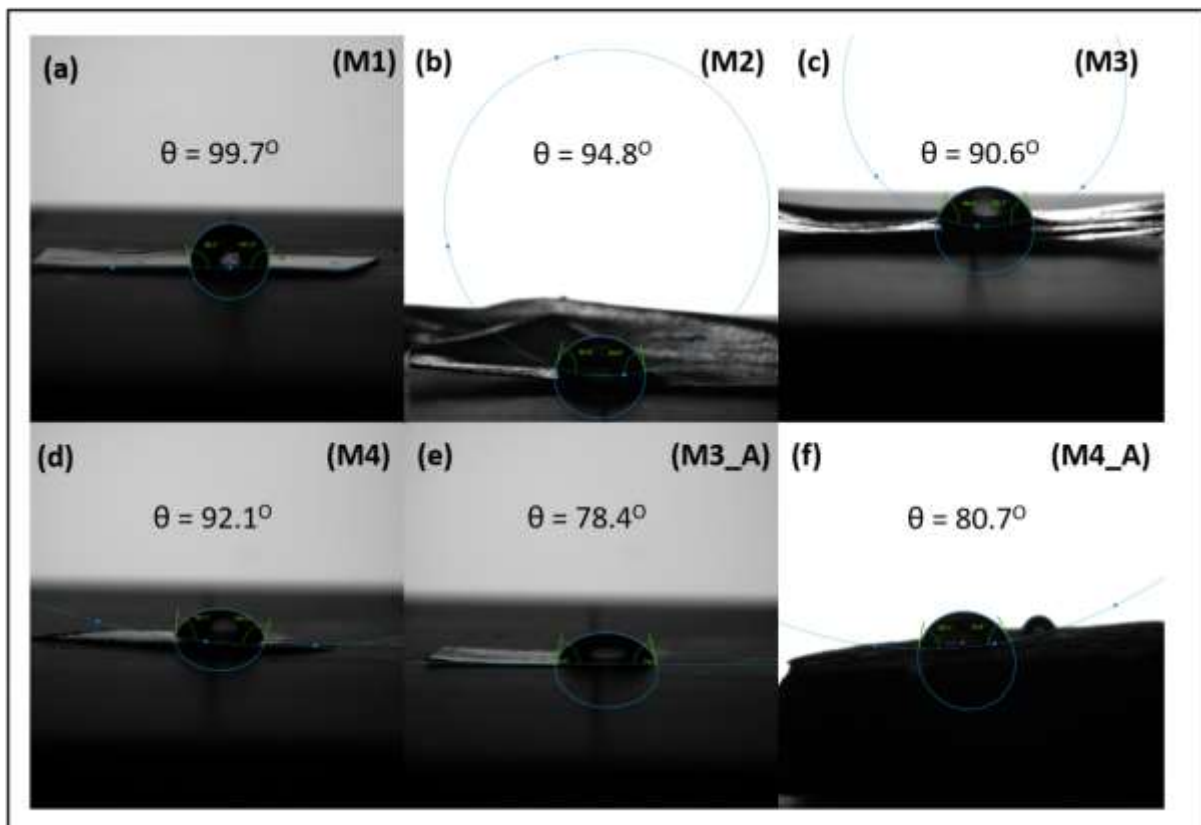


Fig 4.3 Contact angle of synthesized composite membranes from (M1) to (M4_A)

4.1.3. Surface zeta potential

The surface charges of the prepared and utilized composite membranes is represented graphically in **Fig. 4.4 (a)**. The pristine PSF membranes have negative surface zeta potential values which tends to be even more negative with the addition of PEG-4000 or by increasing the concentrations of PEG-4000 in the polysulfone membranes (Fu, Hua and Zhang, 2017). Pure PSF membranes' point of zero charge values are near to pH 3.0 (der Meeren *et al.*, 2004). The PSF membrane's surface holds the negative charge at above pH 3.0 value (M1 = -24.8 mV). The GO membrane's surface also holds the negative charge at the pH ranges of 2.50–8.50 (Xu *et al.*, 2017). Thus, a combination of PSF/PEG-4000/GO increases the negativity of the mixed matrix membrane's surface. And this negativity of the surface further rises by increasing the concentration of PEG-4000/GO in the casting solutions. (Simin Nasseri, 2017) states that the surface charge of PSF/PEG membranes changes approximately from -30.5 to -33.4 mV (M2) and from -33.4 to -28.6 mV by the addition of 0.2% and 0.5 wt.% GO respectively, while the addition of PEG-4000 further increase the charge value to more negative. (Van Der Meeren *et al.*, 2004).

The additives used in the casting solution decreases its mixing compatibility with the non-solvent and improves instant remixing, hence developing thermodynamic properties (Xie, Saito and Hickner, 2011). Yet, because very viscous casting solutions enhance non-solvent inflow and solvent outflow, which leads to the evolution of a porous membrane structure, they also produce kinetic resistance (Young and Chen, 1995). Thus, the increment in the molecular mass of the additive raises the porosity of the membrane. However, large additive molecules can clog the pores of the membrane which can enhance the hydrophilic character of the synthesized membranes and zeta potential increases. For example, ZnO-GO nanocomposite membranes with estimated ZnO loading (0.3-0.5 wt.%) were having zeta potential value of -41.60 mV, -44.30 mV, -45.70 mV for (M3) (M4) and (M5) membranes respectively, suggesting ZnO-GO nanocomposite material was approaching stability at higher ZnO loading to produce uniform NPs distribution which expected a uniform nanomaterials distribution when incorporation with variety of other applications for enhancing the process efficiency (Haan, Rosnan and Mohammad, 2018).

The measurement of NiO zeta potential at various pH levels reveals that NiO is negatively charged (El-Kemary, Nagy and El-Mehasseb, 2013). The Ni²⁺ on the top layer of composite membrane (ZnO-GO-NiO) surfaces completes their coordination sphere by OH groups from

water molecules generating surface OH, and certain layers of adsorbed water are present controlling the contacts on the surface of NiO (Hosny *et al.*, 2020a). As a result, (Ni-OH) sites will be present on the oxide's surface. Because they are not physically and chemically similar, the surface hydroxyl groups generate surface-O through an association-dissociation mechanism. At pH (3), the positively charged Pb and Cd ions will be protonated and available for adsorption by the negatively charged NiO oxide (Hosny *et al.*, 2020a). NiO when combined with negatively charges ZnO-GO nanocomposite to make composite membrane, it exhibit more negative charge on surface. (M3_A) (M4_A) and (M5_A) membranes are more hydrophilic rather than (M3) (M4) and (M5) has more negative surface charge i.e. -53.1 mV, -54.9 mV, -56.2 mV respectively, which may possibly be the reason of high heavy metal ions adsorption on the membrane surfaces, as indicated by (Gu *et al.*, 2019).

The surface charge also increases by the hydroxyl groups of the PEG which can improve the water permeation by creating a hydrogen bond between water and the membrane (Shahkaramipour *et al.*, 2017). The existence of more negative surface charge enhances the removal percentage of heavy metal ions with positive charge (Qasem, Mohammed and Lawal, 2021). Thus, the zeta potentials of the membrane surfaces immensely influence the membrane flux and removal efficiency (Bauman *et al.*, 2013). Once the metal ions solutions were filtered, surface zeta potential values moved in the direction of zero. And this shift become even more when the concentrations of the metal ions in the solution increased (Ernst *et al.*, 2000).

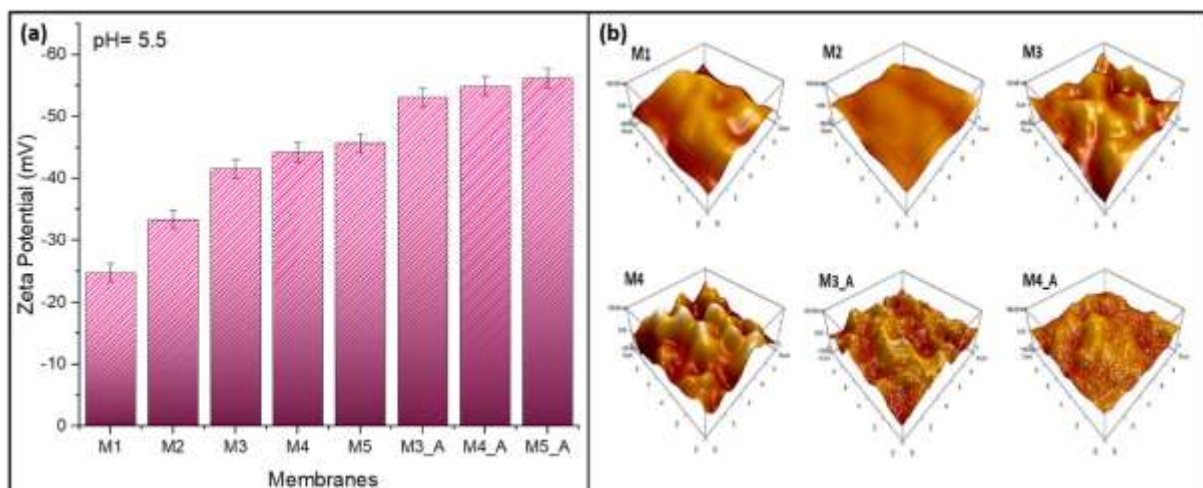


Fig 4.4 (a) Surface charges of the membranes, (b) Atomic force microscopy (AFM) images of membranes

4.1.4 Atomic force microscopy (AFM)

Atomic force microscopy (AFM) analysis was performed to study the surface roughness and surface topography of both neat PSF/PEG-4000, GO, ZnO-GO, and ZnO-GO-NiO PSF MMMs as represented by **Fig. 4.4 (b)**. It is clear that the PSF surface is smooth overall, with the exception of a few minor bumps that may be caused by the structure of the beaded fibres. Pristine PSF membrane (M1) is discovered to have a roughness value (R_A) of roughly 18.50 nm (Plisko *et al.*, 2020). Yet, the PSF level of surface roughness quickly increases with the addition of GO, ZnO, NiO nanoparticle. Up to a certain point, the GO nanoparticle concentration enhances the surface roughness of the PSF/GO (M2) membrane; after that point, R_A values significantly decrease to 14.45 nm (Mao *et al.*, 2020). For membranes (M3, M4) and (M3_A, M4_A), the R_A values of the preparation coatings are determined to be equal to 24.53, 28.76, 36.90 nm, and 39.45 respectively (Hooda *et al.*, 2017).

This finding shows that the surface roughness of the membrane will increase with increasing ZnO/NiO nanoparticle concentration (Ryu *et al.*, 2017). In general, AFM measurements highlight the influence of the PSF to ZnO/NiO nanoparticle content ratio on the degree of roughness of the produced composite membranes (Ryu *et al.*, 2017). It is important to note that the surface roughness of the membranes is better by the produced microbeads and nanofiber structures (Mukai *et al.*, 2021). However, since there are a number of variables that can affect how hydrophobic membranes, a high rough surface does not always exhibit the optimum water contact angle and hydrophobic qualities (Zhang *et al.*, 2015).

4.1.5 XRD analysis

The **XRD** pattern of GO, ZnO nanoparticles, ZnO-GO, and ZnO-GO-NiO nanocomposite material are presented in **Fig. 4.5 (a)**. Pure graphite represented a sharp peak at 26.5° which was moved to 10.8° for graphene oxide, indicated the success exfoliation of graphite into GO nanosheet (Aslam *et al.*, 2019). Sharp peak at 2θ is 10.8° corresponds to the oxygen functionalities of the graphene oxide and signifies the distance in between the graphene layers. This peak is attributed to the (002) reflection plane with the d-spacing of 8.263 \AA while the peak at 31.7° corresponds to the spacing around 2.3 \AA (Anjum *et al.*, 2021). The number of graphene layers in graphene oxide are calculated by the following equation (Elsie *et al.*, 2019)

$$N = \frac{t}{d} \quad (26)$$

where ‘t’ is called crystallite size, and d is lattice spacing. The four number of Graphene Oxide layers were calculated. The peak at 31.7° & 44° shows the short-range order in the assembled layers of Graphene.

XRD spectrum of ZnO nanoparticles displays strong peaks near 31.95°, 34.59° and 36.43° corresponding to the (110), (002), (101) plane respectively. On the other hand, some minute peaks appearing at 47.66°, 56.73°, 63.18°, 68.25° and 69.53° are representative of (102), (110), (103), (112) and (201) crystalline planes respectively (Tariq *et al.*, 2021). Scherrer equation used at (101) line width the average size of zinc oxide nanoparticles comes around 18.98 nm (Vinila and Isac, 2022). It is testified that the reduction or the disappearance of the diffraction peak of graphene oxide nanosheet can occur by the destruction of the nanosheet due to exfoliation (Arthi G and BD, 2015).

The ZnO identical characteristic diffraction peaks are also appearing in the XRD pattern of ZnO-GO nanocomposite but having almost (15.47) nm average particle size (Anjum *et al.*, 2021). After the treatment of the graphene oxide, presence of new peaks and the shift of existed peaks demonstrates the conversion of crystallographic manner of graphene oxide (Hosseini and Babaei, 2016). The major peak of graphene oxide nanosheet at 10.8° vanished by the impregnation of zinc oxide nanoparticles onto graphene oxide nanosheet (Rosn, Teow and Mohammad, 2018). The new peaks of ZnO-GO comes out at 44.07° and 63.18° corresponding to (111) and (220) reflections respectively.

Moreover, the ZnO-GO-NiO materials obtained display bigger diffraction peaks, suggesting the growth of NiO crystals with small particle sizes. GO also takes the form of a composite with ZnO, and the NiO phase predominates in its layers. Nickel oxide peaks occurred at $2\theta = 29.45^\circ$ and 43.53° corresponding to (110) and (200) reflections respectively. Nonetheless, zinc oxide was the most intense and had the most peaks, dominating. The crystallite size of ZnO-GO-NiO composite was found to be 42 nm. Using the Debye Scherer formula Eq. (27), the crystallite size was calculated from the primary diffraction peak.

$$D = \frac{K\lambda}{\beta \cos \theta} \quad (27)$$

Where D is the crystallite size and K is the shape factor that depends on the shape as well as the index (hkl) of the crystals, λ is the wavelength of the X-ray (Cu Ka, 1.54056) and $\beta \cos \theta$ is the diffraction angle of the peak (Hosny *et al.*, 2020b).

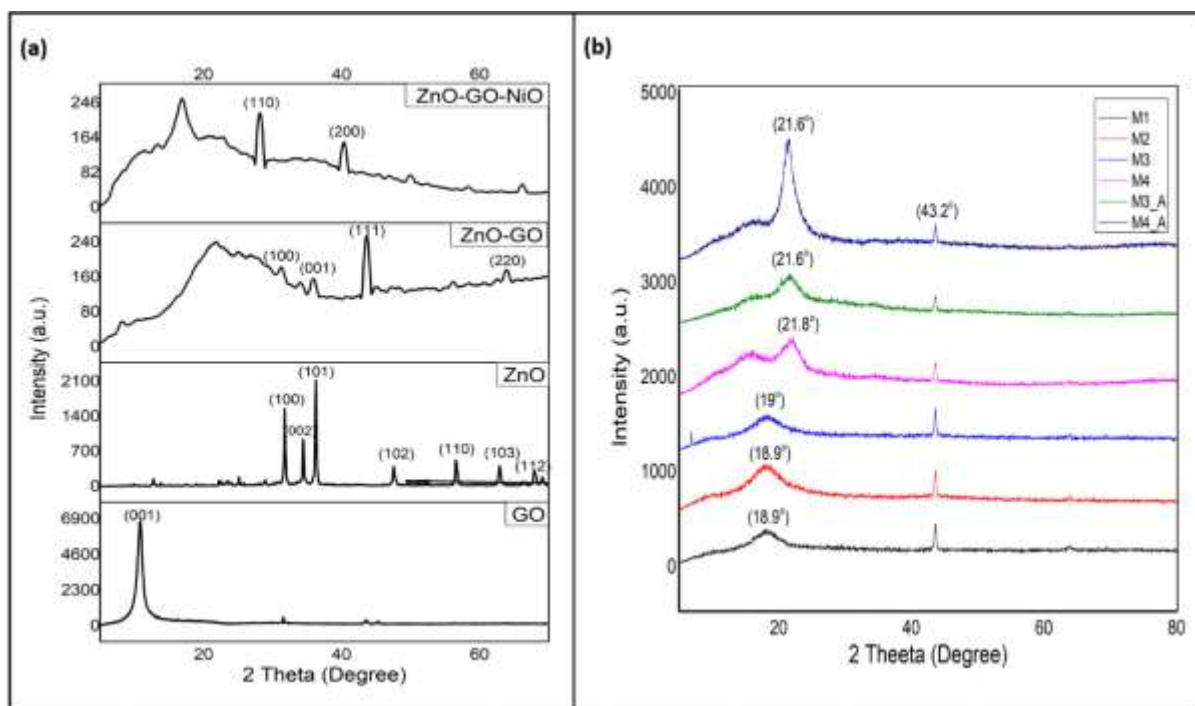


Fig 4.5. XRD spectra (a) of nanoparticles GO, ZnO, and nanocomposites ZnO-GO, and ZnO-GO-NiO and (b) composite membranes.

The results of composite membranes received from the X-ray diffraction analysis are represented in **Fig. 4.5 (b)**. The amorphous structure of polysulfone is implied by the existence of a single broad peak in all experimental samples within the 2θ range of 18.9° – 21.6° . As a result, the other components are ignored (M. Khayet and García-Payo, 2009) and the 2θ values are presented in the ranges of 0 to 90 degrees in Fig. 2(a). The neat PSF and 0.2 wt.% GO membranes' reported 2θ values are 19.9° , and 20.2° respectively. When the compositional components were added to the PSF/PEG-4000 composite matrix, the peak expanded, indicating a rise in polymer chain disorder and the composite materials' increasing amorphousness. (Ionita *et al.*, 2016). The good dispersion or compatibility of the other compositions inside the PSF is linked to the absence of the distinctive diffraction peaks of the other composite materials (GO, PEG-4000, ZnO-NPs) (Wu *et al.*, 2018). While the less peaks in the compositional components could be due to the reduced quantity compared to the PSF. When additional materials are added to the PSF/PEG-4000 composite matrix, it is clear from close observation that the 2θ value lowers significantly ($2\theta = 19.9^\circ$, M1), which denotes a greater structural order of the composite membranes (Ionita, E. Vasile, *et al.*, 2015). When the crystalline size (D) varies from 10.3 (M1) to 12.3 (M3, M4), the d -space value rises from 4.93 (M1) to 5.09 (M3, M4). The ZnO-GO-NiO nanocomposite (M3_A) and (M4_A) showed considerably large diffraction peaks which specifies the formation of NiO crystals of small size. The diffraction peaks attributed to

graphene oxide or zinc oxide completely disappears suggesting the permanent effect of exfoliation on to the stacks of graphene oxide (Yousaf *et al.*, 2021). The sharp peaks of (ZnO-GO-NiO) at ($2\theta = 21.6^\circ$, M3_A, M4_A) indicate its crystalline nature. The layers of the GO in the nanocomposite are overshadowed by the NiO particles (Blessy Pricilla *et al.*, 2021a). The variations in intensity were a sign of the composite materials' varying crystallinity. As crystallinity rises, the intensity rises as well (Yang, Chiu and Lin, 2008).

4.1.6 Spectroscopic analysis

The **FT-IR** spectroscopy identifies the chemical structure of nanoparticles used in this study. **Fig. 4.6 (a)** displays the FT-IR spectra of GO, ZnO and ZnO-GO, ZnO-GO-NiO composite. The absorption band at 3441 cm^{-1} represents the stretching vibration of OH-groups in graphene oxide indicating the existence of hydroxyl groups in the GO layers (Nayak *et al.*, 2016b). While 1544 cm^{-1} and 1646 cm^{-1} peaks of the C=O stretching vibrations (Vignesh Nayak, 2017b) represents carboxylic acids, ketones, aldehydes, or esters occurrence (Xiaolu Liu, 2019). In the intermediate region, the peak at 1067 cm^{-1} and smaller peaks between 1230 cm^{-1} and 1375 cm^{-1} corresponds to C-H, and C-O stretching vibrations respectively (Hadjiivanov *et al.*, 2021). The metallic oxides nanoparticles i.e ZnO, the absorption peaks appear at 454 cm^{-1} , 912 cm^{-1} below 1000 cm^{-1} in the fingerprint area of the infrared spectrum (Daniela C Marcano 1, 2010). The absorption peaks appeared at 1000 cm^{-1} to 1700 in nano ZnO is due to C-O, C-H, C=O stretching vibrations respectively (Sheela, 2012). As hydrogen shows a tendency to form hydrogen bonds with metal oxides, a possible absorption band appears at 3444 cm^{-1} corresponding to of O-H stretching vibration (Gusatti *et al.*, 2011b). Due to reduced thickness, it can be inferred that these groups are the reason for ZnO nanoparticles interaction (Sheela, 2012). The peaks in the range of 1000 cm^{-1} and 1700 cm^{-1} corresponds the oxygen containing bonds. Which are accountable for the attractive forces between nanoparticles and metal ions (Bernstein, Kaufman and Freger, 2013a)

The distinctive band of the stretching vibration of the O-H groups may be seen at 3496 cm^{-1} by comparing the prior spectra with the FT-IR spectrum for GO/ZnO (Rodríguez *et al.*, 2020). It can be determined that these groups are in charge of the interaction with the ZnO nanoparticles because of the decrease in thickness (Rodríguez *et al.*, 2020). It can be determined that these groups are responsible of the interaction with the ZnO nanoparticles because of the decrease in thickness (Hadadian *et al.*, 2018). The remarkable peak at 566 cm^{-1} represents the NiO vibration confirms the existence of NiO nanoparticles. In comparison to the IR spectra of GO, ZnO, and

ZnO-GO nanoparticles, the OH stretching vibrations of GO reduced and a small move of NiO vibrations was examined at 3439 cm^{-1} (Khalaji and Das, 2014). Which was due to the possible coordination of the OH with the NiO nanoparticles, changing the dipole moment during a vibration (Blessy Pricilla *et al.*, 2021b). Again, the absorption peaks appeared at 1023 cm^{-1} to 1647 cm^{-1} in nano (ZnO-GO-NiO) composite is due to C-O, C-H, C=O stretching vibrations respectively (Sheela, 2012).

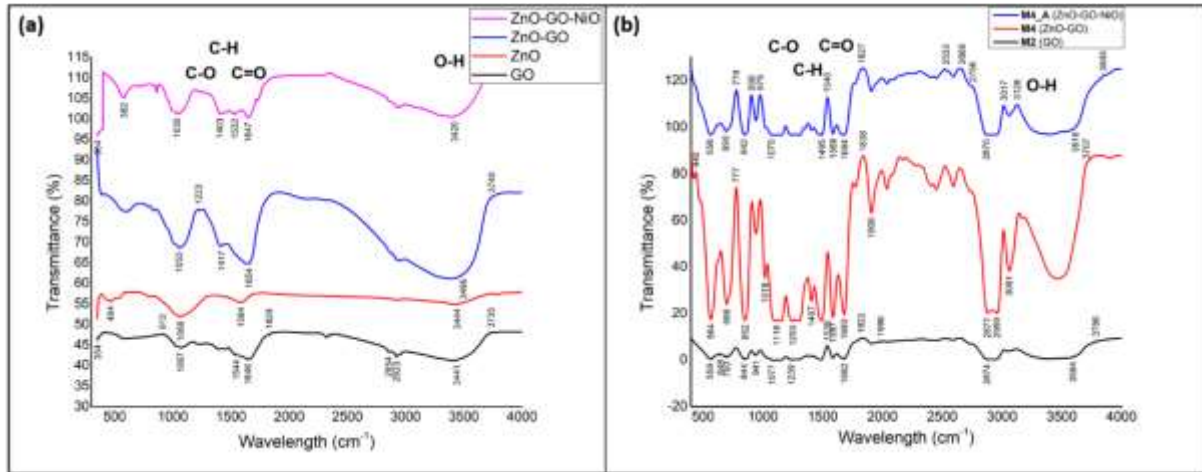


Fig 4.6 FTIR spectra of (a) nanoparticles GO, ZnO, and composites ZnO-GO (b) 0.2 wt.% GO, and 0.3 wt.% ZnO-Go, and 0.3 wt.% ZnO-GO-NiO PSF MMM.

FTIR spectra of 0.2 wt.% GO (M2), and 0.3 wt.% ZnO-Go (M4), and 0.3 wt.% ZnO-GO-NiO (M4_A) PSF MMM are demonstrated in **Fig. 4.6 (b)**. The absorption peaks at 1150 cm^{-1} , 1240 cm^{-1} and 1580 cm^{-1} represent O-S-O stretching, C-O-C stretching, and C-C Aromatic stretching vibrations in polysulfone membranes (Pramila and Gopalakrishnan, 2018b). The FTIR spectra of (GO) PSF-based membrane (M2) membrane presents absorption peaks at 3594 cm^{-1} , respectively corresponding to the stretching vibrations of the OH group in the GO layers, it signify the medium hydroxyl functional group (O-H) and primary amines (N-H) stretching (Johir *et al.*, 2016). The FTIR spectrum of (M4) mixed matrix membrane represents absorption peak at 463.19 cm^{-1} attributed to the stretching vibrations of the ZnO (Uysal, Severcan and Evis, 2013) but due to its low intensity this becomes unimportant. The absorption peak at 3474 cm^{-1} is more intense and wider in the spectrum of ZnO-GO (M4) PSF mixed matrix membrane as compared to the absorption peak at 3594 cm^{-1} in the spectrum of GO (M2) membrane (Rosnan, Teow and Mohammad, 2018). FTIR spectra of (ZnO-GO-NiO) PSF-based composite membrane (M4_A) show a transmission band at 3616 cm^{-1} , which is attributed to water molecules on the PSF

surface bending their O-H bonds. While the broad absorption band at 690 cm^{-1} corresponded to the Ni-O bond's stretching and it confirms the presence of NiO nanoparticle in membrane (M4_A) (El-kemary and Nagy, 2013). While all three membranes exhibit the same FTIR spectra in the range of 1000 cm^{-1} to 3000 cm^{-1} Functional groupings are indicated by the observed bands.

If FTIR spectra of all three membranes is discussed in general, the C-H bond's asymmetric vibrational stretching is represented by the peak at 2959 cm^{-1} (Aziz, Arifin and Lau, 2019). The appearance of (C≡C) stretching in di-substituted alkynes or (C≡N) stretching in nitro compounds was shown by the peak at 2256 cm^{-1} . Peaks at 1588 cm^{-1} and 1495 cm^{-1} illustrate the significant (N-O) stretching of the nitro compound (Yang *et al.*, 2017). 1239 cm^{-1} was used to symbolise the strong (C-O) stretching of the alkyl aryl ether or the medium (C-N) stretching of the amine. The higher (C-O) stretching of secondary alcohol and the strong stretching of sulfone (S=O) groups were both recognised by the peak at 1116 cm^{-1} . Peaks at 842 cm^{-1} and 690 cm^{-1} respectively, indicated the presence of medium and strong (C=C) of di- and tri-substituted alkenes (Ibrahim *et al.*, 2019).

4.1.7 Macroscopic analysis

TGA analysis was used to describe the thermal characteristics of neat PSF membrane and PSF-based mixed matrix membranes. According to **Fig. 4.7 (a)**, the thermal breakdown curve of every sample shows a significant weight loss at a temperature of $500\text{ }^{\circ}\text{C}$. The pristine PSF membrane appears to begin to degrade at a lower temperature, approximately $400\text{ }^{\circ}\text{C}$, compared to other composite membranes (Febriasari *et al.*, 2021). While the PSF/PEG-4000 polymers with the addition of nanocomposites GO/ZnO/NiO exhibits increased breakdown temperatures to the matrix membrane, even with modest loading, at 350 , 400 , and $450\text{ }^{\circ}\text{C}$ for 0.2 , 0.3 , and $0.5\text{ wt.}\%$ nanoparticles loading, respectively. This plainly implies that the addition of GO and metal oxides (ZnO/NiO) nanoparticles improves the thermal stability of composite membranes (Arun *et al.*, 2021).

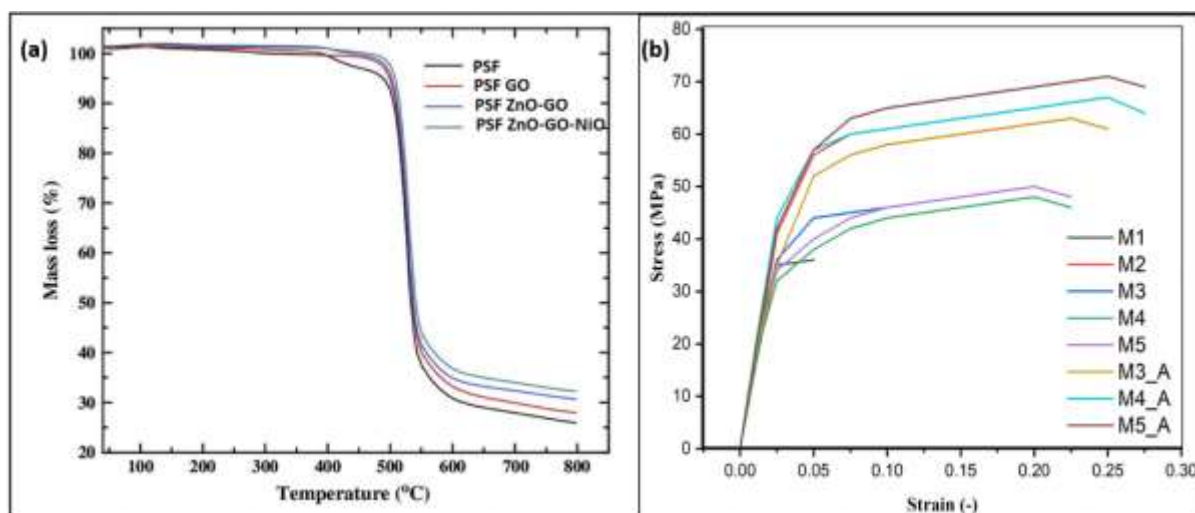


Fig. 4.7 (a) TGA curves of neat PSF, GO, ZnO-GO, and ZnO-GO-NiO PSF-based mixed matrix membranes (b) Stress with respect to the strain variations for composite membranes.

4.1.8 Mechanical Characteristics

The graphical representation between stress and strain is represented signifies the mechanical features of the prepared membranes in **Fig. 4.7 (b)**. **Table 4.1** shows the subsequent numerical values of ultimate tensile strength (MPa) and elongation or strain (%), their values at break point and young's modulus. The maximum tensile stress was utilized to estimate the ultimate tensile strength at break-even point. The young's modulus was determined by the slope of the graph in the linear elasticity regime of uniaxial deformation (Ammar *et al.*, 2015). The stress is the force applied on per unit of the cross-sectional area and the strain is change in length of the material due to application of stress (Alderliesten, 2017). Research have confirmed that the change in composition influences profoundly on tensile strength value and Young's modulus (Cuong N. Hoang, 2020). The young's modulus values show an increasing trend in the start and then a decreasing trend with respect to the density of the material (GO) in the samples (Afiqah Mohd Radzuan, Gunasegran and Naima Khalid, 2021). Firstly, the young's modulus rises with the increase of density but after the further increase in the density, young's modulus decreases as a result the material becomes stiffer by the addition of metal oxide ZnO/NiO (Tsai *et al.*, 2001).

In this research, the combination of 15 wt.% PSF with 5 wt.% PEG-4000 polymer causes a profound rise in Young's modulus values of the synthesized composite membrane (M1 = 763.91 MPa) than the described value of the neat PSF membrane (~ 246 MPa) which suggests the great interactions of the polymer and PSF substrate (Ionita, A. M. Pandele, *et al.*, 2015). With the addition of GO in the PSF substrate, the ultimate tensile strength and Young's modulus

increases (M2 = 901.30 MPa) as acquired for the membrane due to the as it leads to the formation of relatively much arranged crystalline structures (Ionita *et al.*, 2014). As the membranes get utilized for the elimination of metal ions, the membranes become incorporated with the metal oxide (ZnO) as a result the Young's modulus decrease. This decline in young's modulus values (781.52 MPa, 693.47 MPa, 735.65 MPa) creates a stiffness in the membrane which can be seen in (M3) (M4) and (M5) membrane composites respectively. The results showed (M4_A) to be the best composite membrane having the maximum ultimate tensile strength and Young's modulus (957.60 MPa) due to the addition of NiO nanoparticles in the composite membrane and its excellent mechanical properties (Tsai *et al.*, 2001). These mechanical strength attributes can support the membrane to resist high pressure during operations.

Table 4.1 Mechanical characteristics of synthesized composite membranes.

Membrane	Ultimate tensile strength (MPa)	Elongation Or Strain (%)	Tensile strength at break (MPa)	Elongation or Strain at break (%)	Young's Modulus (MPa)
M1	36.12	4.90	35.96	5.19	763.91
M2	56.83	5.92	54.43	6.16	901.30
M3	46.15	11.93	44.32	18.49	781.30
M4	48.89	19.18	45.84	20.03	693.47
M5	50.44	21.97	48.72	22.97	735.65
M3_A	63.70	22.52	61.81	25.33	753.26
M4_A	67.19	24.17	64.34	26.02	957.60
M5_A	71.47	25.88	69.25	27.66	918.91

4.2 Pure water fluxes (PWF) of membranes

Pure water flux of all synthesized membranes is represented in **Fig. 4.8 (a)**. Graph illustrates that the increment in the ratio of PEG-4000 in casting solution causes an increase in the flux which also sustains at high transmembrane pressure. Therefore, the membrane (M1) containing 15 wt.% PSF and 5 wt.% PEG when tested in dead end filtration unit for 1 hour, presents water flux of (26.16 L m⁻²h⁻¹ at 2 Kg cm⁻², while, 45.19 L m⁻²h⁻¹ and 73.90 at 2.5 Kg cm⁻² and 3 Kg cm⁻². Although according to the (Fig. 6), the membrane (M2) was hydrophobic which can reduce the efficacy of the metal ions removal. The porosity, EWC and hydrophilic nature of

the composite membranes (M3) and (M4) enhanced after the integration of ZnO nanoparticles in graphene oxide (Nisar *et al.*, 2022). In these membrane, the pure water flux increases as (54.94, 84.37, 92.69) L m⁻²h⁻¹ at (2, 2.5, 3) Kg cm⁻² in membrane (M) respectively, in increases as (75.88, 122.67, 140.92) L m⁻²h⁻¹ at (2, 2.5, 3) Kg cm⁻² in membrane (M4) respectively. While, on addition of third nanoparticle, the metal oxides (ZnO/NiO), pure water flux of membranes (M3_A) and (M4_A) increase further at 2 Kg cm⁻² as 106.76 L m⁻²h⁻¹ and 128.65 L m⁻²h⁻¹ respectively, but this increase in pure water flux is not gradual at higher transmembrane pressure (2.5-3) Kg cm⁻² that make (M4_A) membrane, the best membrane is modest values of pure water flux as compared to other composite membranes. As equilibrium water content (EWC), hydrophilic nature, porosity, and pore diameter of the membranes all contribute to the pure water flux. (Table 4.2) (Nadour *et al.*, 2017). The addition of zinc oxide nanoparticles reduced the pore size of the membranes which caused better water permeability the development of hydrophilic nature and the variation of these properties depend on the composition difference as discussed earlier (Johnson E Efome, 2019). It is observed that the pure water flux and transmembrane pressure are directly proportional (Fig. 4.8 (a)). The pore size, porosity, membrane permeability and other (quantitative) measurements were assessed through (PWF) measurement method. Table 4.2 represents the results of pure water flux measurements.

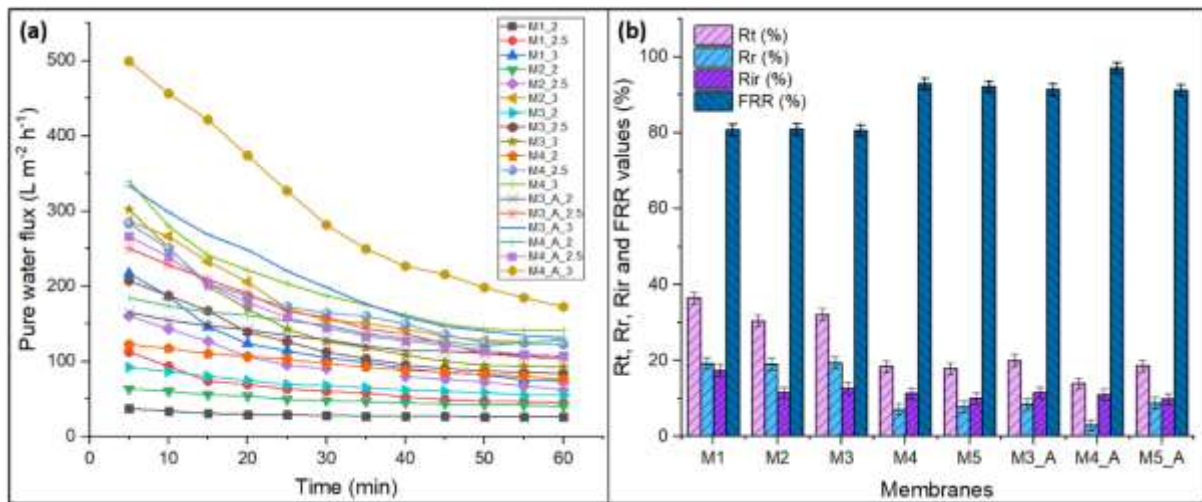


Fig. 4.8 (a) Pure water flux (PWF) of different composition membranes at three different pressures (2, 2.5, and 3 kg cm⁻²) (b) Graphical representation of R_t, R_r, R_{ir} and FRR values (%) of synthesized membranes.

Table 4.2 Pure water flux (PWF), contact angle, equilibrium water content, porosity, permeability, compaction factor at transmembrane pressure and mean pore diameter of synthesized membranes (Zhang, Xiao and Hu, 2013a).

Membrane	Dry weight of membrane (mg)	Wet weight of membrane (mg)	Pure water flux (PWF) at transmembrane pressure 2 kg cm ⁻² (J _w , L m ⁻² h ⁻¹)	Contact angle (θ)	Equilibrium water Content (EWC, %)	Porosity (ε)	Permeability (P _m , L m ⁻² h ⁻¹ kPa ⁻¹)	Compaction factor at transmembrane pressure 2 kg cm ⁻² (CF)	Mean pore diameter (nm) [Eq.(7)]
M1	126.30	350.40	26.16	101.3	63.96	0.81	0.13	1.58	27.44
M2	112.95	301.16	40.26	94.80	62.49	0.80	0.22	1.65	35.53
M3	102.92	286.77	54.94	92.70	64.11	0.81	0.25	1.70	43.32
M4	96.70	274.54	75.88	90.60	64.77	0.81	0.23	1.72	53.41
M3_A	87.66	266.84	106.76	78.40	67.14	0.83	0.27	1.78	64.17
M4_A	82.74	263.39	128.65	74.90	68.59	0.84	0.28	1.75	77.73

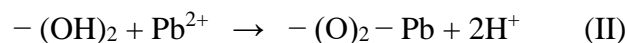
4.3 Total fouling factor (R_t) and flux recovery ratio (FRR)

Surface features of composite membranes influence the total fouling factor and its procedures. The important surface properties that effect the fouling are the surface charge, surface roughness, and hydrophilic nature of the membranes (Yin *et al.*, 2017). As the hydrophilic nature of the membrane is increased by the integration of PEG-4000 or ZnO-GO composite, the antifouling characteristics of the membranes also increases (Padaki *et al.*, 2015). But this improvement in the hydrophilic character (decline in contact angle) continues up to a specific saturation point with the addition of ZnO-GO. Beyond that limit, the accumulation of GO on the surface of membrane results in the development of hydrophobic character (Zhang, Xiao and Hu, 2013c) (Mehmet Emin Pasaoglu, 2016). This effect was observed in membrane (M5_A). By adding GO, the flux of the membrane rises due to the reduction in contact angle (Nguyen *et al.*, 2019) (Ravishankar, Christy and Jegatheesan, 2018b). The improvement in the

antifouling characteristics and the ratio of membrane flux recovery was examined by (Ebrahim Mahmoudi, 2019) by the addition of GO impregnated with 0.3 wt.% ZnO nanoparticles into the PSF/PEG-4000 membrane (Ebrahim Mahmoudi, 2019). The antifouling properties of this membrane was further enhanced by the addition of (ZnO/NiO) nanoparticles in the casting solution along with GO (Dipheko *et al.*, 2017) (Ahmad, Sugumaran and Shoparwe, 2018). The antifouling nature and the flux recovery ratios of the manufactured mixed matrix membranes are presented in **Fig. 4.8 (b)**. The total reflux values of the synthesized membranes represented a variation from 36.5% (M1) to 18.6% (M5_A), however, the FRR values showed a change from 80.8% (M1) to 91.23% (M5_A). The R_r , and R_{ir} values are quite close to each other in this filtration experiment of 50 mg L⁻¹ lead and cadmium ions solution at the transmembrane pressure of 2 kg cm⁻² (Table 4.2). These results confirm that the incorporation of the (ZnO/NiO) nanoparticles exhibited the improvement in the antifouling characteristics of the membranes (Fig. 4.7 (a)), hydrophilic properties (Fig. 4.7 (b)), permeability (Table 4.2), and the pure water flux (Fig. 4.8 (a)). The effect of the impregnation on the adsorption is discussed further in next section.

4.4 Heavy metal ions removal

Mixed matrix membranes were examined to test the removal of heavy metal ions by passing 50 mg L⁻¹ Pb²⁺ and Cd²⁺ solutions (pH = 5.5) across every membrane at 2 kg cm⁻² pressure. The membrane M4_A was found to be the most efficient membrane for metal ions removal which was followed by M3_A, possibly because of their surface charge values and contact angles (Fig. 4.4 (a) and Fig. 4.3). On the other hand, the composite membranes were very receptive to the pH of the solutions. For these membranes the adsorption may probably took place either by the oxygen or (Jamshidi Gohari, 2019) by the nitrogen-containing functional groups (Mohammad Reza Toosi, 2018) because of their capacity to make a bond by donating electrons lone pair. The equations represent the mechanism of reaction.



Cadmium metal ions shows the same adsorption mechanism for heavy metal ions removal. This mechanism, representing the involvement of functional groups was agreed by (Zhang *et*

al., 2014), and (K. C. Khulbe and Matsuura, 2018). Fig. 4.9 (a) displays graphical illustration of the adsorption mechanism. The ZnO nanoparticles further enhanced the antifouling properties of the membranes. However, the integration of ZnO nanoparticles along with GO caused an increase in the pore size which became a reason for the decline in the heavy metal ions removal (Fig. 4.9 (b) and Table 4.3) (Tariq *et al.*, 2021). These ZnO nanoparticles additionally covered a few pores and reduced the adsorption efficiency. While the addition of NiO along with ZnO-GO enhances the heavy metal ions removal also by utilizing the antifouling properties. The ZnO-GO-NiO MMM in PSF/PEG-4000 has better adsorption characteristics. Due to the presence of amine groups along the PSF chain, as well as O and N functional groups that can be replaced by pollutant ions, metal oxides have a higher affinity for metallic ions than simple ZnO-GO composite membranes. This is explained by their high surface roughness, high surface charge, and hydrophilicity, which provide a freer adsorption site from one side. Due to the membranes' lower volume when compared to Cd^{2+} , which allows for better penetration and with less resistance, they have a higher Pb^{2+} adsorption efficiency. The amine groups in equation (III) act as the Brönsted base and enables the ion exchange mechanism, while the $-\text{NH}$ groups in equation (IV) act as the Lewis base. The Pb^{+2} act as the Lewis acid assisting the electrons lone pair interactions of appear on the nitrogen, and Pb^{+2} ions. The amine groups can be protonated at low pH values which lowers the heavy metal ions removal efficiency. While at high pH values, the $-\text{NH}$ groups becomes strong as base as a result, removal efficiency of the metal ions also increases. (Mohammad Reza Toosi, 2018) describes that the solubility product value (k_{sp}) of $\text{Pb}(\text{OH})_2$ at the Pb^{+2} concentration of smaller than 75.0 mg L^{-1} is 1.42×10^{-20} due to which $\text{Pb}(\text{OH})^+$ or $\text{Pb}(\text{OH})_2$ complexes form at the pH greater than 6.0 (Zhang, Xiao and Hu, 2013c). This can also be a possible because for high removal capacity at high pH values. Fig. 4.9 (b), represents the changing behaviour of removal efficacies. M4_A membrane shows the removal efficiency for the different lead and cadmium ions concentration solutions in the ranges of $50\text{--}200 \text{ mg L}^{-1}$. Firstly, when the solutions contain more metal ions, the adsorption efficiency rises with respect to time but after that the adsorption capability reduces because of the coverage of adsorption sites (Samavati *et al.*, 2023). However, after a certain period of time, the lack of adsorption sites causes the adsorption capacity to drop and eventually reach its lowest value. (**Fig. 4.9 (a, b, c, d)**). The maximum removal percentages for Pb^{+2} and Cd^{2+} decrease with increasing initial concentration from 99.02% at 50 mg L^{-1} to 90.60% at 200 mg L^{-1} and 98.64% at 50 mg L^{-1} to 88.70% at 200 mg L^{-1} , respectively, with the

minimum concentration (50 mg L⁻¹) exhibiting the highest overall percentages removal (67.90% for Pb(II) and 62.31 for Cd(II)). This is shown in the **Fig. 4.9 (a, b)**.

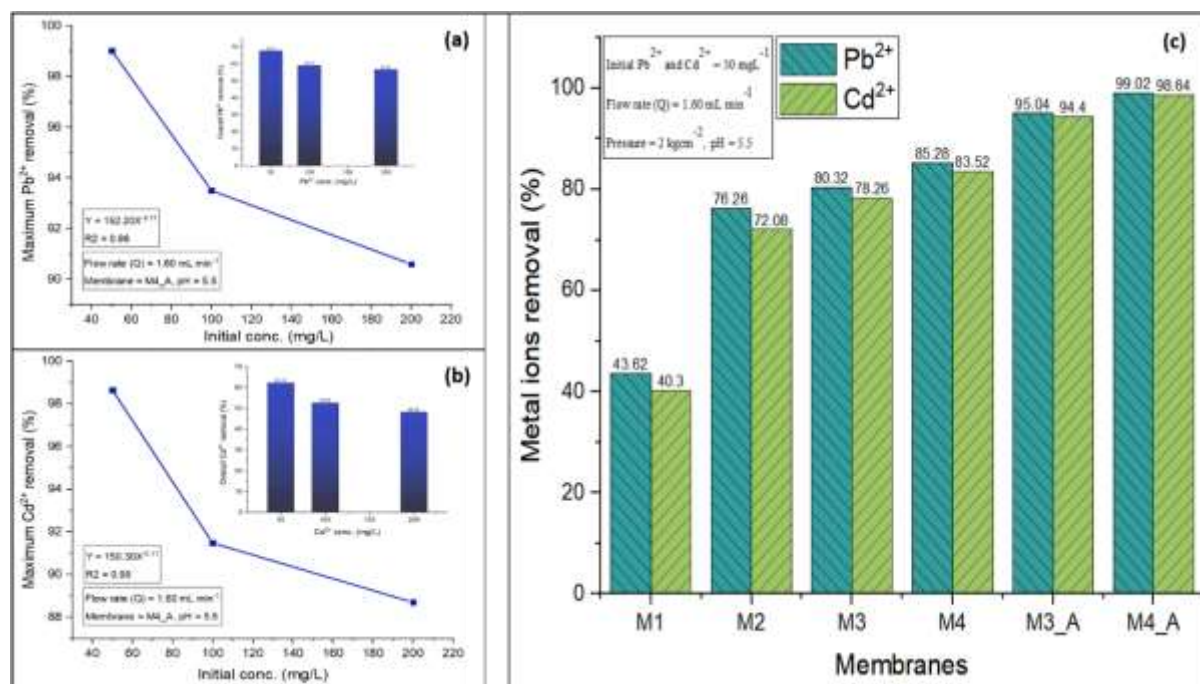


Fig. 4.9 (a) (b) represents percentage removal with different concentrations of Pb²⁺ and Cd²⁺ ions for membrane (M4_A) (c) Removal percentages of Pb(II) and Cd(II) by all the synthesized membranes.

Table 4.3 Pb(II) and Cd(II) adsorption at various feed concentrations: Approximated values from the breakthrough curves and the Thomas model (Membrane = M4_A, flow rate = 1.60 mL min⁻¹, fixed pH = 5.5)

Q (mL min ⁻¹)	Conc. (mgL ⁻¹)	Time at the Breakthrough point (t _b , min)	The total vol. of Soln. passed (V _{br} , mL)	Time at the exhaustion point (t, min)	Contaminant fed (m ₀ , mg)	Contaminant adsorbed (q _v , mg)	Overall removal percentage (R _o %)	K _T (Lmg ⁻¹ min ⁻¹)	q ₀ (mg g ⁻¹) experimental	q ₀ (mg g ⁻¹) calculated	R ²	%E
For lead Pb (II)												
1.60	50	96.13	300	245.76	19.66	13.35	67.90	7.05 x 10 ⁻⁴	148.14	149.60	0.99	0.98
1.60	100	53.09	250	215.34	34.45	20.41	59.25	3.38 x 10 ⁻⁴	233.75	240.14	0.99	2.73
1.60	200	26.17	200	138.29	44.25	25.16	56.85	2.40 x 10 ⁻⁴	362.40	379.38	0.99	4.69

For Cadmium Cd (II)

1.60	50	98.21	300	249.34	19.95	12.43	62.31	7.02×10^{-4}	141.60	142.98	0.99	0.97
1.60	100	62.43	250	219.69	35.15	18.51	52.66	3.32×10^{-4}	228.70	234.17	0.99	2.39
1.60	200	29.51	200	143.54	45.93	22.16	48.24	2.33×10^{-4}	354.80	371.54	0.99	4.72

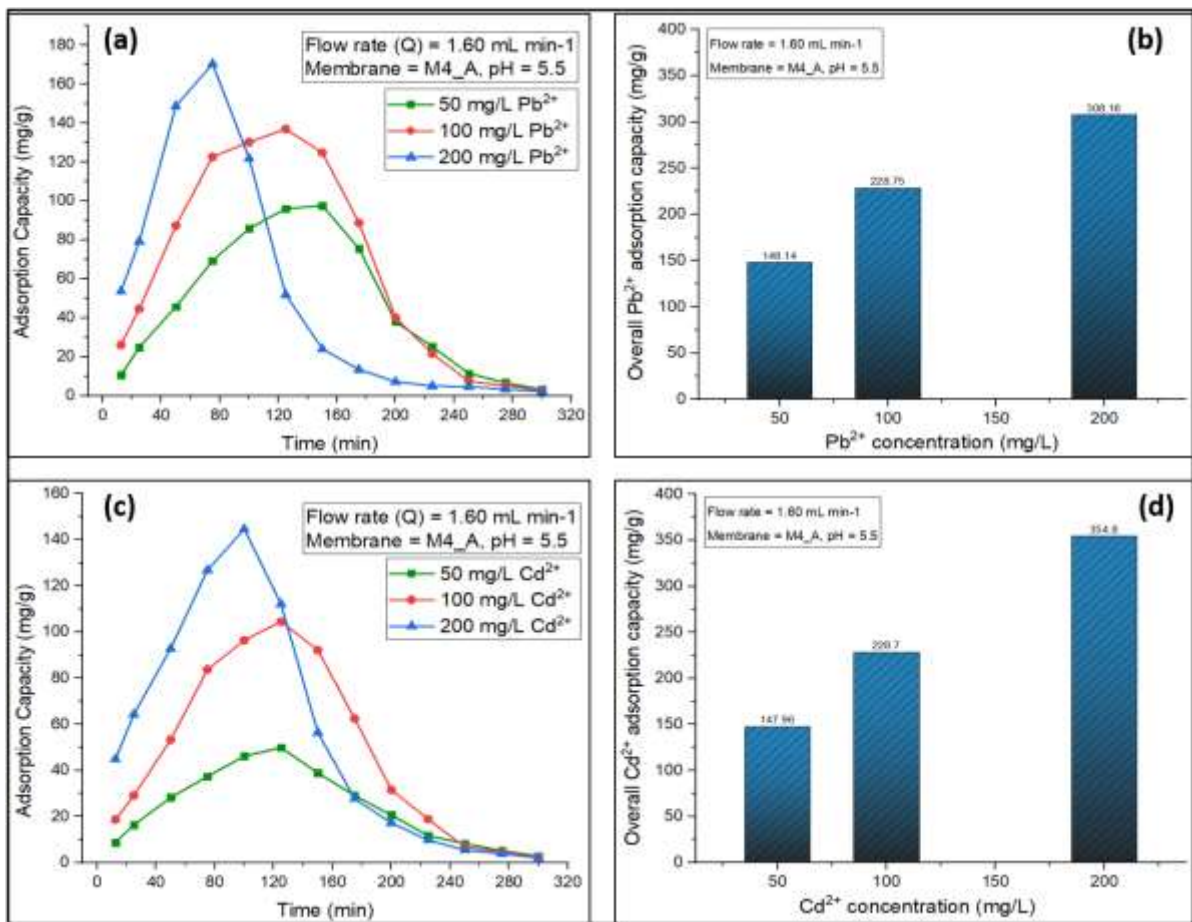


Fig. 4.10 (a) Change in adsorption capacity values (mg g⁻¹) of membrane (M4_A) for Pb (II) and Cd (II) ions.

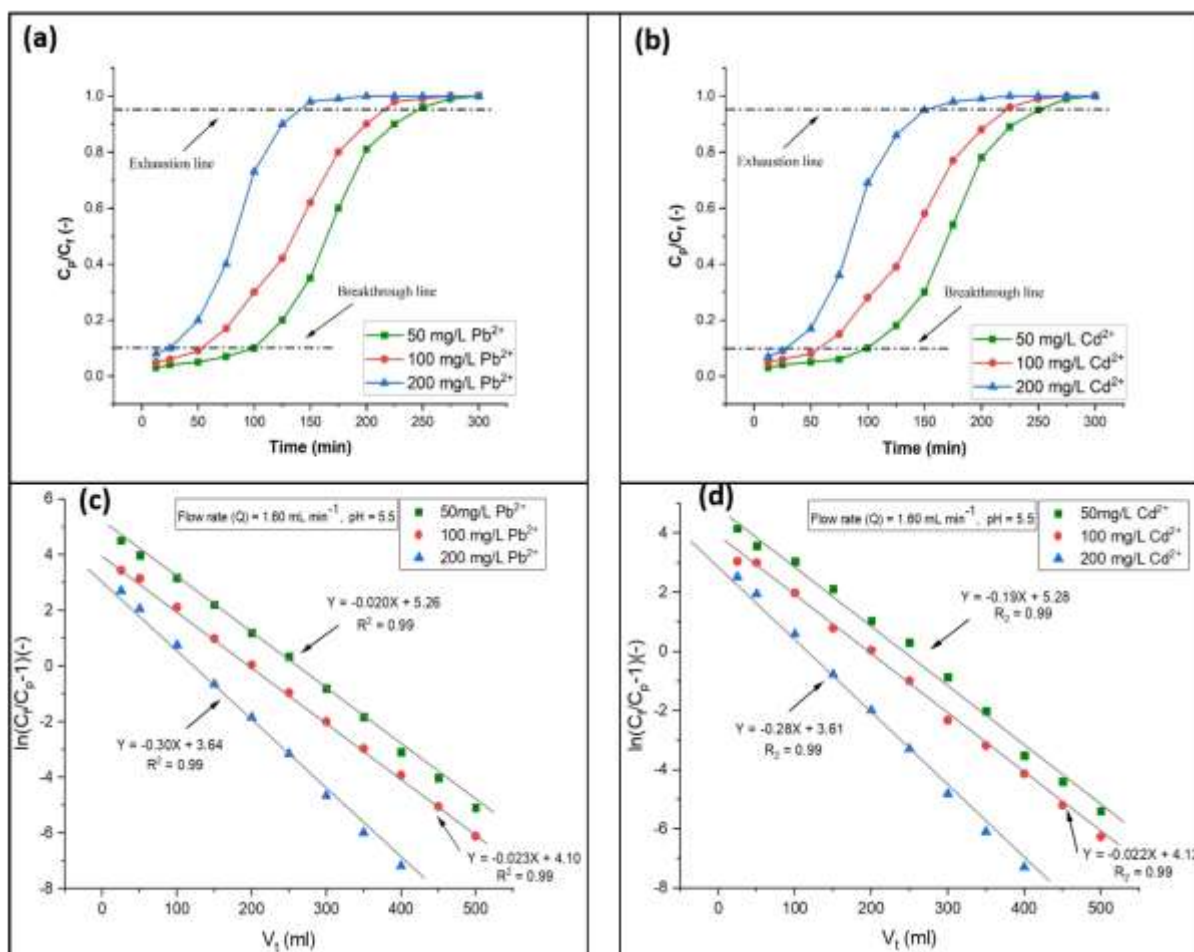


Fig. 4.11 (a) (b) represents Pb(II) and Cd(II) breakthrough curves at various feed concentrations (c) (d) shows Thomas model plots at different concentration of Pb (II) and Cd (II) respectively. (Membrane = M4_A).

Breakthrough curves shows (**Fig. 4.10 (a, b)**), that the breakthrough point and the exhaustion point (C_p/C_f) is (0.1) and (0.95) respectively, achieves in small time period when the concentration is high (Johnson E Efome, 2019). Hence, to operates the process for long time, the concentration of the metal ions should be less initially. In this way, the process will be continued without regeneration for more time. The adsorption data satisfies Thomas model (Table 8) within $\pm 4.7\%$ error and 0.99 correlation coefficient (R^2). **Fig. 4.10 (c, d)** shows Thomas model graph. According to the assumptions (Thomas model), the experimental process of adsorption fits to the second-order kinetic model and the Langmuir isotherm (Maleki *et al.*, 2021).

EDX analysis was again performed for the elemental characterization of the heavy metal ions removal (**Fig. 4.11**), which verifies that the metal ions were adsorbed by the membrane before and after the completion of the process. Fig. 4.11 explained that the uptake of the metal ions

reduces with respect to the time. Though, lead ions achieved the maximum adsorption capacity (99.02 % removal) and the least hydrated ionic radii and greater surface charge density, followed by cadmium ions which is (98.64 % removal). Due to which it contented with the proton with maximum removal capacity by membrane (M4_A) (Fig. 4.9 (b)) (Lau *et al.*, 2015)

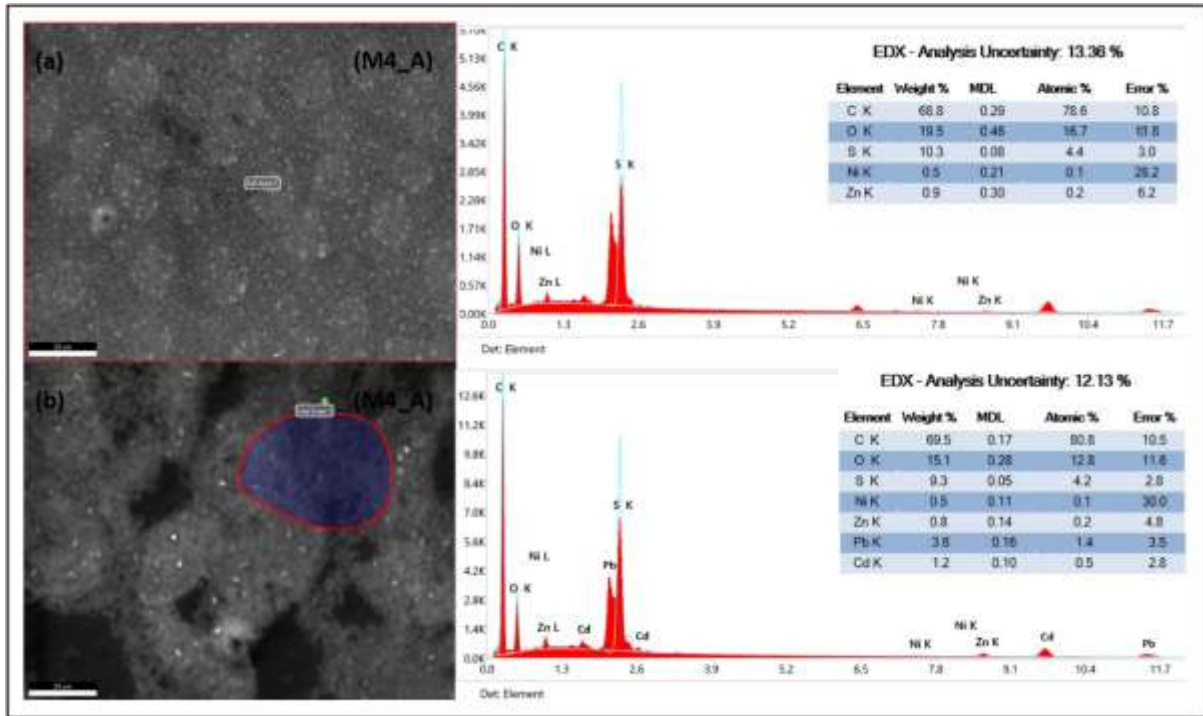


Fig. 4.12 EDX analysis of membranes (a) before the adsorption (b) after the adsorption, and (c) compositional analysis of membrane (M4_A)

Conclusion

5. Conclusion

In this research, polysulfone membranes with the combination of different nanoparticles are synthesized, characterized and their application for the removal of heavy metal ions from wastewater is discussed. The integration of PEG-4000 with the PSF membranes improves the solvent and non-solvent de-mixing that results in the development of more porous membrane structure and high permeate flux of membranes. The surface characteristics of membranes and metal ions removal efficiency were further increased by impregnating graphene oxide (GO) on to the membranes and it also increase the membrane strength. Although a declining trend in pore size and permeate flux was observed but this improved the mechanical characteristics of the membranes. The integration of metal oxide zinc oxide and nickel oxide (ZnO/NiO) nanoparticles prepended various properties in the membranes such as enhancement in antifouling characteristics, improvement in hydrophilic nature, permeate flux, pore size, and the flux recovery ratio. The negative surface charge also raised from -24.8 mV (M1) to -54.9 mV (M4_A), which improved the adsorption efficiency of the membrane. It increases from (GO) to (ZnO-GO) composite membranes as -33.40 mV (M2) to -44.30 mV (M4) and further increases from (ZnO-GO) to (ZnO-GO-NiO) MMMs as -33.40 mV (M4) to -54.90 mV (M4_A) respectively. With a flow rate of 1.60 mL min^{-1} and a pH value of 5.5, the membrane (M4_A) adsorption capacities enhances from 148.14 mg g^{-1} to 308.16 mg g^{-1} for Pb^{2+} and 147.96 mg g^{-1} to 354.80 mg g^{-1} for Cd^{2+} , when their concentration increase from 50 mg L^{-1} to 200 mg L^{-1} . However, because the exhaustion point is reached sooner for higher concentrations (245.76 min for 50 mg L^{-1} and 138.29 min for 200 mg L^{-1}) for Pb^{2+} , and (249.34 min for 50 mg L^{-1} and 143.54 min for 200 mg L^{-1}), the overall recovery percentages for the higher concentration fall from 67.90% to 56.85% for lead and 62.31% to 48.24% for cadmium. With a maximum error of $\pm 4.7\%$, the experimental adsorption results suited the Thomas model, proving that the Langmuir isotherms model and second-order kinetics were used in the adsorption process. Based on the results of the current study, it can be concluded that the final composite (ZnO-GO-NiO) membranes (M3_A, M4_A) are preferable to the (ZnO-GO) membranes (M3, M4) as they are having a higher adsorption capacity of (Pb^{2+} , Cd^{2+}) ions and higher flux and antifouling properties. (M4_A) membrane had a higher flux recovery percentage of (97.10%) as compared to other membranes. Because the (M4_A) membrane operates for a longer period

of time while having a greater removal efficiency, it is preferred to operate it at lower metal ion concentrations.

References:

- [1] Hanson, R.T., et al., *Rio Grande transboundary integrated hydrologic model and water-availability analysis, New Mexico and Texas, United States, and northern Chihuahua, Mexico*. 2020, US Geological Survey.
- [2] Haase, F.T., et al., *Role of Nanoscale inhomogeneities in Co₂FeO₄ catalysts during the oxygen evolution reaction*. *Journal of the American Chemical Society*, 2022. 144(27): p. 12007-12019.
- [3] Briffa, J., E. Sinagra, and R. Blundell, *Heavy metal pollution in the environment and their toxicological effects on humans*. *Heliyon*, 2020. 6(9): p. e04691.
- [4] Zacchaeus, O.O., et al., *Effects of industrialization on groundwater quality in Shagamu and Ota industrial areas of Ogun state, Nigeria*. *Heliyon*, 2020. 6(7): p. e04353.
- [5] Van Dyck, C.H., et al., *Lecanemab in early Alzheimer's disease*. *New England Journal of Medicine*, 2023. 388(1): p. 9-21.
- [6] Khan, H.A.A., S.A. Shad, and W. Akram, *Resistance to new chemical insecticides in the house fly, Musca domestica L., from dairies in Punjab, Pakistan*. *Parasitology research*, 2013. 112: p. 2049-2054.
- [7] Ortony, A., G.L. Clore, and A. Collins, *The cognitive structure of emotions*. 2022: Cambridge university press.
- [8] Song, J., et al., *Preparation of montmorillonite modified biochar with various temperatures and their mechanism for Zn ion removal*. *Journal of hazardous materials*, 2020. 391: p. 121692.
- [9] Roy, S. and S. Ragonath, *Emerging membrane technologies for water and energy sustainability: Future prospects, constraints and challenges*. *Energies*, 2018. 11(11): p. 2997.
- [10] Kathrin, H., et al., *Eco-innovations in the German fertilizer supply chain: Impact on the carbon footprint of fertilizers*. *Plant, Soil and Environment*, 2017. 63(12): p. 531-544.
- [11] Salehi, M., et al., *Electrospun nanofibers for efficient adsorption of heavy metals from water and wastewater*. 2021.
- [12] Rout, D.R., et al., *Graphene-based materials for effective adsorption of organic and inorganic pollutants: A critical and comprehensive review*. *Science of The Total Environment*, 2023. 863: p. 160871.

- [13] Velusamy, S., et al., *A review on heavy metal ions and containing dyes removal through graphene oxide-based adsorption strategies for textile wastewater treatment*. The Chemical Record, 2021. 21(7): p. 1570-1610.
- [14] Ali, H., E. Khan, and I. Ilahi, *Environmental chemistry and ecotoxicology of hazardous heavy metals: environmental persistence, toxicity, and bioaccumulation*. Journal of chemistry, 2019. 2019.
- [15] Dasari Shareena, T.P., et al., *A review on graphene-based nanomaterials in biomedical applications and risks in environment and health*. Nano-micro letters, 2018. 10: p. 1-34.
- [16] Sheoran, K., et al., *Recent advances of carbon-based nanomaterials (CBNMs) for wastewater treatment: Synthesis and application*. Chemosphere, 2022: p. 134364.
- [17] Motitswe, M.G., K.O. Badmus, and L. Khotseng, *Development of Adsorptive Materials for Selective Removal of Toxic Metals in Wastewater: A Review*. Catalysts, 2022. 12(9): p. 1057.
- [18] Liu, X., et al., *Metal (Ni, Co)-metal oxides/graphene nanocomposites as multifunctional electrocatalysts*. Advanced Functional Materials, 2015. 25(36): p. 5799-5808.
- [19] Buledi, J.A., et al., *A Reusable Nickel Oxide Reduced Graphene Oxide Modified Platinum Electrode for the Detection of Linezolid Drug*. Industrial & Engineering Chemistry Research, 2023.
- [20] Dhiman, V. and N. Kondal, *ZnO Nanoadsorbents: A potent material for removal of heavy metal ions from wastewater*. Colloid and Interface Science Communications, 2021. 41: p. 100380.
- [21] Haq, I.U., et al., *A Comparison of Two-Way (Chemical and Thermal) Synthesis and Characterization of the Graphene Oxide (Go) and the Reduced Graphene Oxide (Rgo)*. Available at SSRN 4415876.
- [22] Guerrero-Contreras, J. and F. Caballero-Briones, *Graphene oxide powders with different oxidation degree, prepared by synthesis variations of the Hummers method*. Materials Chemistry and Physics, 2015. 153: p. 209-220.
- [23] Gusatti, M., et al., *Effect of different precursors in the chemical synthesis of ZnO nanocrystals*. Materials Research, 2011. 14: p. 264-267.
- [24] Obodo, R.M., et al., *Conjugated NiO-ZnO/GO nanocomposite powder for applications in supercapacitor electrodes material*. International Journal of Energy Research, 2020. 44(4): p. 3192-3202.

- [25] Obodo, R.M., et al., *Recent advances in metal oxide/hydroxide on three-dimensional nickel foam substrate for high performance pseudocapacitive electrodes*. Current Opinion in Electrochemistry, 2020. 21: p. 242-249.
- [26] Nasirian, D., et al., *Investigation of the gas permeability properties from polysulfone/polyethylene glycol composite membrane*. Polymer Bulletin, 2020. 77: p. 5529-5552.
- [27] Bărdacă Urducea, C., et al., *Control of nanostructured polysulfone membrane preparation by phase inversion method*. Nanomaterials, 2020. 10(12): p. 2349.
- [28] Basri, H., A.F. Ismail, and M. Aziz, *Polyethersulfone (PES)–silver composite UF membrane: Effect of silver loading and PVP molecular weight on membrane morphology and antibacterial activity*. Desalination, 2011. 273(1): p. 72-80.
- [29] Thomas, L.E. and S.M. Bruemmer, *High-resolution characterization of intergranular attack and stress corrosion cracking of Alloy 600 in high-temperature primary water*. Corrosion, 2000. 56(06).
- [30] Khayet, M. and M.d.C. García-Payo, *X-Ray diffraction study of polyethersulfone polymer, flat-sheet and hollow fibers prepared from the same under different gas-gaps*. Desalination, 2009. 245(1-3): p. 494-500.
- [31] Muniz, F.T.L., et al., *The Scherrer equation and the dynamical theory of X-ray diffraction*. Acta Crystallographica Section A: Foundations and Advances, 2016. 72(3): p. 385-390.
- [32] Rust, C., et al., *Global Alignment of Carbon Nanotubes via High Precision Microfluidic Dead-End Filtration*. Advanced Functional Materials, 2022. 32(10): p. 2107411.
- [33] Rezaee, R., et al., *Fabrication and characterization of a polysulfone-graphene oxide nanocomposite membrane for arsenate rejection from water*. Journal of Environmental Health Science and Engineering, 2015. 13: p. 1-11.
- [34] Sinha, M. and M. Purkait, *Increase in hydrophilicity of polysulfone membrane using polyethylene glycol methyl ether*. Journal of Membrane Science, 2013. 437: p. 7-16.
- [35] Chakrabarty, B., A. Ghoshal, and M. Purkait, *Effect of molecular weight of PEG on membrane morphology and transport properties*. Journal of membrane science, 2008. 309(1-2): p. 209-221.
- [36] Lorente-Ayza, M.-M., et al., *Comparison of porosity assessment techniques for low-cost ceramic membranes*. boletín de la sociedad española de cerámica y vidrio, 2017. 56(1): p. 29-38.

- [37] Ghaemi, N., S. Zereshti, and S. Heidari, *Removal of lead ions from water using PES-based nanocomposite membrane incorporated with polyaniline modified GO nanoparticles: Performance optimization by central composite design*. Process Safety and Environmental Protection, 2017. 111: p. 475-490.
- [38] Son, M., et al., *Influence of extreme concentrations of hydrophilic pore-former on reinforced polyethersulfone ultrafiltration membranes for reduction of humic acid fouling*. Chemosphere, 2017. 179: p. 194-201.
- [39] Mohammad, N. and Y. Atassi, *Enhancement of removal efficiency of heavy metal ions by polyaniline deposition on electrospun polyacrylonitrile membranes*. Water Science and Engineering, 2021. 14(2): p. 129-138.
- [40] Khulbe, K. and T. Matsuura, *Removal of heavy metals and pollutants by membrane adsorption techniques*. Applied water science, 2018. 8: p. 1-30.
- [41] Hutera, B., et al., *Synthesis of ZnO nanoparticles by thermal decomposition of basic zinc carbonate*. Archives of Metallurgy and Materials, 2013. 58.
- [42] Huang, Y., et al., *Poly (lactic acid)/graphene oxide-ZnO nanocomposite films with good mechanical, dynamic mechanical, anti-UV and antibacterial properties*. Journal of Chemical Technology & Biotechnology, 2015. 90(9): p. 1677-1684.
- [43] Zhou, Q., et al., *Fabrication and characterization of highly sensitive and selective sensors based on porous NiO nanodisks*. Sensors and Actuators B: Chemical, 2018. 259: p. 604-615.
- [44] Lee, P.-H., et al., *Highly crystalline colloidal nickel oxide hole transport layer for low-temperature processable perovskite solar cell*. Chemical Engineering Journal, 2021. 412: p. 128746.
- [45] Bekele, B., et al., *Green versus chemical precipitation methods of preparing zinc oxide nanoparticles and investigation of antimicrobial properties*. Journal of Nanomaterials, 2021. 2021: p. 1-10.
- [46] Alamdari, S., et al., *Preparation and characterization of GO-ZnO nanocomposite for UV detection application*. Optical Materials, 2019. 92: p. 243-250.
- [47] Mardiroosi, A., A.R. Mahjoub, and H. Fakhri, *Efficient visible light photocatalytic activity based on magnetic graphene oxide decorated ZnO/NiO*. Journal of Materials Science: Materials in Electronics, 2017. 28: p. 11722-11732.
- [48] Liang, H.-q., et al., *Polysulfone membranes via thermally induced phase separation*. Chinese Journal of Polymer Science, 2017. 35(7): p. 846-856.

- [49] Nasser, S., et al., *Synthesis and characterization of polysulfone/graphene oxide nano-composite membranes for removal of bisphenol A from water*. Journal of environmental management, 2018. 205: p. 174-182.
- [50] Chong, W.C., et al., *Improving performance in algal organic matter filtration using polyvinylidene fluoride–graphene oxide nanohybrid membranes*. Algal research, 2017. 27: p. 32-42.
- [51] Angesti, W. and M. Munasir. *Fabrication and Characterization of Polysulfone Membrane Based On GO-SiO₂ Composite using Phase Inversion Method*. in *E3S Web of Conferences*. 2021. EDP Sciences.
- [52] Ayyaru, S., T.T.L. Dinh, and Y.-H. Ahn, *Enhanced antifouling performance of PVDF ultrafiltration membrane by blending zinc oxide with support of graphene oxide nanoparticle*. Chemosphere, 2020. 241: p. 125068.
- [53] Pasaoglu, M.E., S. Guclu, and I. Koyuncu, *Polyethersulfone/polyacrylonitrile blended ultrafiltration membranes: preparation, morphology and filtration properties*. Water Science and Technology, 2016. 74(3): p. 738-748.
- [54] Daraei, P., et al., *Fouling resistant mixed matrix polyethersulfone membranes blended with magnetic nanoparticles: Study of magnetic field induced casting*. Separation and Purification Technology, 2013. 109: p. 111-121.
- [55] Ahmad, A., et al., *Recent development in additives modifications of polyethersulfone membrane for flux enhancement*. Chemical engineering journal, 2013. 223: p. 246-267.
- [56] Hosny, N.M., et al., *Synthesis, magnetic and adsorption of dye onto the surface of NiO nanoparticles*. Journal of Materials Science: Materials in Electronics, 2020. 31: p. 8413-8422.
- [57] Gu, Y., et al., *Facile fabrication of composition-tunable Fe/Mg bimetal-organic frameworks for exceptional arsenate removal*. Chemical Engineering Journal, 2019. 357: p. 579-588.
- [58] Plisko, T.V., et al., *Modification of polysulfone ultrafiltration membranes via addition of anionic polyelectrolyte based on acrylamide and sodium acrylate to the coagulation bath to improve antifouling performance in water treatment*. Membranes, 2020. 10(10): p. 264.
- [59] Ahmad, D., et al., *Hydrophilic and hydrophobic materials and their applications*. Energy Sources, Part A: Recovery, Utilization, and Environmental Effects, 2018. 40(22): p. 2686-2725.

- [60] Elsie, S., et al., *Tris-(2-aminoethyl) amine-intercalated graphene oxide as an efficient 2D material for cerium-ion fluorescent sensor applications*. ACS omega, 2019. 4(27): p. 22431-22437.
- [61] Gupta, S., C. Ravikant, and A. Kaur, *One-pot wet chemical synthesis of reduced graphene oxide-zinc oxide nanocomposites for fast and selective ammonia sensing at room temperature*. Sensors and Actuators A: Physical, 2021. 331: p. 112965.
- [62] Pricilla, R.B., et al., *GO/NiO nanocomposite: Chemosensor for L-Leucine and a potential antibacterial agent*. Materials Today: Proceedings, 2021. 47: p. 814-818.
- [63] Ibrahim, M.I., et al., *Extraction, chemical composition, and characterization of potential lignocellulosic biomasses and polymers from corn plant parts*. BioResources, 2019. 14(3): p. 6485-6500.
- [64] Ionita, M., et al., *Synthesis, characterization and in vitro studies of polysulfone/graphene oxide composite membranes*. Composites Part B: Engineering, 2015. 72: p. 108-115.
- [65] Nadour, M., et al., *Effects of methylcellulose on the properties and morphology of polysulfone membranes prepared by phase inversion*. Materials Research, 2017. 20: p. 339-348.
- [66] Padaki, M., et al., *Antifouling properties of novel PSf and TNT composite membrane and study of effect of the flow direction on membrane washing*. Desalination, 2015. 362: p. 141-150.
- [67] Toosi, M.R., M.R.S. Emami, and S. Hajian, *Dynamic filtration and static adsorption of lead ions in aqueous solution by use of blended polysulfone membranes with nano size MCM-41 particles coated by polyaniline*. Environmental Science and Pollution Research, 2018. 25: p. 20217-20230.
- [68] Shahrin, S., et al., *Development of adsorptive ultrafiltration membranes for heavy metal removal*, in *Advanced Nanomaterials for Membrane Synthesis and its Applications*. 2019, Elsevier. p. 1-22.
- [69] Samavati, Z., et al., *A comprehensive review of recent advances in nanofiltration membranes for heavy metal removal from wastewater*. Chemical Engineering Research and Design, 2022.

APPENDICES

APPENDIX A: Cd²⁺ Stock Solution Preparation Calculation

Stock solution preparation ample calculation

mass of Cd(NO₃)₂·4H₂O = V x MW of Cd(NO₃)₂·4H₂O x ppm of Cd²⁺ /MW of Cd²⁺x stoichiometry

As,

$$V = 1 \text{ L}$$

$$\text{MW of Cd(NO}_3)_2 \cdot 4\text{H}_2\text{O} = 308.49 \text{ g/mol}$$

$$\text{MW of Cd}^{2+} = 112.41 \text{ g/mol}$$

$$\text{ppm of Cd}^{2+} = 100 \text{ mg/L}$$

$$\text{mass of Cd(NO}_3)_2 \cdot 4\text{H}_2\text{O} = 1 \times 308.49 \times 100 / 112.41 \times 1 \text{ mol Cd}^{2+} / 1 \text{ mol NO}_3 = 274.43 \text{ mg/L}$$

So, 274.43 mg of Cd(NO₃)₂·4H₂O should be added in 1 Liter deionised water to prepare 100 mg/L of Cd²⁺ stock solution.

APPENDIX B: 40 ppm of Cd²⁺ Solution preparation Calculation

$$C_1V_1=C_2V_2$$

As,

$$C_1 = 100 \text{ ppm}$$

$$C_2 = 40 \text{ ppm}$$

$$V_1 = \text{required volume of Cd}^{2+} \text{ stock solution, mL}$$

$$V_2 = 60 \text{ mL}$$

$$V_1 = C_2V_2/C_1$$

$$= 40 \text{ ppm} \times 60 \text{ mL} / 100 \text{ ppm}$$

$$= 24 \text{ mL}$$

Therefore, 24 mL of 100 ppm Cd²⁺ stock solution will be added in 48 mL of deionized water to prepare 60 mL of 40 ppm Cd²⁺ solution.

APPENDIX C: Pb²⁺ Stock Solution Preparation Calculation

mass of Pb(NO₃)₂ = V x MW of Pb(NO₃)₂ x ppm of Pb²⁺ /MW of Pb²⁺x stoichiometry

As,

$$V = 1 \text{ L}$$

Molar mass of $\text{Pb}(\text{NO}_3)_2 = 331.2 \text{ g/mol}$

Molar mass of $\text{Pb}^{2+} = 207 \text{ g/mol}$

ppm of $\text{Pb}^{2+} = 100 \text{ mg/L}$

$$\text{mass of } \text{Pb}(\text{NO}_3)_2 = 1 \times 331.2 \times 100 / 207 \times 1 \text{ mol } \text{Pb}^{2+} / 1 \text{ mol } \text{NO}_3 = 160 \text{ mg/L}$$

So, 160 mg of $\text{Pb}(\text{NO}_3)_2$ should be added in 1 Liter deionised water to prepare 100 mg/L of Pb^{2+} stock solution.

APPENDIX D: 0.2 M HCl Solution Preparation Calculation

MW of HCl = 36.5 g/mol

Specific gravity of HCl (37 wt%) = 1190 g/L

Molarity of HCl (37 wt%)

$$37 \text{ ml} / 100 \text{ ml} \times 1190 \text{ g/L} \times 136.5 \text{ g/mol} = 12.06 \text{ M}$$

Using dilution factor equation:

$$C_1 V_1 = C_2 V_2$$

As,

$$C_1 = 12.06 \text{ M}$$

$$C_2 = 0.2 \text{ M}$$

$V_1 =$ Required volume of HCl (37 wt%), mL

$$V_2 = 500 \text{ mL}$$

$$V_1 = C_2 V_2 / C_1$$

$$= 0.2 \times 500 / 12.06$$

$$= 8.29 \text{ mL}$$

So, 8.29 mL of HCl (37 wt.%) should be added to 495.854 mL distilled water to prepare 0.2 M of HCl.

APPENDIX E: 0.2 M NaOH solution Preparation Calculation

MW of NaOH = 40 g/mol

Volume of 0.2 M of NaOH = 0.5 L

$$0.5 \times 0.2 \times 40 = 4 \text{ g}$$

So, 4 g of NaOH should be added to 500 mL distilled water to prepare 0.2 molar NaOH soln.